

Supplementary Information for:

The critical role played by water in controlling Pd catalyst speciation in arylcyanation reactions

Joshua T. W. Bray,^a Mark J. Ford,^b Peter B. Karadakov,^a Adrian C. Whitwood^a and Ian J. S. Fairlamb^{a*}

^aDepartment of Chemistry, University of York, Heslington, York, YO10 5DD, United Kingdom.

^bBayer Aktiengesellschaft, Crop Science Division, Industriepark Höchst G836, 65926 Frankfurt am Main, Germany.

Contents

1. General information.....	2
1.1. Preparative and laboratory analysis.....	2
1.2. Instrument details for compound characterisation purposes.....	3
2. Mechanistic and kinetic studies.....	4
2.1. General procedure: React-IR kinetic studies of Pd-catalysed arylcyanations.....	4
2.2. Catalyst loading and temperature effects of catalyst efficiency under anhydrous conditions.....	6
2.3. Determination of order w.r.t. 1-pip.....	7
2.4. Determination of order w.r.t. 2.....	8
2.5. Catalyst loading investigations with 1-pip, using K ₄ [Fe(CN) ₆]·3H ₂ O.....	8
2.6. Finke-Watzky curvefits for sigmoidal kinetic plots.....	9
2.7. Hg drop test of reaction with K ₄ [Fe(CN) ₆]·3H ₂ O.....	17
2.8. Catalyst loading k _{obs} relationship with K ₄ [Fe(CN) ₆]·3H ₂ O.....	18
2.9. On the Role of Na ₂ CO ₃ in aryl cyanations.....	18
2.10. On the behavior of alternative hexacyanoferrate salts.....	23
2.11. Characterisation of “solubilised [Fe(CN) ₆] ⁴⁻ ”.....	23
2.12. Varying K ₄ [Fe(CN) ₆]·3H ₂ O equivalences.....	28
2.13. Relative aromaticities of N-methyl-4-bromo-6-methyl-2-pyridone, bromobenzene, pyridine and benzene.....	30
2.14. Substrate scope.....	36
3. Experimental.....	37
4. NMR spectra of organic compounds.....	41
4.1. N-Benzyl-4-bromo-6-methylpyridin-2-one (2).....	41
1.1. N-Benzyl-4-cyano-6-methylpyridin-2-one (3).....	43
4.2. 1,4-Dicyanobenzene (4).....	44

4.3.	4-Fluorobenzonitrile (5)	45
4.4.	2-Methylbenzonitrile (6)	47
4.5.	4-Phenylbenzonitrile (7).....	48
4.6.	4-(Methylthio)benzonitrile (8)	49
4.7.	9-Cyanoanthracene (9)	50
4.8.	4-Formylbenzonitrile (10).....	51
4.9.	2-Thiophenecarbonitrile (11)	52
4.10.	2-Phenylbenzonitrile (12)	53
4.11.	4-Methoxybenzonitrile (13).....	54
4.12.	Benzonitrile (14).....	55
5.	NMR spectra of Pd amine complexes	56
5.1.	1-Pyr.....	56
5.2.	1-Pip	57
5.3.	1-Aze	58
5.4.	1-DMP.....	59
6.	X-Ray crystallography.....	60
6.1.	General details	60
6.2.	X-ray data for 3 and complexes 1-Pyr, 1-Aze and 1-DMP	61
7.	References.....	67

1. General information

1.1. Preparative and laboratory analysis

Reagents were purchased from Sigma-Aldrich, Alfa Aesar, Acros Organics or Fluorochem and used as received unless otherwise stated. Isotopically labelled chemicals were purchased from Icon Isotopes Ltd. and used as received. Pd(OAc)₂ was obtained from Precious Metals Online. Dry THF, CH₂Cl₂ and acetonitrile were obtained from a Pure Solv MD-7 solvent system and stored under nitrogen. THF was also degassed by bubbling nitrogen through the solvent with sonication. Dry methanol was obtained by drying over 3 Å molecular sieves. Petroleum ether (petrol) refers to the fraction of petroleum that is collected at 40-60 °C. Piperidine was distilled from KOH under a nitrogen atmosphere and stored in an ampoule wrapped in aluminium foil under nitrogen. Pyrrolidine, azepane, 2,6-*cis* dimethylpiperidine and 2,2,6,6-tetramethylpiperidine were all freshly purified prior to use *via* short path distillation. Extra dry DMAc was obtained from Acros with a maximum water content of 0.005%, degassed by bubbling with nitrogen gas through the solvent with sonication and stored in ampoules under nitrogen while over activated 4Å molecular sieves. Reactions requiring anhydrous conditions were carried out using Schlenk techniques (high vacuum, liquid nitrogen trap on a standard in-house built dual line). Room temperature upper and lower limits are stated as 13-25 °C, but typically 21 °C was recorded. Brine refers to a saturated aqueous solution of NaCl.

Thin layer chromatography (TLC) was carried out using Merck 5554 aluminium backed silica plates (silica gel 60 F254) and spots were visualized using UV light (at 254 nm). Where necessary, plates were stained and heated with one of potassium permanganate, anisaldehyde or vanillin as appropriate. Retention factors (Rf) are reported in parentheses along with the solvent system used. Flash column chromatography was performed according to the method reported by W. C. Still *et al.*¹ using Fluorochem 60 Å silica gel (particle size 40–63 μm) and a solvent system as reported in the text.

1.2. Instrument details for compound characterisation purposes

NMR spectra were obtained in the solvent indicated, using a JEOL ECX400 or JEOL ECS400 spectrometer (400 MHz, 101 MHz and 377876 MHz for ¹H, ¹³C and ¹⁹F, respectively). Chemical shifts are reported in parts per million and were referenced to the residual undeuterated solvent of the deuterated solvent used (CHCl₃ TMH = 7.26 and TMC = 77.16 (CDCl₃), CDHCl₂ TMH = 5.31 and TMC = 54.0 (CD₂Cl₂), ¹H and ¹³C, respectively). Spectra were typically run at a temperature of 298 K. All ¹³C NMR spectra were obtained with ¹H decoupling. NMR spectra were processed using MestReNova software (versions 5.3, 7.03 and 8.1). The spectra given below were saved as .TIF files in MestReNova and inserted directly into a Microsoft Word Document. For the ¹H NMR spectra the resolution varies from 0.15 to 0.5 Hz; the coupling constants have been quoted to ± 0.5 Hz in all cases for consistency. ¹H NMR chemical shifts are quoted to 2 decimal places; ¹³C and ¹⁹F NMR chemical shifts are quoted to 1 decimal place. Numbers were rounded to the nearest value, e.g. 1.237 ≈ 1.24, 1.232 ≈ 1.23.

Infrared spectra were obtained using either a Unicam Research Series FTIR (KBr-IR) or a Bruker ALPHA-Platinum FTIR Spectrometer with a platinum-diamond ATR sampling module, in a NaCl window solution cell. All cyanation kinetics and complimentary studies were followed using a Mettler Toledo React-IR spectrometer with a silicon probe and K6 conduit/R4 (mirror arm). IR spectra are taken in real-time every 60 seconds between 4000 and 649 cm⁻¹, with a spectral resolution of 4 cm⁻¹. All reaction temperatures were measured independently from the heating bath using a TENMA 72-7715 electronic thermometer and thermocouple to ensure accurate reaction temperature regulation. All data analysis was carried out on raw, uncorrected data. The reaction profile data shown in the manuscript has been smoothed using a moving four-point average.

MS spectra were measured using a Bruker Daltonics micrOTOF MS, Agilent series 1200LC with electrospray ionisation (ESI and APCI) or on a Thermo LCQ using electrospray ionisation, with <5 ppm error recorded for all HRMS samples. LIFDI mass spectrometry was carried out using a Waters GCT Premier MS Agilent 7890A GC (usually for analysis of organometallic compounds when ESI or APCI are not satisfactory ionisation methods). Mass spectral data is quoted as the *m/z* ratio along with the relative peak height in brackets (base peak = 100). Mass to charge ratios (*m/z*) are reported in Daltons. High resolution mass spectra are reported with <5 ppm error (ESI) or <20 ppm error (LIFDI). For clarity, LIFDI data are reported for ¹⁰⁶Pd, the most abundant natural isotope of Pd. Melting points were recorded using a Stuart digital SMP3 machine.

2. Mechanistic and kinetic studies

2.1. General procedure: React-IR kinetic studies of Pd-catalysed arylcyanations

All arylcyanations of **2** monitored using *in situ* infrared spectroscopy were performed using the following general procedure. All adaptations were carried out as appropriate, according to the experiment reported *e.g.* addition of water; changing reagent concentrations; reaction temperature changes, but the orders of addition and a final reaction volume of 7 ml were maintained throughout.

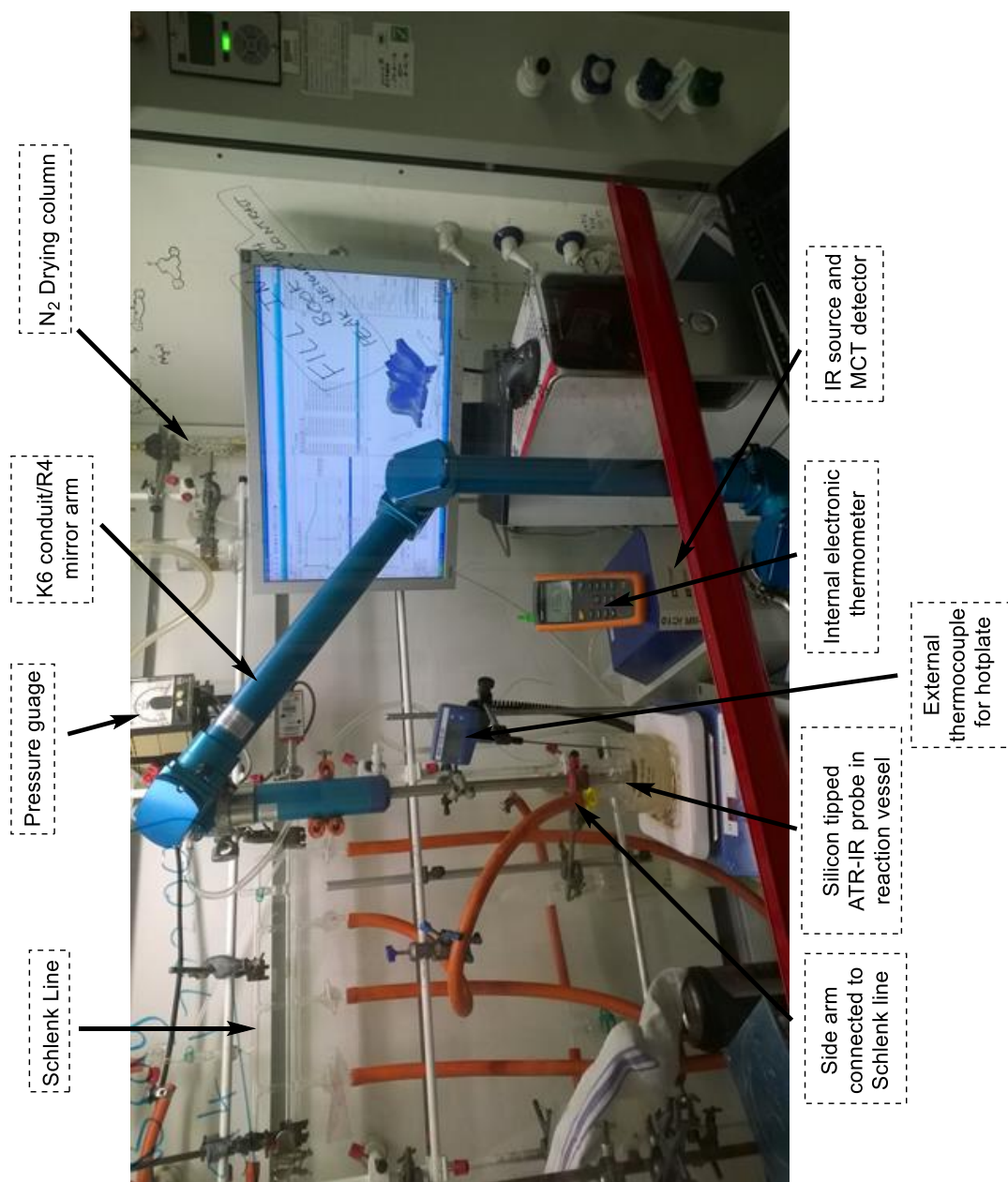
An annotated picture of the experimental set up is displayed in Supplementary Figure 1. An oven dried, 100 ml three necked round bottomed flask equipped with a small stirrer bar was attached to the React-IR, then backfilled with nitrogen three times. At all points of the experiment hereafter, the reaction vessel was open to a steady flow of N₂. In parallel, a small oven dried Schlenk tube was charged with catalyst (10 mg.) and backfilled with nitrogen three times.

After backfilling the round bottomed flask with dry N₂, a background spectrum was collected and then dry, degassed DMAc added (6 ml). At this point a reference spectrum was recorded with stirring. After sequence initiation, the reaction was stirred at room temperature for 5 minutes, before being heated to reaction temperature (as monitored by the internal thermocouple) by being placed in a silicon oil bath set to an appropriate level above the desired reaction temperature. After the reaction mixture reached the correct temperature, the solvent was stirred for a further five minutes and a spectrum used as a reference. To the hot solvent was then added the Na₂CO₃ (0.25 – 1 eq., freshly ground in a pestle and mortar) and was stirred for a further 5 minutes. After the system reached equilibrium, the cyanating agent {K₄[Fe(CN)₆]·3H₂O or K₄[Fe(CN)₆], 0.167 – 0.5 eq., freshly ground in a pestle and mortar} was added and stirred for 5 minutes. A spectrum was then selected as a second reference. To the mixture was then added *N*-benzyl-4-bromo-6-methylpyridin-2-one (**2**, 1 eq.), and the sides of the flask rinsed with dry, degassed DMAc (0.5-1 ml, adding the appropriate amount to make the *final total reaction volume* up to 7 ml) *via* a septum. The reaction mixture was then stirred for 5 minutes, to allow for temperature equilibration back to the desired reaction temperature and dissolution of the substrate. During this time the appropriate amount of dry, degassed DMAc was added to the small Schlenk containing the precatalyst to make a stock solution. All catalyst stock solutions were made to a concentration of 25 mmol dm⁻³ prior to their addition to reaction mixtures. After the reaction mixture had achieved a constant temperature and immediately after complete dissolution of the catalyst, the reaction was initiated by addition of an appropriate quantity of catalyst stock solution using a syringe to the round bottomed flask *via* a septum.

The reaction progress was monitored by measuring the increase in absorbance at 2238 cm⁻¹, corresponding to the product's nitrile stretch. After the absorbance at 2238 cm⁻¹ had reached a constant value (indicating reaction completion) the experiment was stopped, and the reaction mixture allowed to *cool to room temperature*. Once the mixture had cooled, the final conversion of each reaction was measured by direct ¹H NMR spectroscopic analysis of the crude reaction mixture. An aliquot of the reaction mixture was filtered through a small Celite/cotton wool plug to remove any organic-insoluble salts and diluted with CDCl₃ before running the NMR experiment. The final conversion was calculated by measuring the ratio of

the diagnostic peaks at 6.80 ppm for N-benzyl-4-bromo-6-methylpyridin-2-one (**2**) and 6.85 ppm for N-benzyl-4-cyano-6-methylpyridin-2-one (**3**).

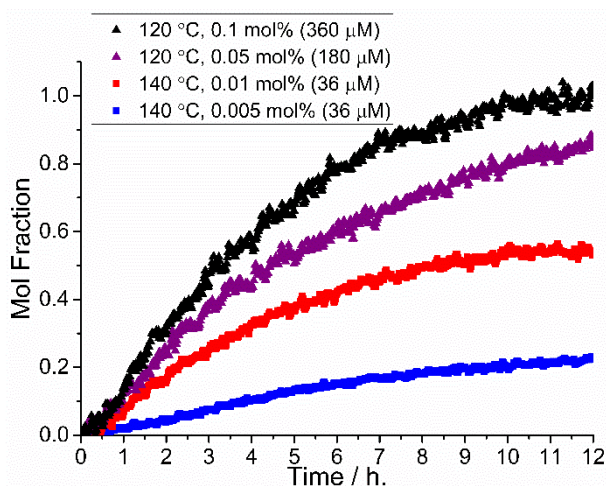
All peak absorption data for 2238 cm^{-1} , 2045 cm^{-1} and any other peaks of interest were exported into Excel in three forms: i) with no reference subtraction; ii) after subtraction of a reference spectrum of DMAc at reaction temperature; iii) after subtraction of a reference spectrum of the reaction mixture before substrate addition, at reaction temperature °C. All subsequent analysis was carried out on dataset iii). All kinetic traces (conversions) were normalised using the final reaction conversion (as calculated *vide supra*) and the absorption value of an appropriate data point at 2238 cm^{-1} (mid data scatter) after reaction completion. All data was smoothed with a moving four-point average.



Supplementary Figure 1 | Picture of experimental set up for kinetic experiments using the React IR.

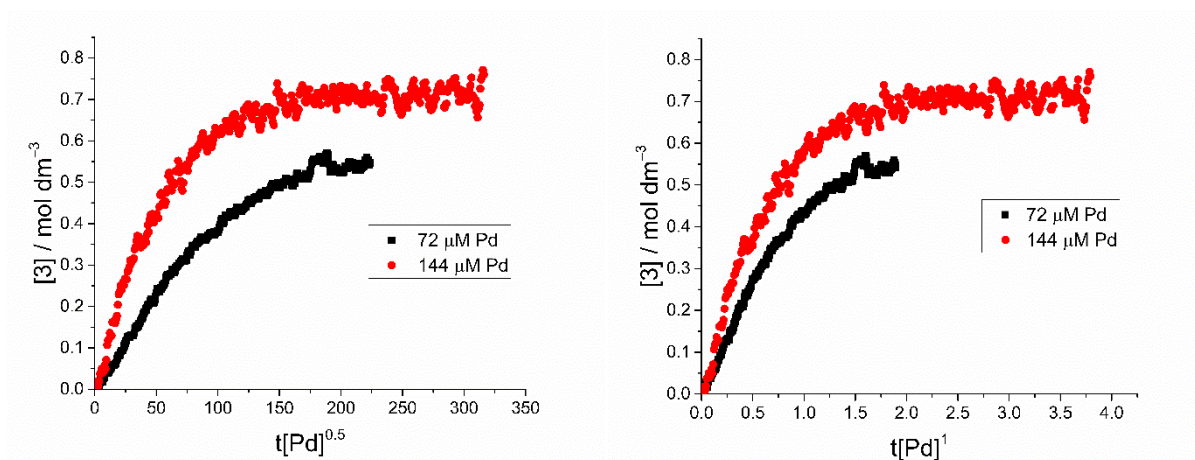
2.2. Catalyst loading and temperature effects of catalyst efficiency under anhydrous conditions.

Investigation into the effect of temperature and Pd catalyst loading shows that under ‘low water’ conditions, at slightly increased catalyst loadings (0.05 mol%, 180 μ M) **1-pip** performs as an effective catalyst when the temperature is decreased to 120 $^{\circ}$ C; doubling this catalyst loading (0.1 mol%, 360 μ M) does not result in a doubled initial rate (Supplementary Figure 2). When performing the reaction at very low catalyst loadings (0.01 – 0.005 mol%,) it is necessary to increase the reaction temperature to 140 $^{\circ}$ C and optimize [Pd], as shown in the main manuscript, Figure 5.



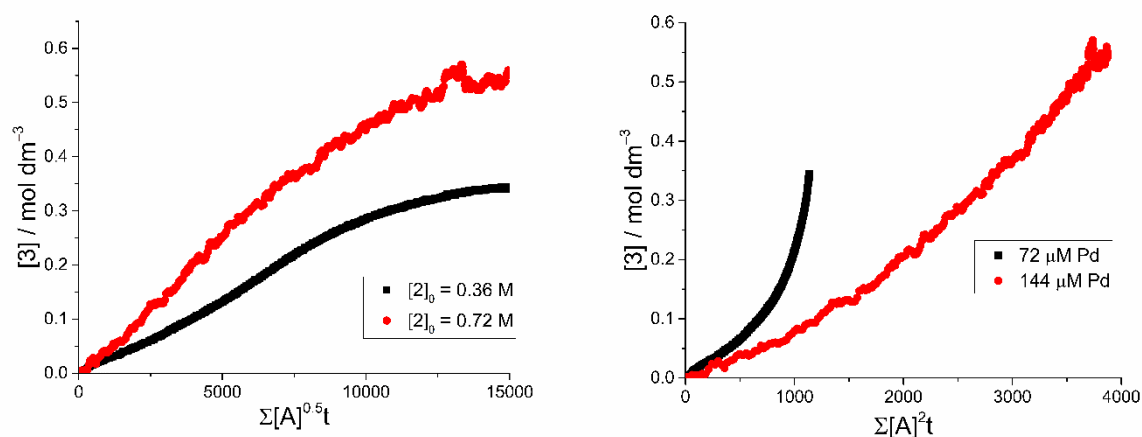
Supplementary Figure 2 | Reaction profiles for the reaction of 2 to give 3 at different 1-pip catalyst loadings, [Pd] and reaction temperatures under pseudo-anhydrous conditions (data points cut-off at 12 h). Reaction conditions: 1-pip (0.005 – 0.1 mol%), $K_4[Fe(CN)_6]$ (0.22 eq.), Na_2CO_3 (1 eq.), DMAc, N_2 , 120–140 °C. Data cut off at 12 h. [2] at catalyst loadings: 0.005 mol%: 0.72 M; 0.01 – 0.1 mol%: 0.36 M.

2.3. Determination of order w.r.t. 1-pip



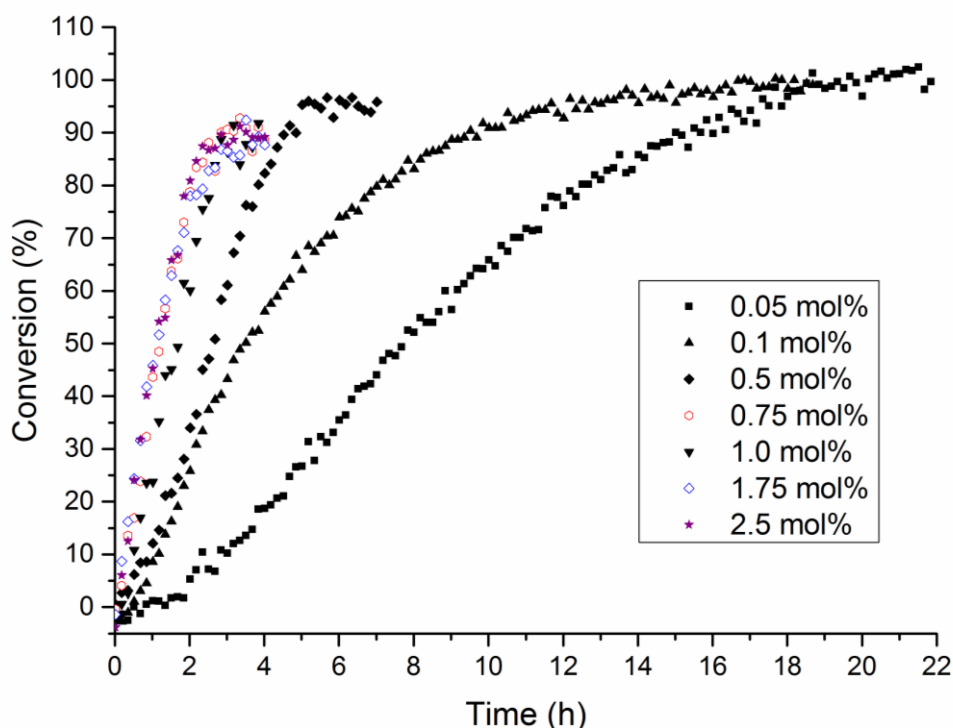
Supplementary Figure 3 | Using the Bures time normalisation method, orders of reaction with respect to Pd of 0.5 and 1 were ruled out. By comparison, the graphical fit of the two reaction profiles in Figure 4a of the manuscript show significantly better overlap when the concentration of Pd is raised to the power of 2.

2.4. Determination of order w.r.t. 2



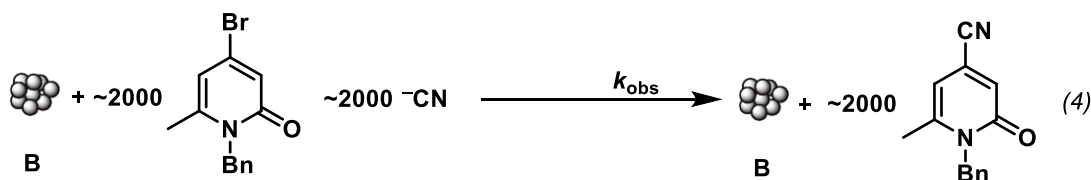
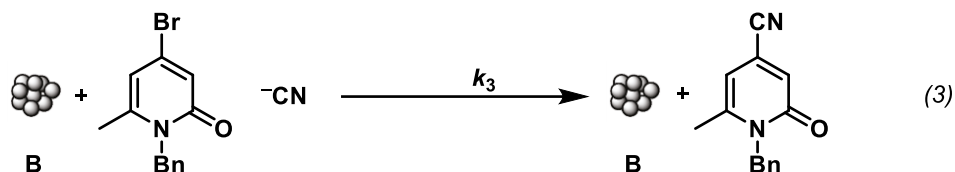
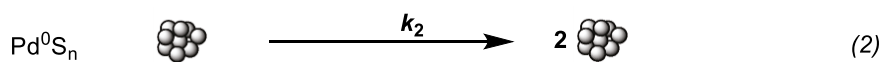
Supplementary Figure 4 | Using the Bures time normalisation method, orders of reaction with respect to **2** of 0.5 and 2 were ruled out. By comparison, the graphical fit of the two reaction profiles in Figure 6(bottom) of the manuscript show significantly better overlap when the concentration of **2** is raised to the power of 1.

2.5. Catalyst loading investigations with **1-pip**, using $K_4[Fe(CN)_6] \cdot 3H_2O$



Supplementary Figure 5 | All catalyst loading kinetic investigations of **1-pip** under hydrous conditions. Reaction conditions: **1-pip** (0.05 mol% - 2.5 mol%), $K_4[Fe(CN)_6] \cdot 3H_2O$ (0.22 eq.), Na_2CO_3 (1 eq.), DMAc, N_2 , 120 °C.

2.6. Finke-Watzky curvefits for sigmoidal kinetic plots



Supplementary Figure 6 | The Finke-Watzky nucleation and autocatalytic growth mechanism. Provided $k_3 \gg k_2 > k_1$ it is possible to calculate the values of k_1 and k_2 using the kinetics for the summative pseudoelementary step (4).2

All data treatments were devised after careful incorporation of the protocol provided by Kemmer and Keller³ for nonlinear least-squares data fitting with the integrated rate equation for the 2-step, Finke-Watzky nucleation and autocatalytic growth mechanism (Equation 1).

$$[A]_t = \frac{\frac{k_1}{k_2} + [A]_0}{1 + \frac{k_1}{k_2 [A]_0} \times e^{(k_1 + k_2 [A]_0)t}}$$

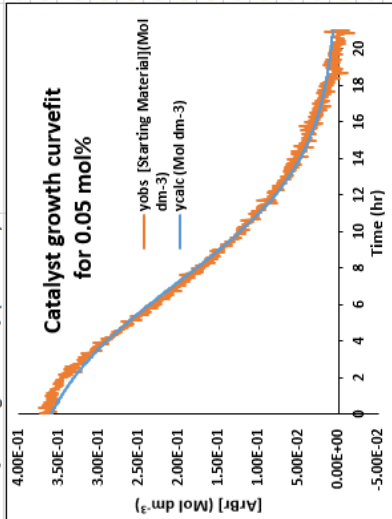
Equation 1 | The integrated rate equation for the 2-step, Finke-Watzky nucleation and autocatalytic growth mechanism (F-W 2-step mechanism).

Supplementary Figure 7 shows a screenshot of the spreadsheet, with formulae shown, used to calculate each curvefit. Where: k_1 (cell B1) is the calculated rate of nucleation; k_2 (cell B2) is the calculated rate of catalytic surface growth; corrected k_2 (cell B3) is the calculated rate of autocatalytic surface growth corrected to include the correct catalyst : substrate ratio; X (column C) is the time of reaction progression in hours; Y_{obs} (column E) is the concentration of starting material, calculated from the known concentration of product in column D; Y_{calc} (column F) is the calculated concentration of starting material according to Supplementary Figure 7; δ^2 (column G) is the square residual between Y_{obs} and Y_{calc} .

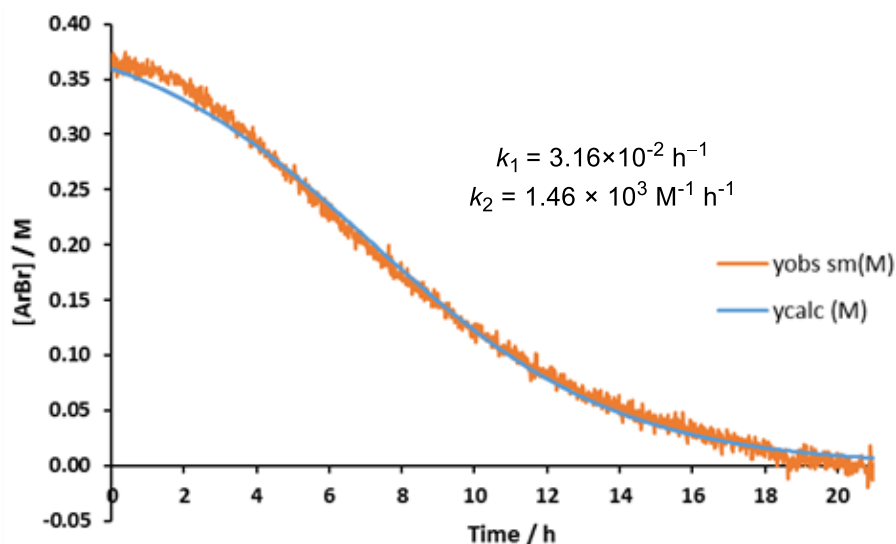
In order to calculate a sum of least squares fit, Excel Solver must be used to optimise the Sum of Square Residuals (SSR) (**Set Target Cell**, B4), to the **Value of: 0, Subject To The Constraints**, B2>0.000001. The adjustable parameters in this instance are k_1 and k_2 and can

be set in Solver by defining the field "By Changing Cells" as cells B1 and B2. By setting the SSR to 0 rather than minimum, this reduces the likelihood of Solver getting stuck in a local minima. However when using experimental data it is often very unlikely for this to reduce to zero and causes Solver to open an error window stating that a solution was unable to be found; this error message can be ignored.

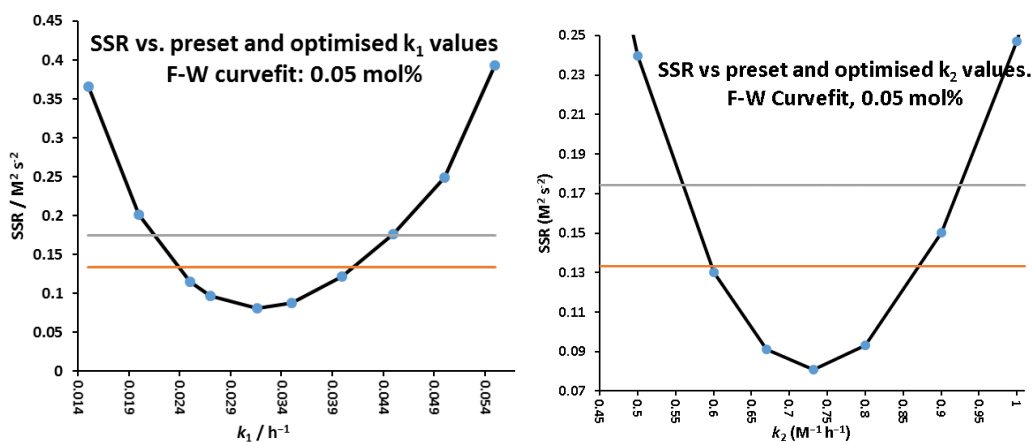
A	B	C	D	E	F	G
1	k_1	0.0316358174870607	[product] (Mol dm ⁻³)	Y_{obs} [Starting Material](Mol dm ⁻³)	Y_{calc} (Mol dm ⁻³)	δ^2 ((Mol dm ⁻³) ² s ⁻²)
2	k_2	0.73145015269432	-0.00005439=- $\$B\6 -D2		$=((\$B\$1/(\$B\$2)+\$E\$2)/(1+(\$B\$1/(\$B\$2)*\$E\$2)))*EXP((\$B\$1+(\$B\$2)*\$E\$2)*\$C2)$	$=\$E2-F2^{\wedge}2$
3	corrected k_2 (stoic factor)	$=B2*2000$	-0.00412966=- $\$B\6 -D3		$=((\$B\$1/(\$B\$2)+\$E\$2)/(1+(\$B\$1/(\$B\$2)*\$E\$2)))*EXP((\$B\$1+(\$B\$2)*\$E\$2)*\$C3)$	$=\$E3-F3^{\wedge}2$
4	Sum of Square Residuals	$=SUM(G2:G1320)$	0.0333333333333333	-0.00135633=- $\$B\6 -D4	$=((\$B\$1/(\$B\$2)+\$E\$2)/(1+(\$B\$1/(\$B\$2)*\$E\$2)))*EXP((\$B\$1+(\$B\$2)*\$E\$2)*\$C4)$	$=\$E4-F4^{\wedge}2$
5	mol SM @T0:	0.00251	0.05	-0.01386219=- $\$B\6 -D5	$=((\$B\$1/(\$B\$2)+\$E\$2)/(1+(\$B\$1/(\$B\$2)*\$E\$2)))*EXP((\$B\$1+(\$B\$2)*\$E\$2)*\$C5)$	$=\$E5-F5^{\wedge}2$
6	Initial [Starting material] (mol dm ⁻³)	0.359	0.0666666666666666	-0.01194137=- $\$B\6 -D6	$=((\$B\$1/(\$B\$2)+\$E\$2)/(1+(\$B\$1/(\$B\$2)*\$E\$2)))*EXP((\$B\$1+(\$B\$2)*\$E\$2)*\$C6)$	$=\$E6-F6^{\wedge}2$
7	4.00E-01		0.0833333333333333	-0.00372714=- $\$B\6 -D7	$=((\$B\$1/(\$B\$2)+\$E\$2)/(1+(\$B\$1/(\$B\$2)*\$E\$2)))*EXP((\$B\$1+(\$B\$2)*\$E\$2)*\$C7)$	$=\$E7-F7^{\wedge}2$
8	3.50E-01		0.1	-0.00413575=- $\$B\6 -D8	$=((\$B\$1/(\$B\$2)+\$E\$2)/(1+(\$B\$1/(\$B\$2)*\$E\$2)))*EXP((\$B\$1+(\$B\$2)*\$E\$2)*\$C8)$	$=\$E8-F8^{\wedge}2$
9	3.00E-01		0.1166666666666666	-0.00745399=- $\$B\6 -D9	$=((\$B\$1/(\$B\$2)+\$E\$2)/(1+(\$B\$1/(\$B\$2)*\$E\$2)))*EXP((\$B\$1+(\$B\$2)*\$E\$2)*\$C9)$	$=\$E9-F9^{\wedge}2$
10	3.00E-01		0.1333333333333333	-0.00935274=- $\$B\6 -D10	$=((\$B\$1/(\$B\$2)+\$E\$2)/(1+(\$B\$1/(\$B\$2)*\$E\$2)))*EXP((\$B\$1+(\$B\$2)*\$E\$2)*\$C10)$	$=\$E10-F10^{\wedge}2$
11	2.50E-01		0.15	0.006863441=- $\$B\6 -D11	$=((\$B\$1/(\$B\$2)+\$E\$2)/(1+(\$B\$1/(\$B\$2)*\$E\$2)))*EXP((\$B\$1+(\$B\$2)*\$E\$2)*\$C11)$	$=\$E11-F11^{\wedge}2$
12	2.00E-01		0.1666666666666666	-0.00497656=- $\$B\6 -D12	$=((\$B\$1/(\$B\$2)+\$E\$2)/(1+(\$B\$1/(\$B\$2)*\$E\$2)))*EXP((\$B\$1+(\$B\$2)*\$E\$2)*\$C12)$	$=\$E12-F12^{\wedge}2$
13	2.00E-01		0.1833333333333333	-0.00448222=- $\$B\6 -D13	$=((\$B\$1/(\$B\$2)+\$E\$2)/(1+(\$B\$1/(\$B\$2)*\$E\$2)))*EXP((\$B\$1+(\$B\$2)*\$E\$2)*\$C13)$	$=\$E13-F13^{\wedge}2$
14	1.50E-01		0.2	0.003399341=- $\$B\6 -D14	$=((\$B\$1/(\$B\$2)+\$E\$2)/(1+(\$B\$1/(\$B\$2)*\$E\$2)))*EXP((\$B\$1+(\$B\$2)*\$E\$2)*\$C14)$	$=\$E14-F14^{\wedge}2$
15	1.00E-01		0.2166666666666666	-0.0010453=- $\$B\6 -D15	$=((\$B\$1/(\$B\$2)+\$E\$2)/(1+(\$B\$1/(\$B\$2)*\$E\$2)))*EXP((\$B\$1+(\$B\$2)*\$E\$2)*\$C15)$	$=\$E15-F15^{\wedge}2$
16	1.00E-01		0.2333333333333333	0.00140224=- $\$B\6 -D16	$=((\$B\$1/(\$B\$2)+\$E\$2)/(1+(\$B\$1/(\$B\$2)*\$E\$2)))*EXP((\$B\$1+(\$B\$2)*\$E\$2)*\$C16)$	$=\$E16-F16^{\wedge}2$
17	5.00E-02		0.25	-0.00608666=- $\$B\6 -D17	$=((\$B\$1/(\$B\$2)+\$E\$2)/(1+(\$B\$1/(\$B\$2)*\$E\$2)))*EXP((\$B\$1+(\$B\$2)*\$E\$2)*\$C17)$	$=\$E17-F17^{\wedge}2$
18	5.00E-02		0.2666666666666666	-0.00688173=- $\$B\6 -D18	$=((\$B\$1/(\$B\$2)+\$E\$2)/(1+(\$B\$1/(\$B\$2)*\$E\$2)))*EXP((\$B\$1+(\$B\$2)*\$E\$2)*\$C18)$	$=\$E18-F18^{\wedge}2$
19	0.00E+00		0.2833333333333333	0.00098335=- $\$B\6 -D19	$=((\$B\$1/(\$B\$2)+\$E\$2)/(1+(\$B\$1/(\$B\$2)*\$E\$2)))*EXP((\$B\$1+(\$B\$2)*\$E\$2)*\$C19)$	$=\$E19-F19^{\wedge}2$
20	-5.00E-02		0.3	0.00183592=- $\$B\6 -D20	$=((\$B\$1/(\$B\$2)+\$E\$2)/(1+(\$B\$1/(\$B\$2)*\$E\$2)))*EXP((\$B\$1+(\$B\$2)*\$E\$2)*\$C20)$	$=\$E20-F20^{\wedge}2$
21			0.3166666666666666	0.00515275=- $\$B\6 -D21	$=((\$B\$1/(\$B\$2)+\$E\$2)/(1+(\$B\$1/(\$B\$2)*\$E\$2)))*EXP((\$B\$1+(\$B\$2)*\$E\$2)*\$C21)$	$=\$E21-F21^{\wedge}2$



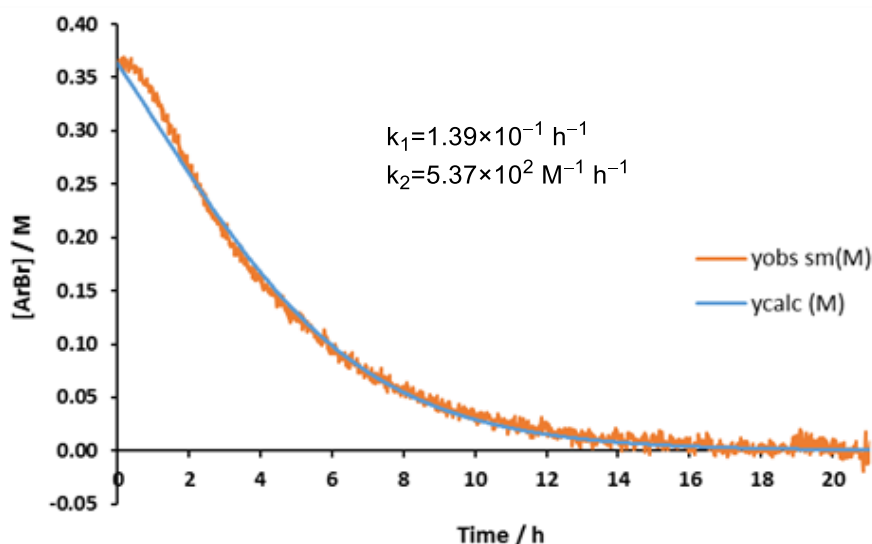
Supplementary Figure 7 | By incorporating Equation 1 into a nonlinear least-squares data fit, a suitable F-W 2-step mechanism curvefit can be achieved using Excel Solver for the consumption of starting material using 0.05 mol% **1-Pip** and $K_4[Fe(CN)_6] \cdot 3H_2O$.



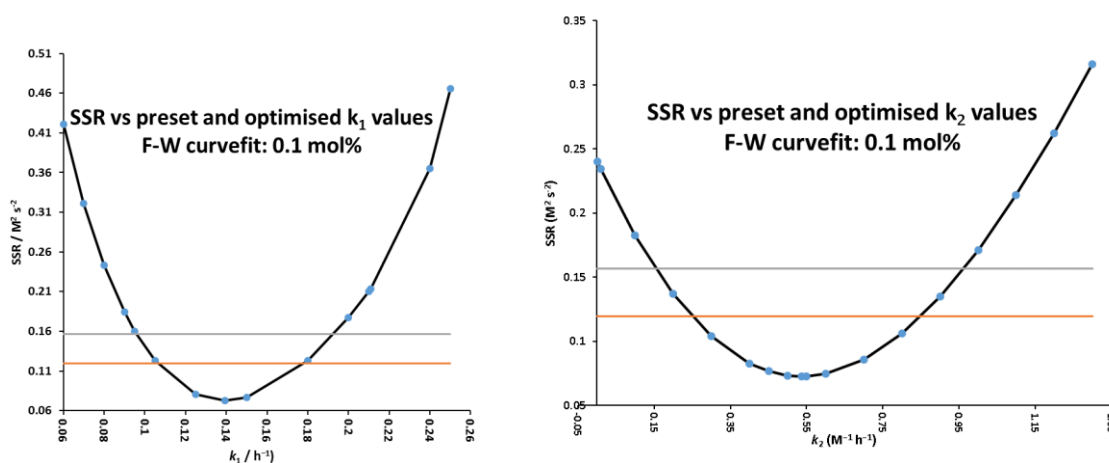
Supplementary Figure 8 | Concentration *vs.* time curve and data fit to the F-W 2-step mechanism for 0.05 mol% catalyst loading. The resultant rate constant k_2 has been corrected by using a stoichiometry factor of 2000. k_1 confidence intervals: 95% = $2.4 \times 10^{-2} - 4.1 \times 10^{-2} \text{ hr}^{-1}$; 99% = $2.15 \times 10^{-2} - 4.5 \times 10^{-2} \text{ hr}^{-1}$. k_2 confidence intervals: 95% = $1.2 \times 10^3 - 1.74 \times 10^3 \text{ M}^{-1} \text{ hr}^{-1}$; 99% = $1.12 \times 10^3 - 1.84 \times 10^3 \text{ M}^{-1} \text{ hr}^{-1}$.



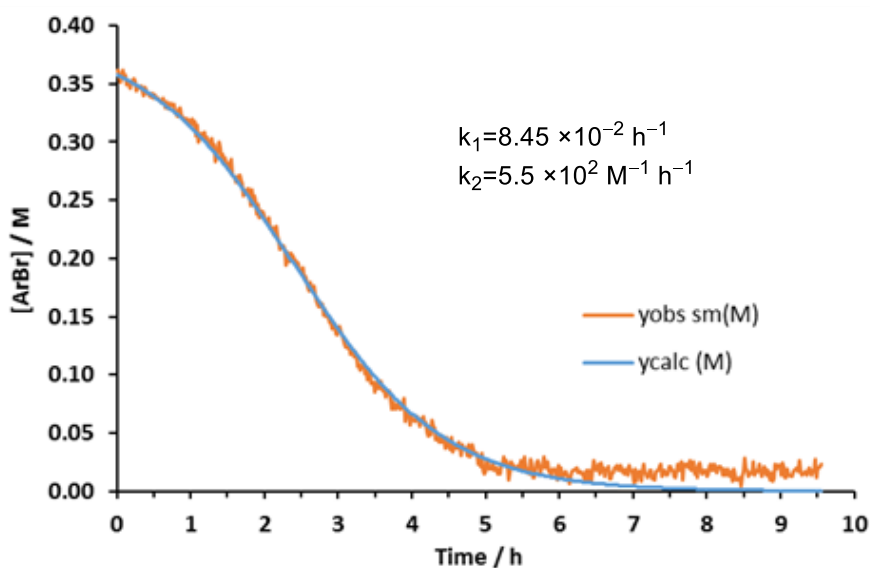
Supplementary Figure 9 | Visual representations of the 95% (brown line) and 99% (grey line) confidence limits for the F-W 2-step curvefit displayed in Supplementary Figure 8.



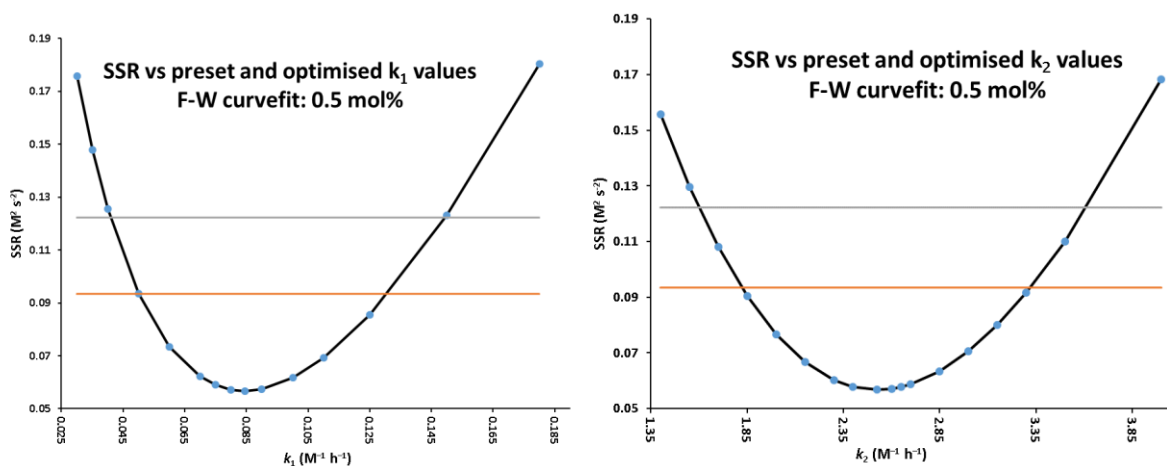
Supplementary Figure 10 | Concentration *vs.* time curve and data fit to the F-W 2-step mechanism for 0.1 mol% catalyst loading. The resultant rate constant k_2 has been corrected by using a stoichiometry factor of 1000. k_1 confidence intervals: 95% = $1.06 \times 10^{-1} - 1.78 \times 10^{-1} \text{ hr}^{-1}$; 99% = $9.6 \times 10^{-2} - 1.92 \times 10^{-1} \text{ hr}^{-1}$. k_2 confidence intervals: 95% = $2.5 \times 10^2 - 8.50 \times 10^2 \text{ M}^{-1} \text{ hr}^{-1}$; 99% = $1.6 \times 10^2 - 9.6 \times 10^2 \text{ M}^{-1} \text{ hr}^{-1}$.



Supplementary Figure 11 | Visual representations of the 95% (brown line) and 99% (grey line) confidence limits for the F-W 2-step curvefit displayed in Supplementary Figure 10.



Supplementary Figure 12 | Concentration vs. time curve and data fit to the F-W 2-step mechanism for 0.5 mol% catalyst loading. The resultant rate constant k_2 has been corrected by using a stoichiometry factor of 200. k_1 confidence intervals: 95% = $5 \times 10^{-2} - 1.3 \times 10^{-1} \text{ hr}^{-1}$; 99% = $0.04 - 0.15 \text{ hr}^{-1}$. k_2 confidence intervals: 95% = $3.6 \times 10^2 - 6.7 \times 10^2 \text{ M}^{-1} \text{ hr}^{-1}$; 99% = $3.2 \times 10^2 - 7.2 \times 10^2 \text{ M}^{-1} \text{ hr}^{-1}$.

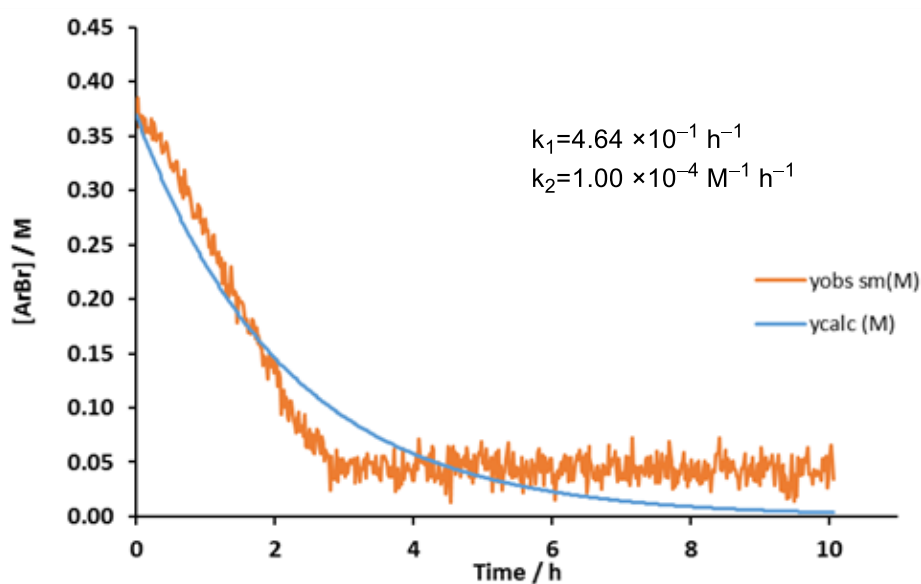


Supplementary Figure 13 | Visual representations of the 95% (brown line) and 99% (grey line) confidence limits for the F-W 2-step curvefit displayed in Supplementary Figure 12.

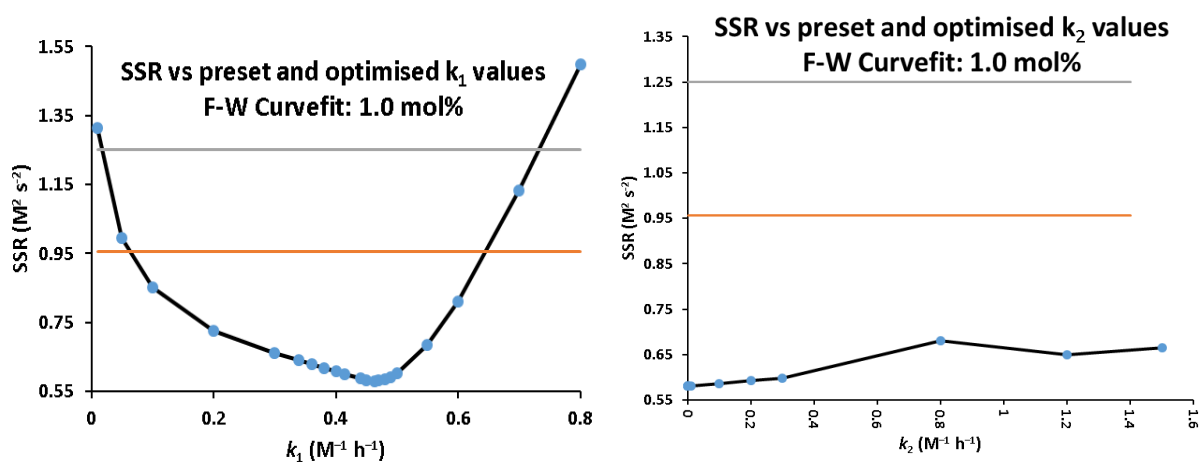
It is difficult to reliably correlate the relationship between increased induction period and decreased value of k_1 with only the three values from 0.05 and 0.1 ($3.16 \times 10^{-2} \text{ hr}^{-1}$ and $1.39 \times 10^{-1} \text{ hr}^{-1}$ respectively). However reflection, along with comparison with other literature values published by Finke and Watzke reveals that the two are directly linked. According to the confidence intervals obtained by manual confidence assessment using Fisher's F distribution, the curvefit for 0.05 mol% provides more precise values of k_1 and k_2 than the curvefit for 0.1 mol%. This implies that as catalyst concentrations increase (above $3.6 \times 10^{-4} \text{ mol dm}^{-3}$ /0.1 mol%) the mechanism deviates more and more from the F-W 2-step mechanism. This can be rationalised by the raised concentration of Pd in solution leading to a much faster nucleation step (k_1). It is important to remember here that in order for the F-W 2-step mechanism to be valid, the rate of continuous nucleation must be *much* lower than both the rate

of catalyst formation (k_2) by autocatalytic surface growth, and the overall rate of reaction (k_{obs}). Instead, it would be sensible to suggest that under these conditions Pd is reaching its critical agglomeration concentration. This means that autocatalysis may have a limited effect upon the rate of active catalyst (**B**) formation, so the F-W 2-step mechanism becomes an unsuitable model to apply. Analysis of the quality of the curvefit upon increasing the catalyst concentration to $1.8 \times 10^{-3} \text{ mol dm}^{-3}/0.5 \text{ mol\%}$ reveals that despite the kinetic traces appearing to be a good candidate for the F-W 2-step mechanism (sigmoidal reaction profile) further investigation reveals that the 95% confidence limits of both k_1 and k_2 are too wide. (Supplementary Figure 12, Supplementary Figure 13) and is representative of a poor fit to the kinetic model.

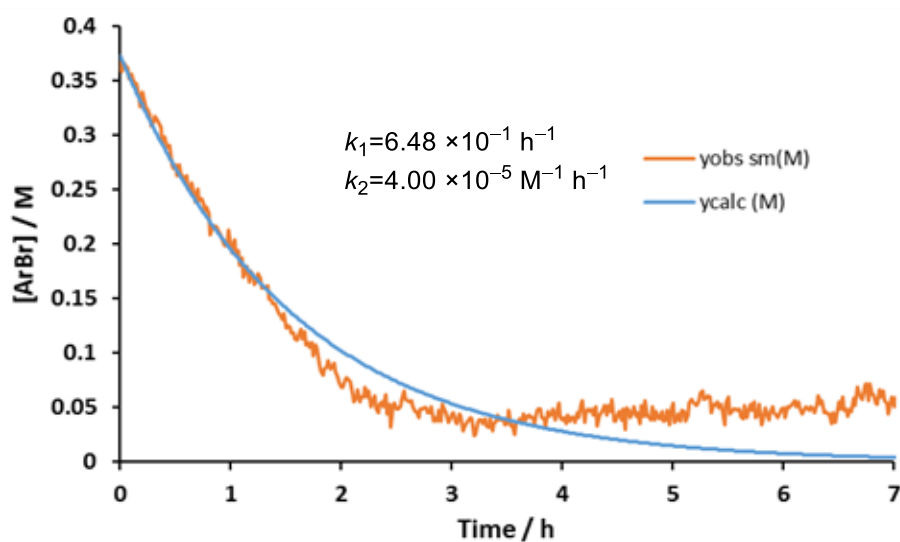
In contrast, at lower Pd concentration ($1.8 \times 10^{-4} \text{ mol dm}^{-3}/0.05 \text{ mol\%}$) the curvefit displayed in Supplementary Figure 8 is good, providing narrow 95% confidence intervals for both k_1 and k_2 ($1.7 \times 10^{-2} \text{ hr}^{-1}$ and $1.46 \times 10^3 \text{ M}^{-1} \text{ hr}^{-1}$, respectively) suggesting that the F-W 2-step mechanism provides a reasonable fit to explain the shape of the kinetic data obtained. Despite this, slight deviations away from the expected rate of catalyst formation are seen. A series of reasons for this are possible: i) the rate of formation of **A** is limited by the initial degradation (and therefore reduction) of the molecular catalyst which, in this kinetic fitting model, is not taken into account and therefore not been assigned a separate rate constant; ii) The F-W 2-step mechanism was designed around the Ir(0)₋₃₀₀ nanocluster catalysed hydrogenation of cyclohexene. This requires for the initial reduction of the Ir(I) precatalyst $[(1,5\text{-COD})\text{Ir}\cdot\text{P}_2\text{W}_{15}\text{Nb}_3\text{O}_{62}]^{8-}$ to be facilitated by an excess of H_2 . Further increasing catalyst concentration (and therefore loading) causes further deviation from the F-W 2-step mechanism:



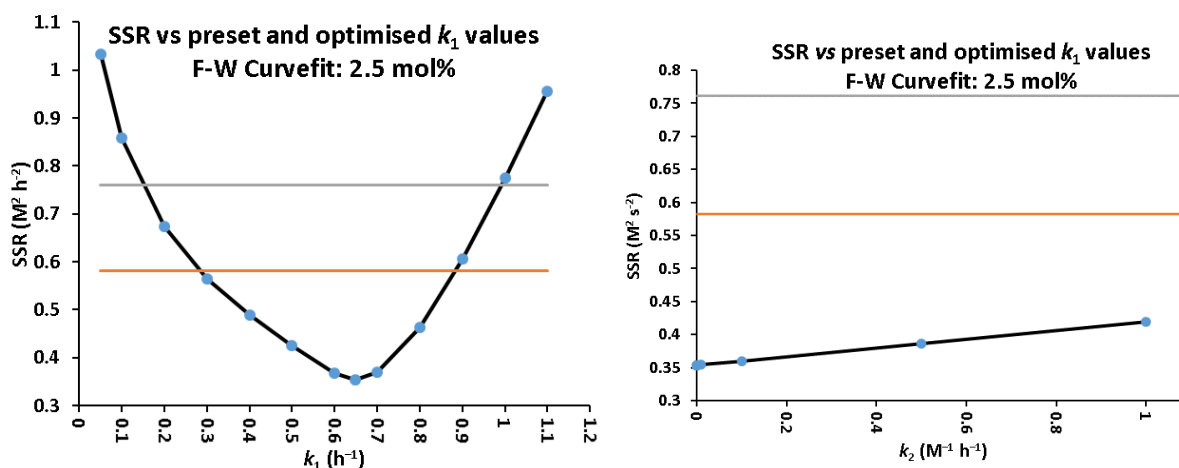
Supplementary Figure 14 | Concentration vs. time curve and data fit to the F-W 2-step mechanism for 1.0 mol% catalyst loading. k_1 confidence intervals: 95% = $6.0 \times 10^{-2} - 6.2 \times 10^{-1} \text{ hr}^{-1}$; 99% = $2.0 \times 10^{-2} - 7.3 \times 10^{-1} \text{ hr}^{-1}$. k_2 confidence intervals: 95% = N/A; 99%: N/A.



Supplementary Figure 15 | Visual representations of the 95% (brown line) and 99% (grey line) confidence limits for the F-W 2-step curvefit displayed in Supplementary Figure 14.

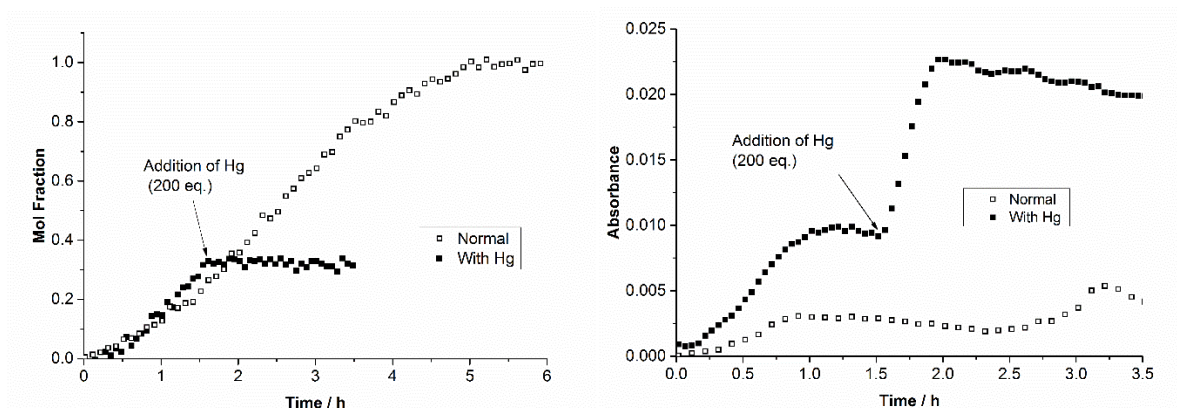


Supplementary Figure 16 | Concentration vs. time curve and data fit to the F-W 2-step mechanism for 2.5 mol% catalyst loading. k_1 confidence intervals: 95% = $2.8 \times 10^{-2} - 8.8 \times 10^{-1} \text{ hr}^{-1}$; 99% = $1.5 \times 10^{-1} - 9.5 \times 10^{-1} \text{ hr}^{-1}$. k_2 confidence intervals: 95% = N/A; 99%: N/A.



Supplementary Figure 17 | Visual representations of the 95% (brown line) and 99% (grey line) confidence limits for the F-W 2-step curvefit displayed in Supplementary Figure 16.

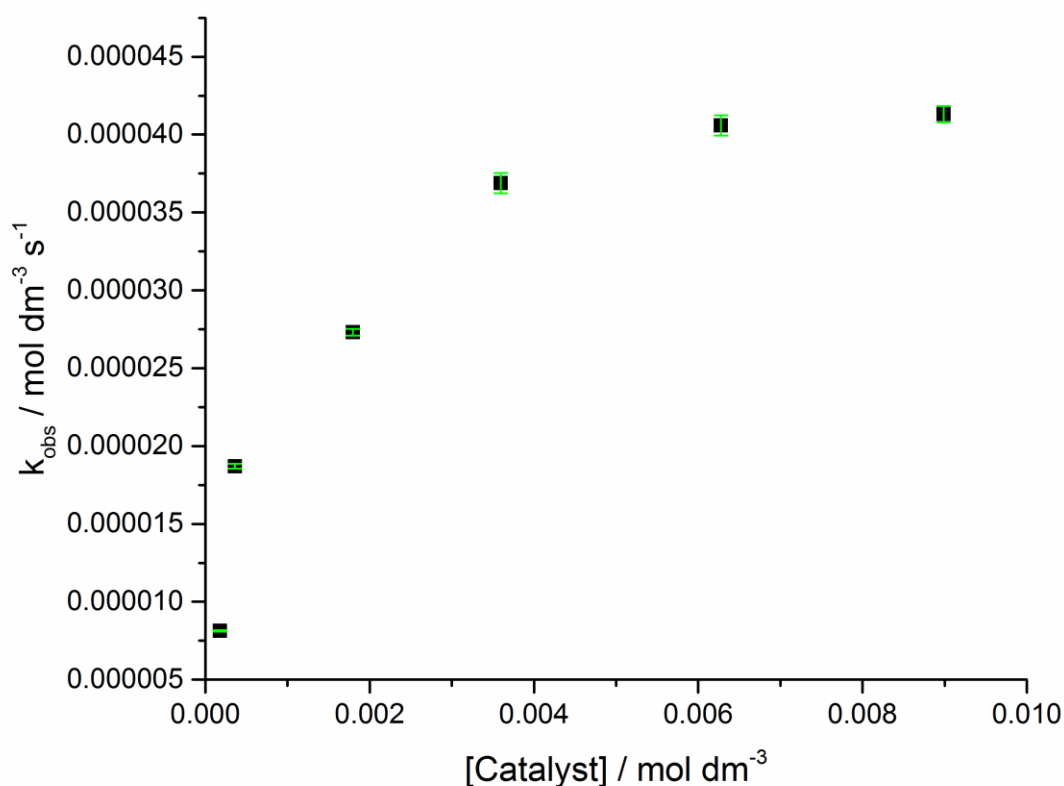
2.7. Hg drop test of reaction with $K_4[Fe(CN)_6] \cdot 3H_2O$



Supplementary Figure 18 | Comparison of rate of conversion of **2** under standard working conditions, vs. rate of dissolution of “[Fe(CN)₆]⁴⁻” (followed by monitoring absorbance at 2045 cm⁻¹). Reaction conditions: 1-pip (0.5 mol%), $K_4[Fe(CN)_6] \cdot 3H_2O$ (0.22 eq.), Na_2CO_3 (1 eq.), N_2 , 120 °C, DMAc. Hg (200 eq. w.r.t. Pd) added with vigorous stirring after 93 mins.

It is of interest to note that as the rate of catalysis increases under normal conditions (in the absence of Hg), after *ca.* 1 hour this rate competes with the rate of dissolution of “[Fe(CN)₆]⁴⁻”, at which point it appears to reach a steady state, drip feeding ⁻CN into the reaction mixture by a solubility dictated equilibrium. However, upon reaction quenching with Hg, a sharp increase in concentration of “[Fe(CN)₆]⁴⁻” occurs after all the catalytically competent Pd is sequestered and is no longer capable of maintaining a steady state concentration of “[Fe(CN)₆]⁴⁻”.

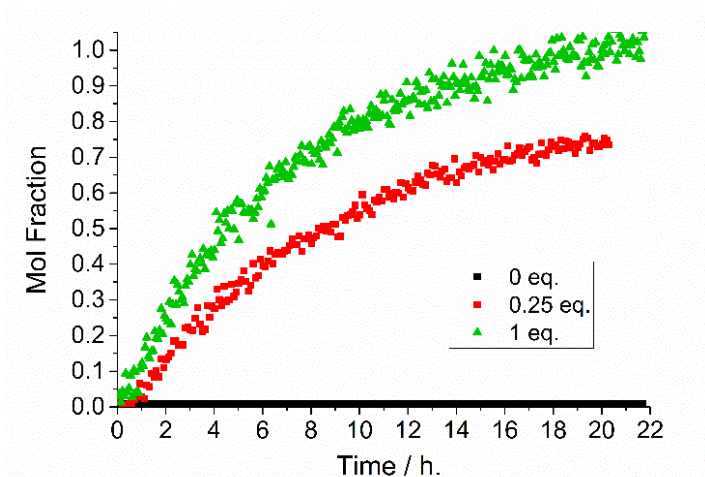
2.8. Catalyst loading k_{obs} relationship with $\text{K}_4[\text{Fe}(\text{CN})_6]\cdot 3\text{H}_2\text{O}$



Supplementary Figure 19 | A plot of k_{obs} vs. $[\text{Pd}]$ shows there is not a linear relationship between reaction rate and catalyst loading. Reaction conditions: 1-Pip (0.05 mol% - 2.5 mol%), $\text{K}_4[\text{Fe}(\text{CN})_6]\cdot 3\text{H}_2\text{O}$ (0.22 eq.), Na_2CO_3 (1 eq.), DMac, N_2 , 120 °C.

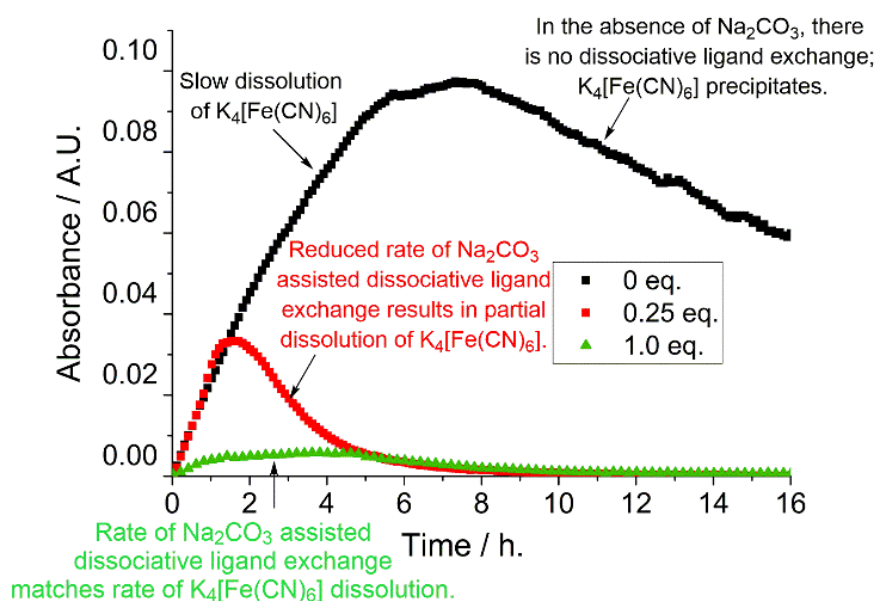
2.9. On the Role of Na_2CO_3 in aryl cyanations.

Despite an inorganic base being a common additive in Pd-catalyzed aryl cyanation reactions, there is little understanding regarding its precise function in terms of the catalytic cycle. Under Buchwald *et al.*'s conditions,⁴ only 0.25 eq. of NaOAc was required to facilitate quantitative conversion, thus a stoichiometric quantity is not necessary to effect efficient catalysis. It is hypothesized that NaOAc is directly involved in the release of CN^- from $\text{K}_4[\text{Fe}(\text{CN})_6]$, but no direct evidence was reported. Evidenced in Supplementary Figure 20 is efficient catalyst turnover upon reducing Na_2CO_3 equivalents from 1 to 0.25. However, instead of proceeding to quantitative conversion, the rate of reaction is lower; overall product conversion to **3** is lowered to 70%. Removing Na_2CO_3 from the reaction mixture completely results in no product formation at all.



Supplementary Figure 20 | Reaction profiles for formation of **3** with varied Na_2CO_3 equivalences. Reaction conditions: 1-pip (0.05 mol%), $[\text{Pd}] = 180 \mu\text{M}$, $\text{K}_4[\text{Fe}(\text{CN})_6]$ (0.22 eq.), Na_2CO_3 (0 – 1 eq.) DMAc, N_2 , $120 \text{ }^\circ\text{C}$.

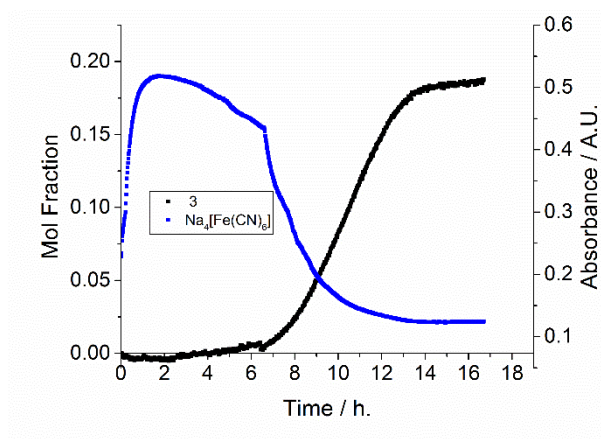
In all of the Pd-catalyzed aryl cyanations performed with $\text{K}_4[\text{Fe}(\text{CN})_6] \cdot \text{XH}_2\text{O}$, a characteristic infrared band at 2045 cm^{-1} occurs immediately after catalyst addition, characterized as solubilized $\text{K}_4[\text{Fe}(\text{CN})_6]$ by *ex situ* IR, following precipitation of a green solid after 8 hours (concomitant with decrease in absorbance at 2045 cm^{-1} , see black line, Supplementary Figure 21) when the reaction was performed in the absence of Na_2CO_3 . Following the 2045 cm^{-1} band throughout the reaction course gives traces as shown. Under standard conditions (1 eq. Na_2CO_3), the concentration of $\text{K}_4[\text{Fe}(\text{CN})_6]$ in the reaction is low during catalytic turnover. Reducing the amount of Na_2CO_3 to 0.25 eq. results in an increased concentration of $\text{K}_4[\text{Fe}(\text{CN})_6]$ over the reaction course. Removal of Na_2CO_3 from the reaction not only impedes product formation, but results in increased $\text{K}_4[\text{Fe}(\text{CN})_6]$ dissolution over time due to the lack of catalyst turnover. These findings support the proposition that Na_2CO_3 is involved in releasing CN^- from $\text{K}_4[\text{Fe}(\text{CN})_6]$, but that a favorable concentration of “[$\text{Fe}(\text{CN})_6$]” is critical.



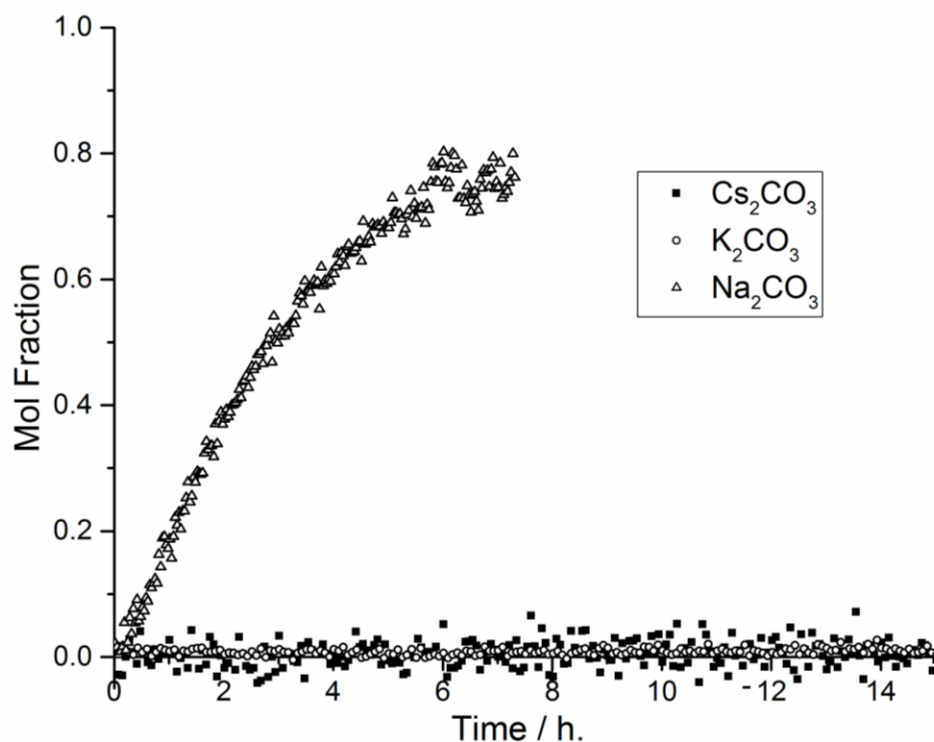
Supplementary Figure 21 | $[\text{Fe}(\text{CN})_6]$ (2045 cm^{-1}) traces with varied Na_2CO_3 equivalences. Reaction conditions: 1-pip (0.05 mol%), $[\text{Pd}] = 180 \mu\text{M}$, $\text{K}_4[\text{Fe}(\text{CN})_6]$ (0.22 eq.), Na_2CO_3 (0 – 1 eq.), DMAc, N_2 , $120 \text{ }^\circ\text{C}$.

Interestingly, changing to alternative carbonate salts (K_2CO_3 or Cs_2CO_3) as additives in the reaction catalyzed by **1-pip** resulted in a complete shutdown of the aryacyanation reaction. This is a resultant of differing hexacyanoferrate solubilities following partial counterion exchange, and can be observed by following the 2045 cm^{-1} absorbance by time resolved infrared spectroscopy. Replacing the carbonate additives with NaCl , NaBr and NaI facilitated limited conversions (7, 12 and 16% respectively) further confirming the importance of Na^+ in assisting “[$\text{Fe}(\text{CN})_6$]” solubility through salt metathesis and carbonate in facilitating efficient dissociative ligand exchange.

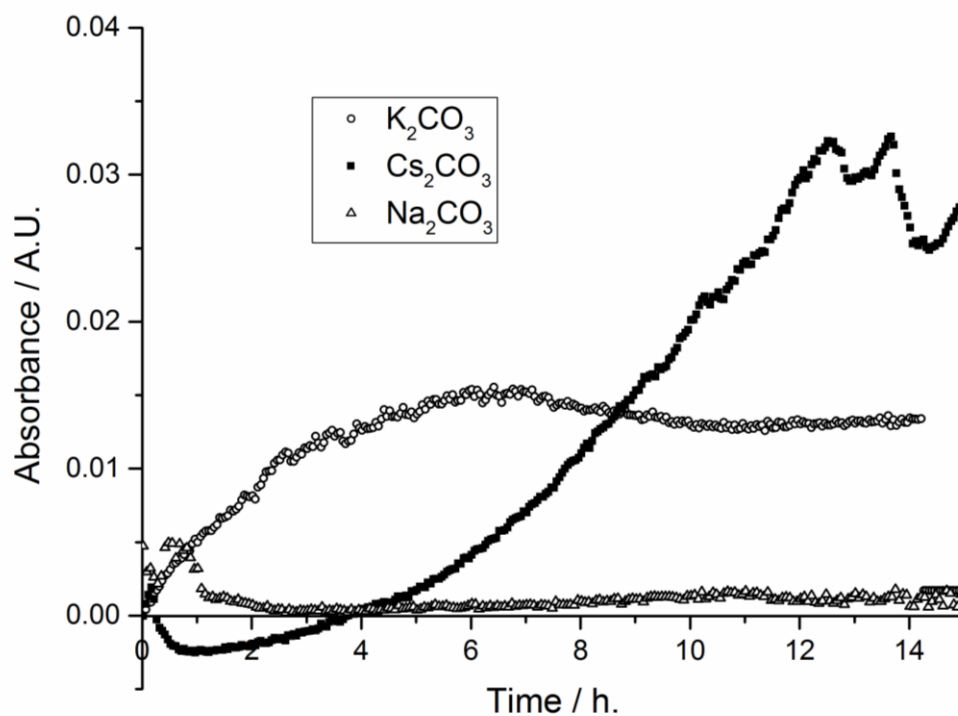
Importantly, replacement of $\text{K}_4[\text{Fe}(\text{CN})_6]$ with $\text{Na}_4[\text{Fe}(\text{CN})_6]$ in the presence of Na_2CO_3 (Table 1, entry 3) resulted in a depleted conversion of 16%. Kinetic analysis revealed an apparent increased solubility of $\text{Na}_4[\text{Fe}(\text{CN})_6]$ (observed at 2061 cm^{-1}), resulting in a reversion to a sigmoidal kinetic profile, and an induction period of 7 hours (Supplementary Figure 22). This shows that in the presence of higher concentrations of “[$\text{Fe}(\text{CN})_6$]” homogeneous Pd is catalytically incompetent; starting material consumption only occurs after the formation of heterogeneous, catalytically relevant Pd species. Again this is explained by the Finke-Watzky 2-step mechanism.²



Supplementary Figure 22 | Reaction profile when $\text{Na}_4[\text{Fe}(\text{CN})_6]$ was used as a cyanide source in the cyanation of **2**. Hexacyanoferrate absorbance followed at 2061 cm^{-1} . Reaction conditions: $\text{Na}_4[\text{Fe}(\text{CN})_6]$ (0.22 eq.), Na_2CO_3 (1 eq.), precatalyst **1-pip** (0.01 mol%, $72\text{ }\mu\text{M}$), DMAc , N_2 , $120\text{ }^\circ\text{C}$.

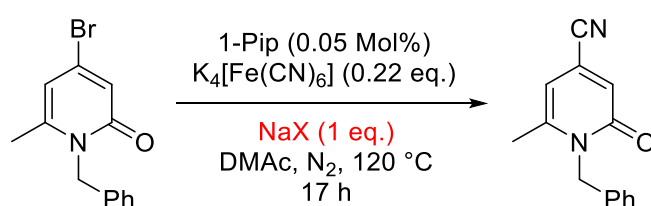


Supplementary Figure 23 | Reaction profiles for formation of cyanopyridone with different carbonate additives. Reaction conditions: Precatalyst **1-pip** (0.01 mol%, 72 μ M), $K_4[Fe(CN)_6]$ (0.22 eq.), X_2CO_3 (1 eq.), DMAc, N_2 , 140 $^\circ$ C.

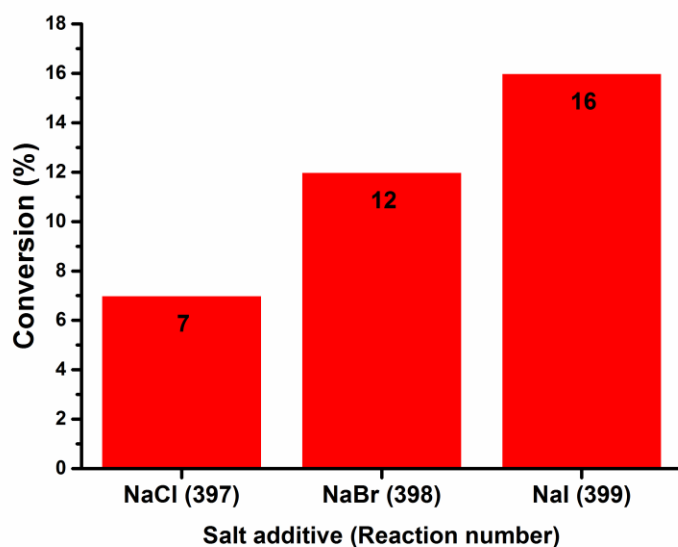


Supplementary Figure 24 | $Fe(CN)_6]_4^-$ traces in the attempted cyanation of 65 with different carbonate additives, shown in Supplementary Figure 23. Reaction conditions: Precatalyst **1-pip** (0.01 mol%, 72 μ M), $K_4[Fe(CN)_6]$ (0.22 eq.), X_2CO_3 (1 eq.), DMAc, N_2 , 140 $^\circ$ C.

The exact reason for this complete reaction shut-down was not entirely clear, but it was apparent that the cationic counterion of the additive is crucial to the mechanism by which the reaction transpires. Given that larger alkali metal counterions have lower solvation enthalpies, the inhibition of catalysis in the presence of K^+ and Cs^+ may have been due to the solvation of the alkali metal carbonates. Studying the $[Fe(CN)_6]^{4-}$ traces displayed in Supplementary Figure 24 showed that in the presence of Na^+ a normal trend was observed: the initial solvation of $[Fe(CN)_6]^{4-}$ followed by its consumption by catalysis. However, when K^+ was employed, $[Fe(CN)_6]^{4-}$ was still solubilised but not consumed by the formation of cyanated product. In the presence of Cs^+ , there was little solvation of $[Fe(CN)_6]^{4-}$ initially, however over a period of 6 hours its concentration did increase. Interestingly the concentration of $[Fe(CN)_6]^{4-}$ appeared to decrease upon the addition of Cs_2CO_3 ; this may be attributed to the counterion exchange between it and $K_4[Fe(CN)_6]$ resulting in a less soluble salt. Na^+ provides the optimal solubility conditions for effective catalysis to occur.



Supplementary Figure 25 | Reaction conditions to test alternative additives in the cyanation of **2**.



Supplementary Figure 26 | Replacing Na_2CO_3 with sodium halide salts still resulted in partial conversion of starting material. Different levels of reaction progression resulted in different coloured solutions, presumably due to the formation of different $K_xNa_y[Fe(CN)_z]$ species through counterion swapping and consumption of starting material.

2.10. On the behavior of alternative hexacyanoferrate salts.

Despite $\text{K}_4[\text{Fe}(\text{CN})_6] \cdot \text{XH}_2\text{O}$ being the most widely used iron-based cyanating agent, there are a range of commercial alternatives. ‘Soluble’ Prussian blue, $\text{KFe}[\text{Fe}(\text{CN})_6]$, was isolated as a side product in selected Pd-catalyzed cyanation reactions.⁴ Buchwald *et al.* therefore suggested that it is incapable of acting as a cyanating agent. Replacing $\text{K}_4[\text{Fe}(\text{CN})_6] \cdot \text{XH}_2\text{O}$ with $\text{KFe}[\text{Fe}(\text{CN})_6]$ in the reaction $2 \rightarrow 3$ confirmed the hypothesis, resulting in no product conversion. Repeating the reaction with 10 vol% degassed H_2O (in DMAc) to aid dissolution also resulted in no product conversion. This evidence, shows that catalysis is the most effective in the presence of $\text{K}_4[\text{Fe}(\text{CN})_6]$ and an inorganic sodium salt, which facilitates the dissolution of a $\text{Na}_x\text{K}_y[\text{Fe}(\text{CN})_6]$ species, where $x+y=4$, concomitant with favorable formation of NaBr , as opposed to KBr .

Table 1. Variation of the cyanide source.

Entry no.	Cyanide source ^a	Catalyst loading (mol%)	Conversion (%) ^b
1	$\text{KFe}[\text{Fe}(\text{CN})_6]$	0.5	0, 0 ^c
2	$\text{Na}_4[\text{Fe}(\text{CN})_6] \cdot 10\text{H}_2\text{O}$	0.05	0
3	$\text{Na}_4[\text{Fe}(\text{CN})_6]$	0.01	16
4	$\text{Na}_4[\text{Fe}(\text{CN})_6]$	0.05	50
5	$\text{Na}_4[\text{Fe}(\text{CN})_6]$	0.05	0 ^d
6	$\text{Na}_4[\text{Fe}(\text{CN})_6]$	0.1	0 ^d

^a Reaction conditions: 1-pip (0.5-0.01 mol%), “[$\text{Fe}(\text{CN})_6$]” (0.22 eq.), Na_2CO_3 (1 eq.), DMAc, N_2 , 120 °C, 5 h.

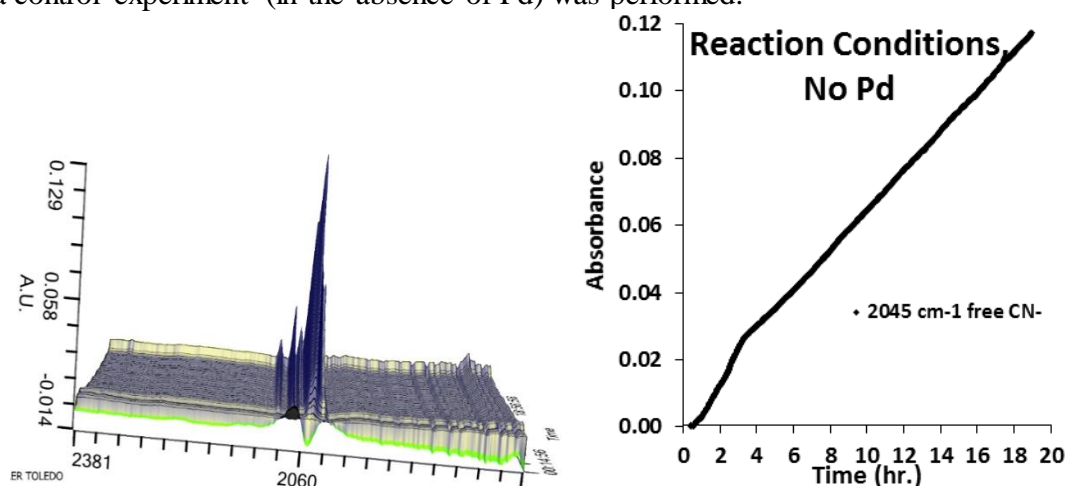
^b Determined by ¹H NMR spectroscopic analysis.

^c Reaction performed with 10 vol% degassed H_2O in DMAc to aid $\text{KFe}[\text{Fe}(\text{CN})_6]$ solubility.

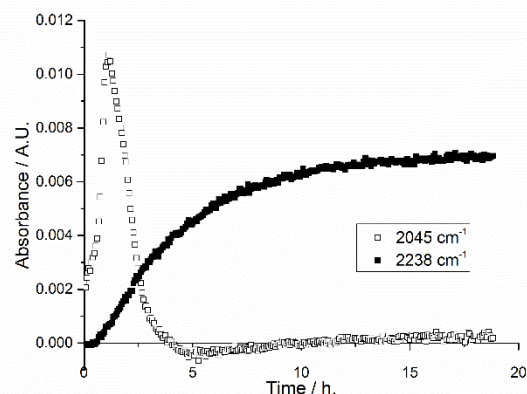
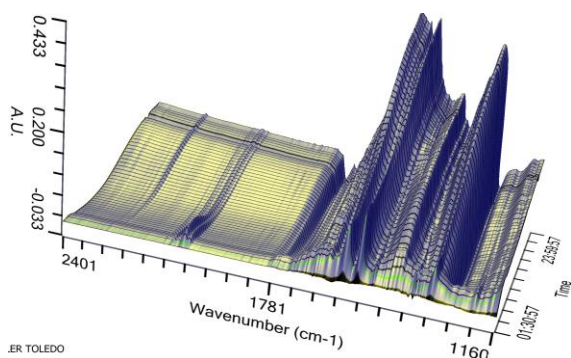
^d Without Na_2CO_3 .

2.11. Characterisation of “solubilised $[\text{Fe}(\text{CN})_6]^{4-}$ ”

In order to characterise the identity of the absorbance at 2045 cm^{-1} appearing in each reaction trace, a control experiment (in the absence of Pd) was performed.

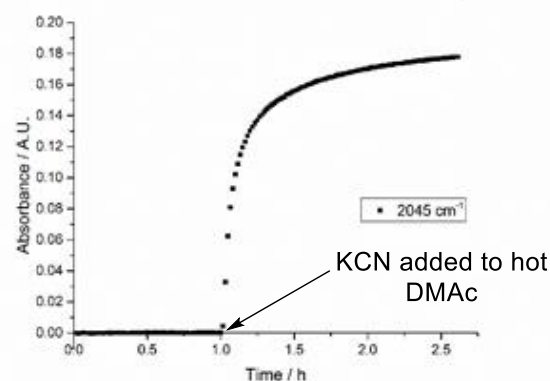
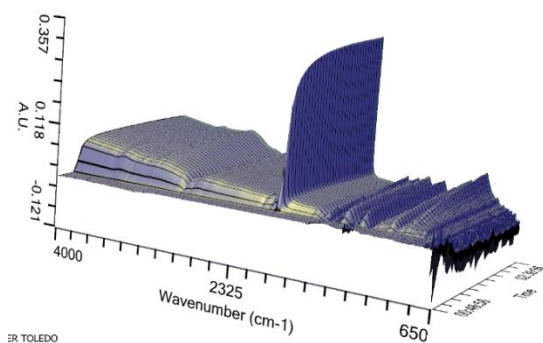


Supplementary Figure 27 | Standard reaction conditions in the absence of Pd led to slow growth of species at 2045 cm^{-1} . Left: In situ IR spectrum of $\text{K}_4[\text{Fe}(\text{CN})_6] \cdot 3\text{H}_2\text{O}$ (0.22 eq.), Na_2CO_3 (1 eq.) and 2 (1 eq.) in DMAc at 120 °C. Right: time resolved study of the absorbance at 2045 cm^{-1} .



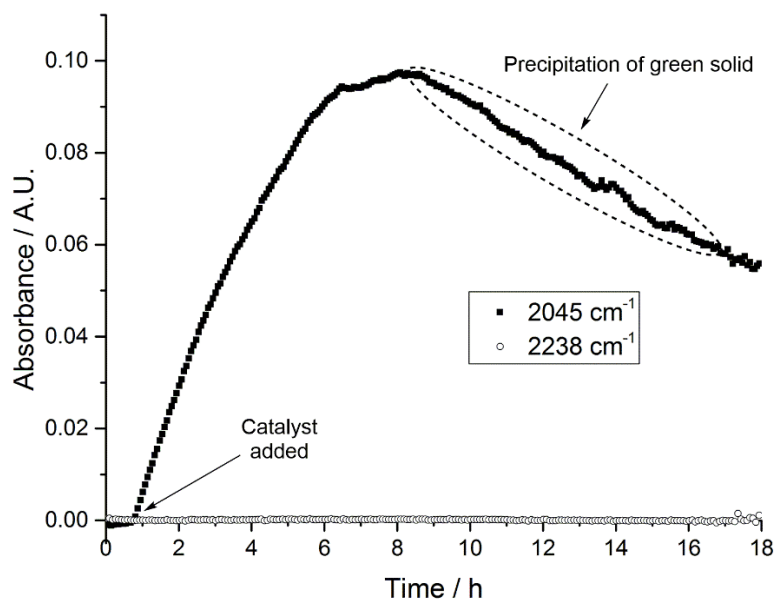
Supplementary Figure 28 | Left: 3D graph of *in situ* IR-spectra of the cyanation of **2**. Reaction conditions: **1-Pip** (0.1 mol%), $K_4[Fe(CN)_6] \cdot 3H_2O$ (0.22 eq.), Na_2CO_3 (1 eq.) and **2** (1 eq.) in DMAc at 120 °C. Right: raw absorbance data showing the time resolved formation of product (2238 cm^{-1}) and the intermediate cyanide species (2045 cm^{-1}).

Dissolution of KCN in DMAc at 120 °C also gave rise to a *single absorbance band* at 2045 cm^{-1} , indicating the presence of a different inorganic cyanide species. *Comparison of the in situ IR spectra in Supplementary Figure 27 with Supplementary Figure 29 shows that they are not the same. i.e.* The absorbance followed under normal reaction conditions (using hexacyanoferrate salts) at 2045 cm^{-1} is NOT free ^{-}CN .



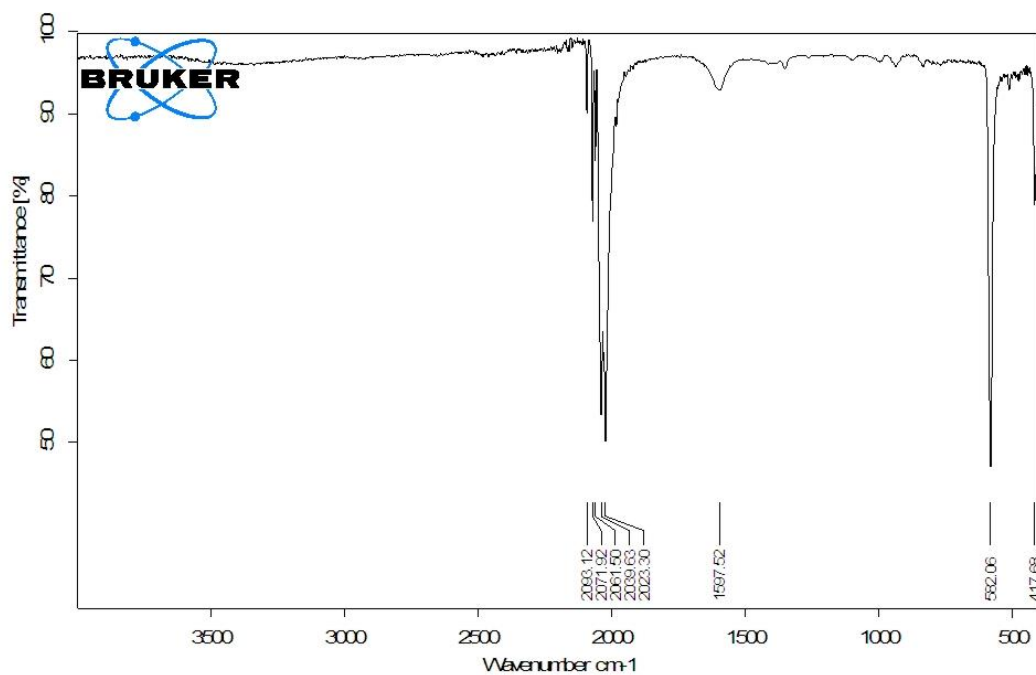
Supplementary Figure 29 | Left: 3D graph of *in situ* IR spectra of KCN in DMAc at 120 °C. Right: time resolved dissolution of KCN in DMAc, monitored at 2045 cm^{-1} . KCN added to the hot solvent at 1 hour.

When the reaction was performed under normal conditions, in the absence of Na_2CO_3 , no conversion to product **3** was observed, but the absorbance at 2045 cm^{-1} still steadily increased over 8 hours. After this point the absorbance decreased, coinciding with the precipitation of a green precipitate (Supplementary Figure 30).

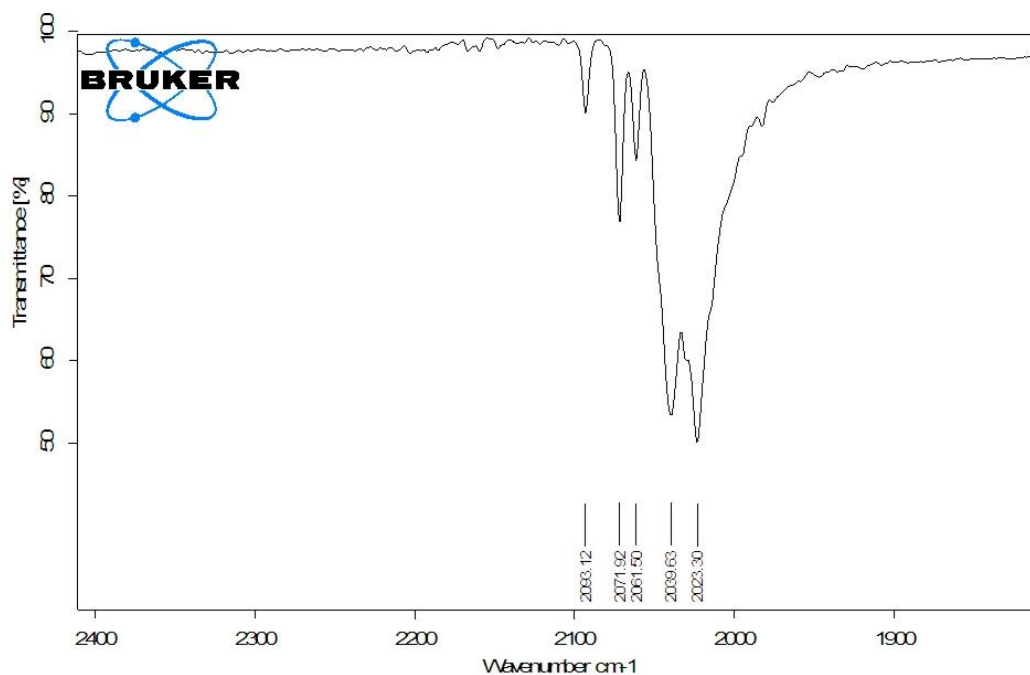


Supplementary Figure 30 | Raw absorbance data showing the time resolved formation of the intermediate cyanide species (2045 cm⁻¹) and lack of formation of product (2238 cm⁻¹) immediately after addition of **1-pip** in the absence of Na₂CO₃. Reaction conditions: **1-pip** (0.05 mol%), **2** (1 eq.), K₄[Fe(CN)₆] (0.22 eq.), DMAc, N₂, 120 °C.

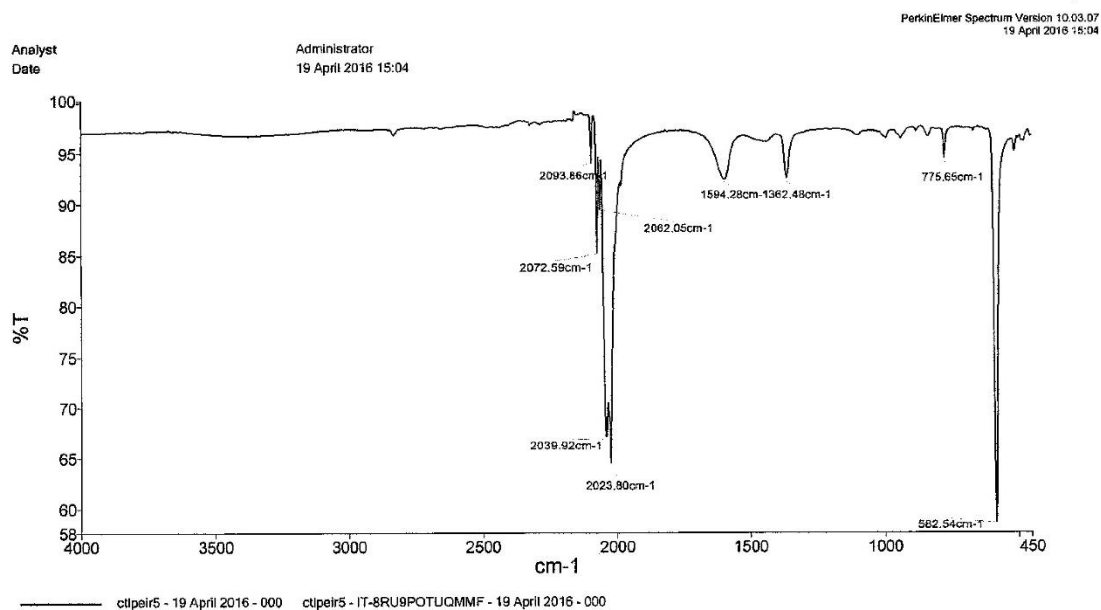
When the ATR-IR spectrum of this green precipitate (Supplementary Figure 31, Supplementary Figure 32) was compared with the ATR-IR spectrum of K₄(Fe(CN)₆, (Supplementary Figure 33, Supplementary Figure 34) it was evident that the species giving the absorbance at 2045 cm⁻¹, under working conditions, corresponded to solubilised [Fe(CN)₆].



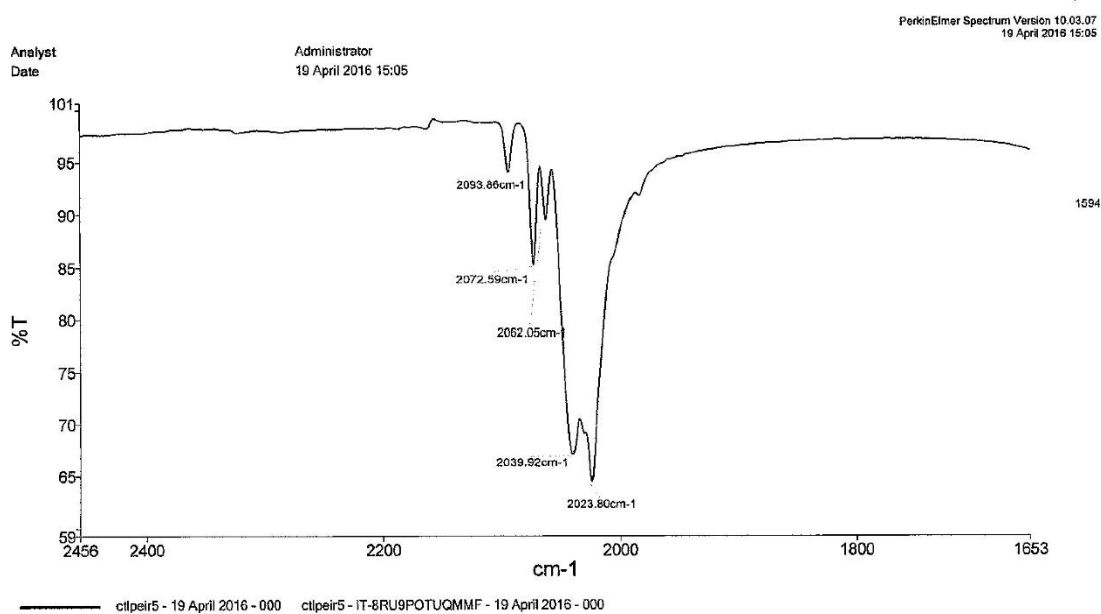
Supplementary Figure 31 | ATR-IR spectrum of green precipitate formed after 8 hours under reaction conditions but in the absence of Na_2CO_3 . Reaction conditions: **1-pip** (0.05 mol%), **2** (1 eq.), $\text{K}_4[\text{Fe}(\text{CN})_6]$ (0.22 eq.), DMAc, N_2 , 120 °C.



Supplementary Figure 32 | Expanded section of IR-region between $1800\text{-}2400\text{ cm}^{-1}$ of the ATR-IR spectrum shown in Supplementary Figure 31. Reaction conditions: **1-pip** (0.05 mol%), **2** (1 eq.), $\text{K}_4[\text{Fe}(\text{CN})_6]$ (0.22 eq.), DMAc, N_2 , 120 °C.

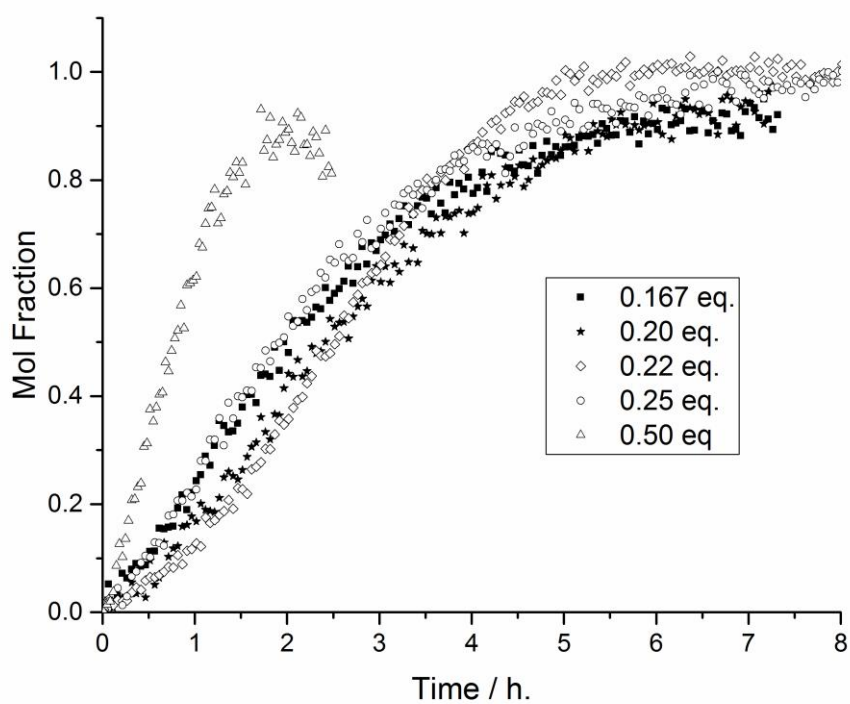


Supplementary Figure 33 | ATR-IR spectrum of $K_4[Fe(CN)_6]$.

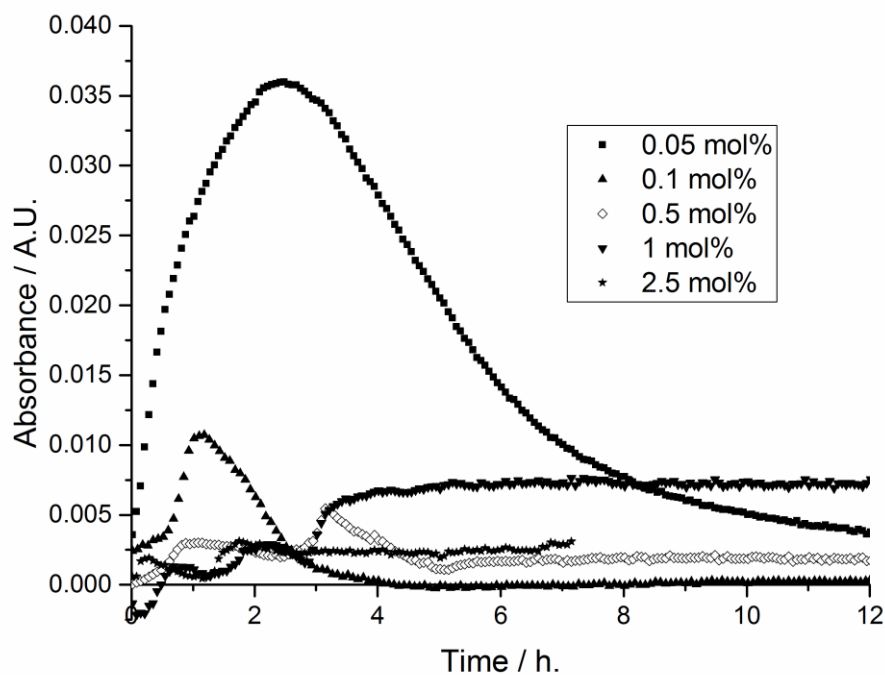


Supplementary Figure 34 | Expanded section of IR-region between $1800-2400\text{ cm}^{-1}$ of the ATR-IR spectrum shown in Supplementary Figure 33.

2.12. Varying $\text{K}_4[\text{Fe}(\text{CN})_6]\cdot 3\text{H}_2\text{O}$ equivalences



Supplementary Figure 35 | All $\text{K}_4[\text{Fe}(\text{CN})_6]\cdot 3\text{H}_2\text{O}$ equivalences kinetic investigations of **1-pip** under hydrous conditions. Reaction conditions: **1-pip** (0.5 mol%), $\text{K}_4[\text{Fe}(\text{CN})_6]\cdot 3\text{H}_2\text{O}$ (0.167–0.5 eq.), Na_2CO_3 (1 eq.), DMAc, N_2 , 120 °C.



Supplementary Figure 36 | All $\text{K}_4[\text{Fe}(\text{CN})_6]\cdot 3\text{H}_2\text{O}$ equivalences kinetic investigations of 1-Pip under hydrous conditions, following “[Fe(CN)₆]” absorbance (2045 cm^{-1}). Reaction conditions: 1-Pip (0.5 mol%), $\text{K}_4[\text{Fe}(\text{CN})_6]\cdot 3\text{H}_2\text{O}$ (0.167–0.5 eq.), Na_2CO_3 (1 eq.), DMAc, N_2 , $120\text{ }^\circ\text{C}$.

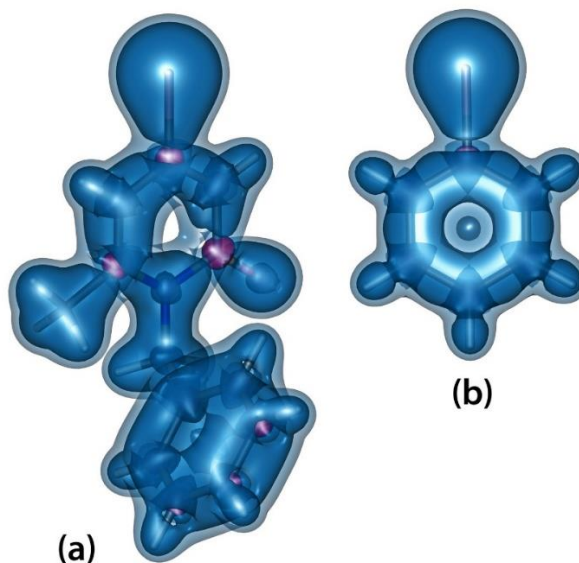
It is important to note here that the higher equivalence of $\text{K}_4[\text{Fe}(\text{CN})_6]\cdot 3\text{H}_2\text{O}$ results in an increase in initial reaction rate and concentration of “[Fe(CN)₆]”. This results in a spike in catalyst TOF, but after *ca.* 1.5 hours the [ArBr] has dropped to a point where it can no longer outcompete the rate of catalyst decomposition by formation of $\text{L}_y\text{Pd}^{\text{II}}(\text{CN})_x$, where $y+x=4$. This results in the reaction auto-quenching at 90% conversion, and a sudden spike in “[Fe(CN)₆]” concentration.

2.13. Relative aromaticities of N-methyl-4-bromo-6-methyl-2-pyridone, bromobenzene, pyridine and benzene

In order to obtain a theoretical estimate of the relative aromaticity of the 2-pyridone ring in N-benzyl-4-bromo-6-methyl-2-pyridone, **2**, we analysed the behavior of the off-nucleus isotropic magnetic shielding, $\sigma_{\text{iso}}(\mathbf{r})$, in the space surrounding the molecule following an approach similar to that used in reference.⁴

The gas-phase geometry of N-benzyl-4-bromo-6-methyl-2-pyridone was optimized at the B3LYP-GD3BJ/6-311++G(d,p) level, including Grimme's dispersion corrections with the Becke-Johnson damping, and the optimized geometry was confirmed as a local minimum through a diagonalization of the analytic nuclear Hessian. Off-nucleus isotropic magnetic shielding values were evaluated at the B3LYP-GIAO/6-311++G(d,p) level, using gauge-including atomic orbitals (GIAOs), for a regular $14 \times 9 \times 8 \text{ \AA}$ grid of points in the shape of a rectangular box encompassing the molecule, with a spacing of 0.1 \AA . For comparison purposes, an analogous sequence of calculations was performed for bromobenzene, for which it was sufficient to use a smaller $7 \times 9 \times 6 \text{ \AA}$ grid. All calculations reported in this paper were carried out using GAUSSIAN16.⁵

To aid visualization, all $\sigma_{\text{iso}}(\mathbf{r})$ values obtained for the N-benzyl-4-bromo-6-methyl-2-pyridone and bromobenzene were assembled in GAUSSIAN cube files. The spatial variations in isotropic magnetic shielding for N-benzyl-4-bromo-6-methyl-2-pyridone (**2**) and bromobenzene are illustrated in Supplementary Figure 37.



Supplementary Figure 37 | Isotropic magnetic shielding isosurfaces at $\sigma_{\text{iso}}(\mathbf{r}) = -16, 10$ (outermost), 16 ppm for (a) N-benzyl-4-bromo-6-methyl-2-pyridone (**2**) and (b) bromobenzene (positive isovalues in blue).

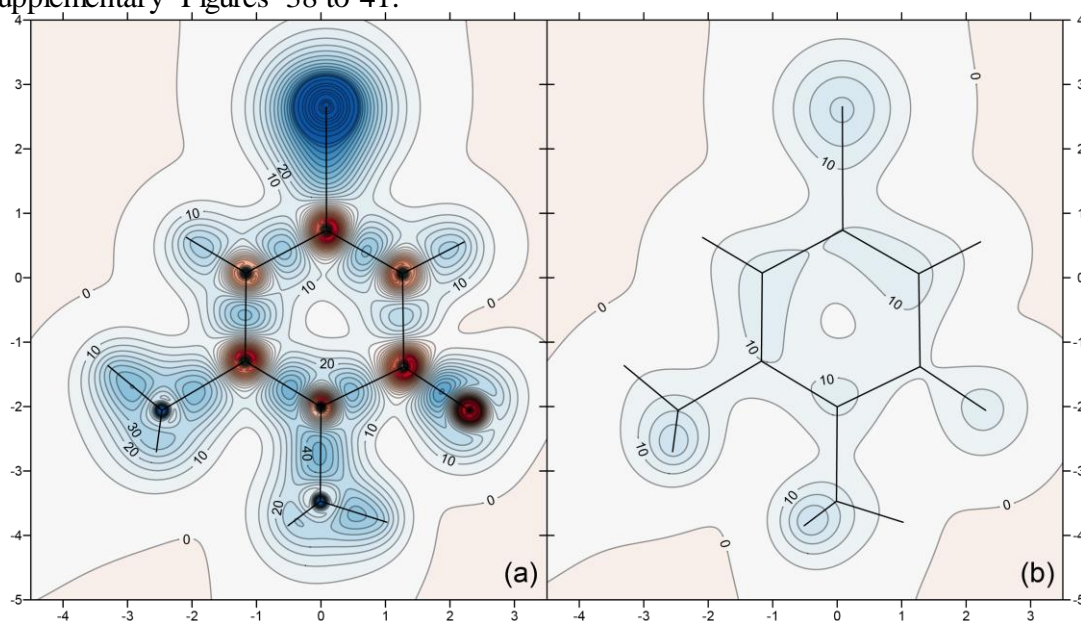
The benzene ring in the benzyl group [see Supplementary Figure 37(a)] is enclosed within a doughnut-shaped region of increased shielding, almost identical to that observed in an isolated benzene molecule.⁷

The rather uniform high shielding along the carbon-carbon bonds within this ring indicates strong bonding interactions and aromatic stability. The region of increased shielding along

the carbon framework in bromobenzene [see Supplementary Figure 37(b)] is less uniform and shows a disruption in the $\sigma_{\text{iso}}(\mathbf{r}) = 16$ ppm isosurface, along the C–Br bond, which can be associated with a minor decrease in aromaticity. Returning to N-benzyl-4-bromo-6-methyl-2-pyridone, but looking at the 2-pyridone ring, the $\sigma_{\text{iso}}(\mathbf{r}) = 16$ ppm isosurface shows not only the disruption along the C–Br bond present in bromobenzene, but also a more prominent disruption around the carbon involved in the C=O bond. However, there are no disruptions in the outermost $\sigma_{\text{iso}}(\mathbf{r}) = 10$ ppm isosurface which suggests that the 2-pyridone ring is aromatic, but less so than bromobenzene.

The small deviations from planarity of the 2-pyridone and benzene rings in N-benzyl-4-bromo-6-methyl-2-pyridone require aromaticity analysis utilizing isotropic magnetic shielding isosurfaces. However, a related smaller substituted 2-pyridone, N-methyl-4-bromo-6-methyl-2-pyridone, has a symmetry plane passing through the 2-pyridone ring. Therefore, its relative aromaticity can be assessed by comparing the isotropic magnetic shielding contour plots in this plane, and in a parallel plane 1 Å above it, to analogous contour plots for bromobenzene, pyridine and benzene.⁷⁻⁹

The gas-phase geometry of each of these four molecules was optimized at the B3LYP-GD3BJ/6-311++G(d,p) level, and the optimized geometry was confirmed as a local minimum through a diagonalization of the analytic nuclear Hessian. Off-nucleus isotropic magnetic shielding values were then evaluated at the B3LYP-GIAO/6-311++G(d,p) level, using gauge-including atomic orbitals (GIAOs), for regular rectangular grids of points of sufficient sizes, with a spacing of 0.05 Å. All calculations were carried out using GAUSSIAN16.⁵ The off-nucleus isotropic magnetic shieldings [$\sigma_{\text{iso}}(\mathbf{r})$] were used to construct the contour plots shown in Supplementary Figures 38 to 41.

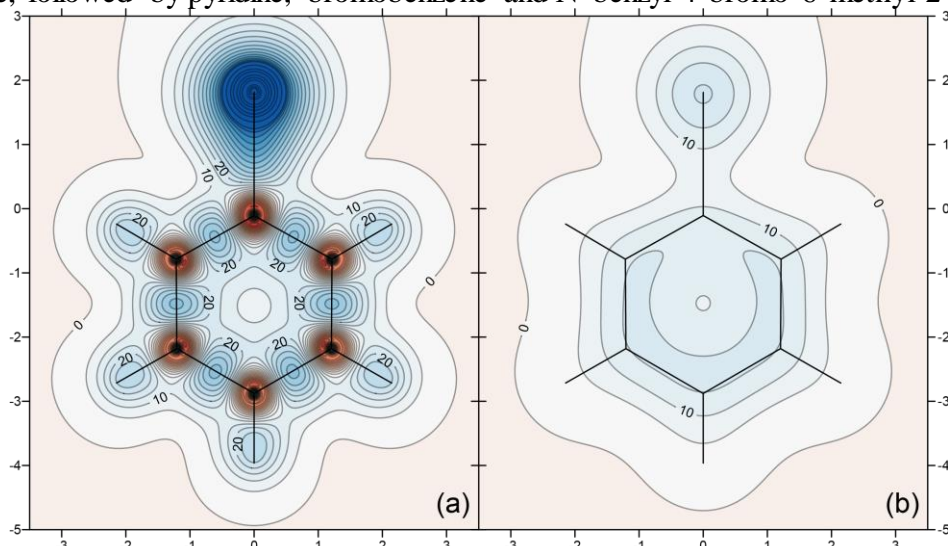


Supplementary Figure 38 | Contour plots of the isotropic magnetic shielding $\sigma_{\text{iso}}(\mathbf{r})$ (in ppm) for N-methyl-4-bromo-6-methyl-2-pyridone in (a) the symmetry plane passing through the 2-pyridone ring and (b) a plane 1 Å above it.

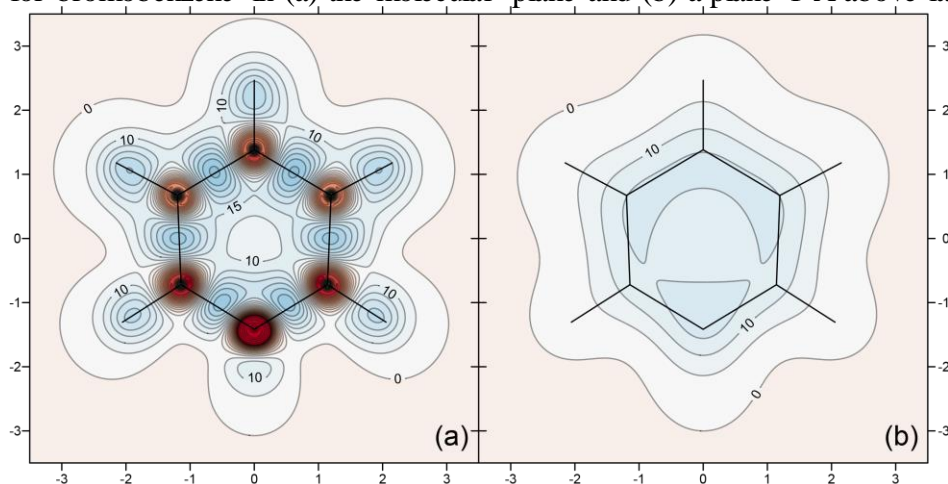
The $\sigma_{\text{iso}}(\mathbf{r})$ contour plots in the symmetry plane of N-methyl-4-bromo-6-methyl-2-pyridone and the molecular planes of the remaining three molecules suggest similar levels of σ bonding within the six-membered rings and sp^2 levels of hybridization for all atoms within a ring (indicated by the red deshielded “halos” surrounding these atoms). A detail worth pointing out

is that the C–C bond to the carbonyl carbon is weakened in comparison to the other bonds in the 2-pyridone ring.

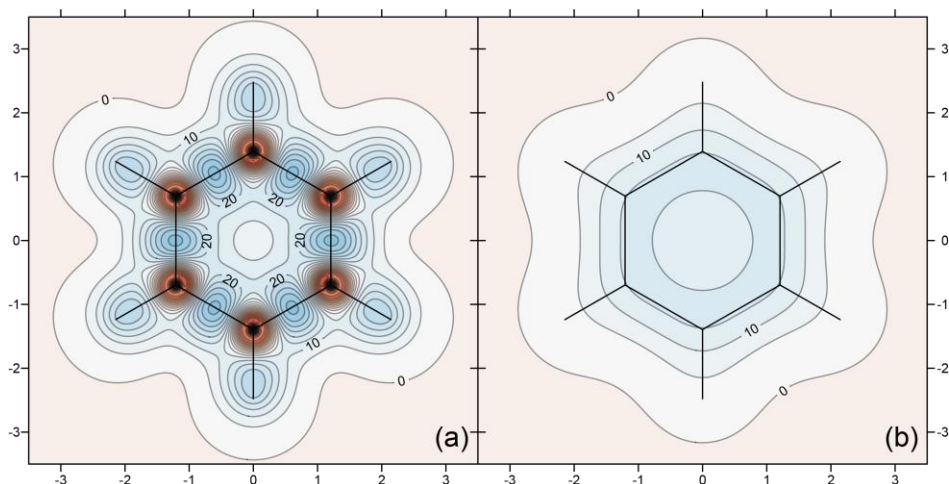
As a rule, aromaticity is considered to arise predominantly from the behaviour of the π electrons. The shielding due to π electrons is easier to analyse in the contour plots in planes 1 Å above the four rings, where the contributions of the σ electrons become negligible. Clearly, the increased isotropic shielding at a height of 1 Å above the ring is most uniformly delocalized in benzene, followed by pyridine, bromobenzene and N-benzyl-4-bromo-6-methyl-2-pyridone.



Supplementary Figure 39 | Contour plots of the isotropic magnetic shielding $\sigma_{\text{iso}}(\mathbf{r})$ (in ppm) for bromobenzene in (a) the molecular plane and (b) a plane 1 Å above it.



Supplementary Figure 40 | Contour plots of the isotropic magnetic shielding $\sigma_{\text{iso}}(\mathbf{r})$ (in ppm) for pyridine in (a) the molecular plane and (b) a plane 1 Å above it.



Supplementary Figure 41 | Contour plots of the isotropic magnetic shielding $\sigma_{\text{iso}}(\mathbf{r})$ (in ppm) for benzene in (a) the molecular plane and (b) a plane 1 Å above it.

Using the link between aromaticity and isotropic shielding delocalization, established in Refs. ^{8,9}, we can conclude that the four molecules are ordered, in terms of decreasing aromaticity, as benzene > pyridine > bromobenzene > N-benzyl-4-bromo-6-methyl-2-pyridone. It is also instructive to have a look at more traditional aromaticity criteria, the nucleus-independent chemical shifts (NICS), popular single-point aromaticity indices introduced by Schleyer and co-workers.¹⁰⁻¹²

For the purposes of this work, we define NICS(0) as the minimal $\sigma_{\text{iso}}(\mathbf{r})$ value in the plane of the ring and within its confines, taken with a negative sign, and NICS(1) as the minimal $\sigma_{\text{iso}}(\mathbf{r})$ value in the plane 1 Å above the ring and within the confines of the projection of the ring on that plane, again taken with a negative sign. The NICS(0) and NICS(1) values for N-methyl-4-bromo-6-methyl-2-pyridone, bromobenzene, pyridine and benzene are collected in Table 2. The NICS(1) values support the order of decreasing aromaticities, suggested by the $\sigma_{\text{iso}}(\mathbf{r})$ contour plots. However, NICS(0) makes the wrong prediction that bromobenzene is more aromatic than both benzene and pyridine which supports the view that aromaticity is a multidimensional property which cannot be fully described using a single number.¹³

Table 2: NICS(0) and NICS(1) values for N-methyl-4-bromo-6-methyl-2-pyridone, bromobenzene, pyridine and benzene (in ppm). For further details, see text.

Molecule	NICS(0)	NICS(1)
N-methyl-4-bromo-6-methyl-2-pyridone	-3.17	-4.46
bromobenzene	-8.53	-9.89
pyridine	-6.83	-10.17
benzene	-8.06	-10.23

GAUSSIAN archive entries from all geometry optimizations

N-benzyl-4-bromo-6-methyl-2-pyridone

```
1\1\GINC-QCHEMQ\FOpt\RB3LYP\6-311++G(d,p)\C13H12Br1N101\PBK\05-Jul-2017\0\#\ B3LYP/6-311++G(d,p) EmpiricalDispersion=GD3BJ # Int(Grid=SuperFine) Opt(VeryTight) Freq Test\2-Pyridone-full b3lyp-d3/6-311++G(d,p) Opt Freq\0,1\C,1.377657039,-1.3735770692,0.1376712422\C,1.343084305,0.0684836882,0.1649497556\C,0.1609917332,0.7303424858,0.0710168103\C,-1.0725950874,0.0534214481,-0.0678379805\C,-1.0708509439,-1.3147208137,-0.112111788\N,0.1110084792,-2.0092833709,-0.0218429779\H,2.2919372167,0.5717013956,0.2757278414\H,-2.0020905052,0.5962786021,-0.1392699598\C
```

,0.1277025748,-3.4806931539,-0.0399968534\H,1.1638376273,-3.7546856368,-0.2376944253\H,-0.4838925787,-3.8346338601,-0.8698915487\O,2.3968652381,-2.0463825141,0.2484744857\Br,0.1298161388,2.643217832,0.1281174863\C,-2.3495960299,-2.0840477938,-0.2647577447\H,-3.1899246227,-1.3923494062,-0.295730967\H,-2.3547916106,-2.6670699995,-1.1902564932\H,-2.4968413773,-2.7792310841,0.5641901583\C,-0.332505733,-4.1044951632,1.2593237983\C,-1.1266372451,-5.2522547138,1.2391379466\C,0.0517915713,-3.5659936034,2.4894464647\C,-1.5324805238,-5.8560465431,2.4276121311\H,-1.4343426464,-5.6746430276,0.2878293101\C,-0.3576294496,-4.1646718652,3.677652545\H,0.677696804,-2.6824234537,2.5176167241\C,-1.1508802064,-5.3108824141,3.6510829707\H,-2.150678655,-6.7458100759,2.3968157001\H,-0.0525038084,-3.7380229172,4.6261027305\H,-1.4688286039,-5.7749534124,4.5772776576\Version=ES64L-G16RevA.03\State=1-A\HF=-3206.9745794\RMSD=5.533e-09\RMSF=4.942e-08\Dipole=-1.7544173,-0.6418307,-0.0880337\Quadrupole=-5.1564979,1.9189967,3.2375012,5.581607,2.4792718,0.7592866\PG=C01 [X(C13H12Br1N101)]\@

N-methyl-4-bromo-6-methyl-2-pyridone

1\GINC-QCHEMQ\FOpt\RB3LYP\6-311++G(d,p)\C7H8Br1N101\PBK\03-Jul-2017\0\#\B3LYP/6-311++G(d,p) EmpiricalDispersion=GD3BJ # Int(Grid=SuperFine) Opt(VeryTight) Freq Test\2-Pyridone-4-Br-6-Me Cs b3lyp-d3/6-311++G(d,p) Opt Freq\0,1\C,-1.3119188528,-1.3548355144,0.\C,0.1288147426,-1.2592826643,0.\C,0.7415939072,-0.0477744611,0.\C,0.0134141734,1.1646712262,0.\C,-1.3542378415,1.1064566546,0.\N,-2.0009910815,-0.104181544,0.\H,0.6720816819,-2.1924016407,0.\H,0.5163749153,2.1190101355,0.\C,-3.4653777326,-0.1688777223,0.\H,-3.7377285491,-1.2201578403,0.\H,-3.8718702249,0.3129002787,0.890578168\H,-3.8718702249,0.3129002787,-0.890578168\O,-1.9367402472,-2.4085644568,0.\Br,2.6529660204,0.0577645662,0.\C,-2.1838964677,2.3565614975,0.\H,-1.5333821453,3.229703901,0.\H,-2.829130246,2.4087040023,-0.881170193\H,-2.829130246,2.4087040023,0.881170193\Version=ES64L-G16RevA.03\State=1-A'\HF=-2975.8399526\RMSD=6.169e-09\RMSF=2.756e-07\Dipole=-0.7365718,1.8098508,0.\Quadrupole=4.5471291,-3.5913453,-0.9557838,-8.1038775,0.,0.\PG=CS [SG(C7H4Br1N101),X(H4)]\@

Bromobenzene

1\GINC-QCHEMQ\FOpt\RB3LYP\6-311++G(d,p)\C6H5Br1\PBK\05-Jul-2017\0\#\B3LYP/6-311++G(d,p) EmpiricalDispersion=GD3BJ # Int(Grid=SuperFine) Opt(VeryTight) Freq Test\C6H5Br C2v b3lyp-d3/6-311++G(d,p) Opt Freq\0,1\C,0.,0.,-0.1145569695\C,0.,1.2139316795,-0.7937882454\C,0.,-1.2139316795,-0.7937882454\C,0.,1.2052920308,-2.1875666858\H,0.,2.1466992398,-0.2456317745\Br,0.,0.,1.803433888\C,0.,-1.2052920308,-2.1875666858\H,0.,-2.1466992398,-0.2456317745\C,0.,0.,-2.8864635527\H,0.,2.1468388338,-2.7241501482\H,0.,-2.1468388338,-2.7241501482\H,0.,0.,-3.9697607281\Version=ES64L-G16RevA.03\State=1-A1\HF=-2805.8775301\RMSD=3.052e-09\RMSF=2.227e-07\Dipole=0.,0.,-0.7317787\Quadrupole=-4.3625084,2.5161137,1.8463947,0.,0.,0.\PG=C02V [C2(H1C1C1Br1),SGV(C4H4)]\@

Pyridine

1\GINC-QCHEMA\FOpt\RB3LYP\6-311++G(d,p)\C5H5N1\PBK\04-Jul-2017\0\#\B3LYP/6-311++G(d,p) EmpiricalDispersion=GD3BJ # Int(Grid=SuperFine) Opt(VeryTight) Freq\pyridine b3lyp-d3/6-311++G(d,p) Opt Freq\0,1\C,0.,1.1414948303,-0.7195673095\C,0.,1.1962389444,0.6730868976\C,0.,0.,1.3842242382\C,0.,-1.1962389444,0.6730868976\C,0.,-1.1414948303,-0.7195673095\N,0.,0.,-1.4145880507\H,0.,0.,2.468174191\H,0.,2.0565342365,-1.3046527662\H,0.,2.1529171795,1.1813715039\H,0.,-2.1529171795,1.1813715039\H,0.,-2.0565342365,-1.3046527662\Version=ES64L-G16RevA.03\State=1-A1\HF=-248.3684155\RMSD=4.367e-09\RMSF=5.534e-07\Dipole=0.,0.,0.9303346\Quadrupole=-2.4476196,3.9494304,-1.5018108,0.,0.,0.\PG=C02V [C2(H1C1N1

),SGV(C4H4)]\@

Benzene

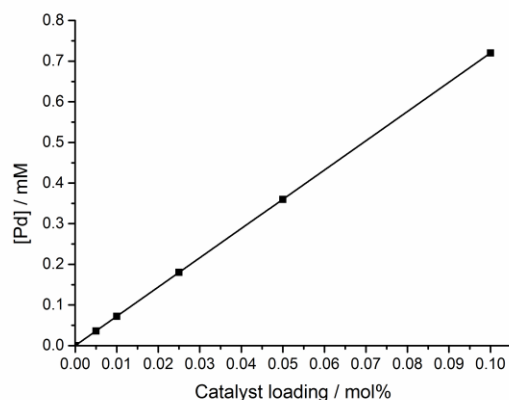
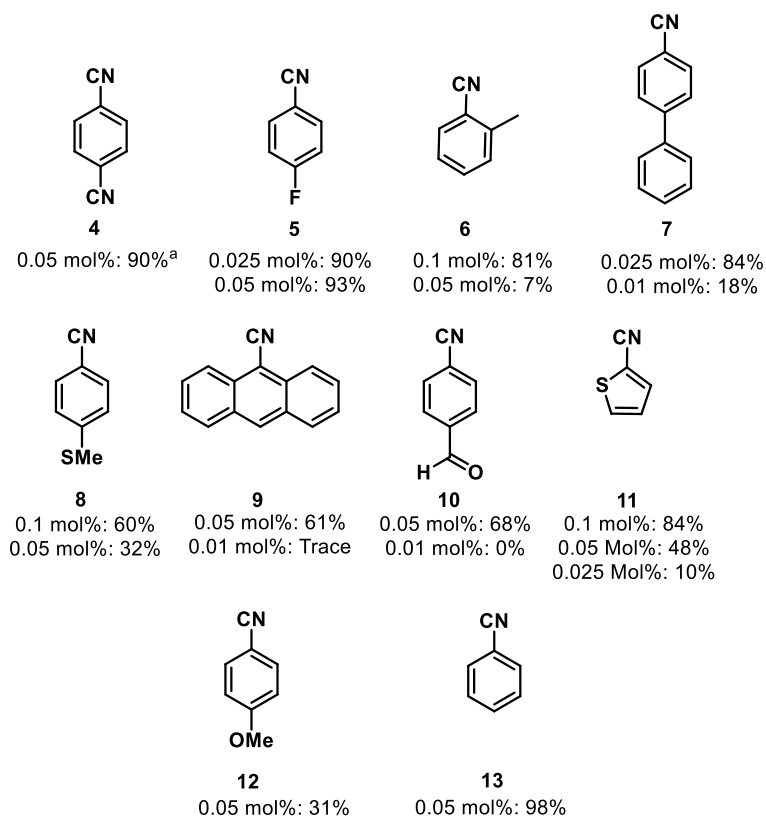
```
1\1\GINC-QCHEMA\FOpt\RB3LYP\6-311++G(d,p)\C6H6\PBK\04-Jul-2017\0\#\# B3
LYP/6-311++G(d,p) EmpiricalDispersion=GD3BJ # Int(Grid=SuperFine) Opt(
VeryTight) Freq\c6h6 b3lyp-d3/6-311++G(d,p) Opt Freq\0,1\C,0.,0.,-0.
002298878\H,0.,0.,1.0817209514\C,1.2073269871,0.,-0.699349439\H,2.1461
156976,0.,-0.1573395243\C,1.2073269871,0.,-2.093450561\H,2.1461156976,
0.,-2.6354604757\C,0.,0.,-2.790501122\H,0.,0.,-3.8745209514\C,-1.20732
69871,0.,-2.093450561\H,-2.1461156976,0.,-2.6354604757\C,-1.2073269871
,0.,-0.699349439\H,-2.1461156976,0.,-0.1573395243\Version=ES64L-G16Re
va.03\State=1-A1G\HF=-232.3302226\RMSD=7.521e-10\RMSF=1.396e-08\Dipole
=0.,0.,0.\Quadrupole=2.0251482,-4.0502964,2.0251482,0.,0.,0.\PG=D06H [
3C2'(H1C1.C1H1)]\@
```

Shielding GAUSSIAN cube files

The GAUSSIAN cube files showing the spatial variations of the isotropic magnetic shielding in N-benzyl-4-bromo-6-methyl-2-pyridone and bromobenzene are included in a separate zip archive, shielding-cube-files.zip. This archive contains two GAUSSIAN cube files, N-benzyl-4-bromo-6-methyl-2-pyridone-shielding.cube and c6h5br-shielding.cube.

2.14. Substrate scope

The optimized reaction system was tested on a range of (hetero)aryl bromides, the successfully cyanated substrates are outlined below (Supplementary Figure 42).



Supplementary Figure 42 | Reaction conditions: ArBr (1 eq., 1.4 mmol), 1-pip (0.01-0.1 mol%) $K_4[Fe(CN)_6]$ (0.22 eq.), Na_2CO_3 (1 eq.), DMAc (2 ml), N_2 , 140 °C, 16 h. ^a Using $K_4[Fe(CN)_6]$ (0.44 eq. with respect to 1,4-dibromobenzene). Graph shows the catalyst loading-Pd concentration (mM) relationship under all substrate screen conditions.

A range of catalyst loadings and concentrations were utilised to optimise reaction yields. Electron poor coupling partners provided the best results, with 4-fluorobromobenzene achieving 90% yield in the formation of **5** with a catalyst loading of only 0.025 mol% (185 μ M). Likewise, **4** was provided in 90% yield with a catalyst loading of 0.05 mol% (370 μ M) in the presence of 0.44 eq. of $K_4[Fe(CN)_6]$; no monocyanoated product was isolated from the

reaction mixture. Both **9** and **10** were isolated in good yields in the presence of 0.05 mol% **1-pip**, however further reducing the catalyst loadings to 0.01 mol% resulted in no catalyst turnover. Interestingly, increased steric bulk around the position of cross-coupling had a substantial detrimental effect on product yields. To achieve acceptable yields Pd precatalyst loadings and concentrations had to be increased to 0.1 mol% ($[Pd] = 720 \mu M$) when attempting to cyanate 2-methylbromobenzene to give **6**. Sulphur was tolerated in both **8** and **11** when catalyst loadings were increased to 0.1 mol%, but in the presence of the strongly electron donating 4-methoxy group, a lower yield was observed at 0.05 mol% catalyst loading for **12**.

3. Experimental

General experimental procedure for the synthesis of *trans*-Pd(OAc)₂(HNR₂)₂ complexes¹⁴:

Representative procedure for the synthesis of *bis-trans*-[piperidiny- κ -N]palladium(II) diacetate (**1-pip**): A flame dried Schlenk tube was charged with Pd₃(OAc)₆ (100 mg, 0.148 mmol, 1 eq.) and backfilled with N₂ (3 ×). To the Pd₃(OAc)₆, dry THF (5 mL) was added and the mixture was stirred until complete dissolution (*ca.* 5 minutes) to give a reddish-brown solution. To the Pd₃(OAc)₆ solution, piperidine (freshly distilled under N₂, 88 μ L, 0.89 mmol, 6 eq.) was added dropwise *via* a septum resulting in a color change from reddish-brown through dark red (indicating the formation of the Pd₂(OAc)₄(HNC₅H₁₁)₂ dimer complex at the halfway point of amine addition) to dark yellow after complete addition. The reaction mixture was stirred at room temperature for a further 5 minutes. The solvent was removed *in vacuo* directly to provide a light green solid (175.0 mg, 90%). This can be recrystallized from DCM/hexane at *ca.* -18 °C, yielding a yellow crystalline solid. MP 165.0 – 168.4 °C (dec.) ¹H NMR (400 MHz, CDCl₃) δ 5.54 (bt, $J = 10.9$ Hz, 2H), 3.14 (d, $J = 12.8$ Hz, 4H), 2.56 (qd, $J = 2.8, 12.8$ Hz, 4H), 1.95 (s, 6H), 1.75- 1.56(m, 6H), 1.51 – 1.30 (m, 6H); ¹³C NMR (101 MHz, CDCl₃) δ 181.0, 49.5, 26.5, 24.0, 23.0; LIFDI MS, m/z 394.12 [M⁺]; ν_{max}/cm^{-1} (ATR): 3486, 3420, 3190, 2941, 2861, 1675, 1573, 1448, 1392, 1368, 1332, 1319, 1194, 1112, 1022, 1012, 944, 880, 813, 695, 654, 627, 601, 466.

Bis-trans-[Azepinyl- κ -N]Palladium(II) diacetate (**1-aze**):

The complex was prepared according to the general procedure for the synthesis of *trans*-Pd(OAc)₂(HNR₂)₂ complexes. Yield: 142.5 mg, 75%; MP 110.1 – 114.0 (dec.); ¹H NMR (400 MHz, CD₂Cl₂) δ 5.96 (bt, $J = 8.6$ Hz, 2H), 3.24 (ddt, $J = 13.6, 6.7, 3.2$ Hz, 4H), 2.6 (dddd, $J = 13.6, 9.9, 8.6, 3.2$ Hz, 4H), 1.93 (s, 6H), 1.73 – 1.61 (m, 4H), 1.61 – 1.41 (m, 12H); ¹³C NMR (101 MHz, CDCl₃) δ 180.6, 50.8, 28.1, 26.6, 24.0; LIFDI MS, m/z 422.12 [M⁺]; ν_{max}/cm^{-1} (ATR) 3187, 2925, 1592, 1463, 1357, 1308, 1261, 1014, 846, 801, 691. Crystal data for ijsf1402 (**1-aze**): C₁₆H₃₀N₂O₈Pd₂, $M = 1.055$, $a = 6.0767(4)$, $b = 7.1046(4)$, $c = 10.4577(5)$, $\alpha = 89.399(4)^\circ$, $\beta = 84.578(5)^\circ$, $\gamma = 86.939(5)^\circ$, $V = 448.82(4) \text{ \AA}^3$, $T = 110.10(14) \text{ K}$, space group P-1, $Z = 1$, 8212 reflections collected, 2927 [R(int) = 0.0323, R_{sigma} = 0.0372] independent reflections. The final R indexes [$I \geq 2\sigma(I)$] were R₁ = 0.0251, wR₂ = 0.0640. The final R indexes all data were R₁ = 0.0255, wR₂ = 0.0645. The goodness of fit on F² was 1.081.

Bis-trans-[pyrrolidinyl- κ -N]Palladium(II) diacetate (**1-pyr**):

The complex was prepared according to the general procedure for the synthesis of *trans*-Pd(OAc)₂(HNR₂)₂ complexes. Yield: 81.3 mg, 50%; MP 140.2 – 142.3 (decomp.); ¹H NMR (400 MHz, CDCl₃) δ 5.98 (s, 2H), 3.02 – 2.92 (m, 4H), 4.74 – 2.58 (m, 4H), 1.86 (s, 6H), 1.78 – 1.65 (m, 4H), 1.80-1.53 (m, 4H); ¹³C NMR (101 MHz, CDCl₃) δ 180.6, 48.5, 24.1, 23.9; LIFDI MS, m/z 368 [M⁺]; ν_{max}/cm^{-1} (ATR) 3469, 3393, 3182, 2964, 1573, 1371, 1315,

1260, 1014, 907, 800, 694, 620. Crystal data for ijsfl464 (**1-pyr**): $C_{12}H_{28}N_2O_8Pd_1$, $M = 1.592$, $a = 17.1405(6)$, $b = 6.10222(17)$, $c = 16.0694(5)$, $\alpha = 90.00^\circ$, $\beta = 90.140(3)^\circ$, $\gamma = 90.00^\circ$, $V = 1680.78(9) \text{ \AA}^3$, $T = 110.05(10) \text{ K}$, space group $C_{12}/C1$, $Z = 4$, 4628 reflections collected, 1496 [$R_{\text{int}} = 0.0295$, $R_{\text{sigma}} = 0.0286$] independent reflections. The final R indexes [$I \geq 2\sigma(I)$] $R_1 = 0.0290$, $wR_2 = 0.0728$. The final R indexes all data were $R_1 = 0.0335$, $wR_2 = 0.0759$. The goodness of fit on F^2 was 1.086.

***Bis-trans*-[2,6-*cis* dimethylpiperidinyl- κ -*N*]Palladium(II) diacetate (**1-dmp**):**

The complex was prepared according to the general procedure for the synthesis of *trans*-Pd(OAc)₂(HNR₂)₂ complexes. Yield: 200.7 mg, 72%; MP 157-158 °C (decomp.); ¹H NMR (400 MHz, CD₆D₆) δ 8.06 (bs, , 2H), 2.75-2.60 (m, 4 H), 2.14 (d, $J = 6.5 \text{ Hz}$, 6H), 2.09 (d, $J = 6.4 \text{ Hz}$, 6H), 2.00 (s, 6H), 1.96 – 1.92 (m, 8H), 1.93 – 1.70 (m, 4 H); ¹³C NMR (101 MHz, CDCl₃) δ 181.0, 56.7, 33.8, 29.3, 24.4, 24.3, 23.2, 23.1, 22.7; LIFDI MS, m/z 450 [M⁺]; $\nu_{\text{max}}/\text{cm}^{-1}$ (ATR) 3059, 2963, 2927, 2863, 1585, 1449, 1370, 1320, 1260, 1171, 1104, 1015, 652, 926, 801, 687, 614, 544. Crystal data ijsfl470 (**1-dmp**): $C_{18}H_{36}N_2O_4Pd_1$, $M = 0.921$, $a = 7.49848(14)$, $b = 9.61025(19)$, $c = 14.3500(3)$, $\alpha = 90.00^\circ$, $\beta = 92.4862(18)^\circ$, $\gamma = 90.00^\circ$, $V = 1033.12(3) \text{ \AA}^3$, $T = 110.05(10) \text{ K}$, space group $P2_1/C$, $Z = 2$, 6182 reflections collected, 1496 [$R_{\text{int}} = 0.0295$, $R_{\text{sigma}} = 0.0286$] independent reflections. The final R indexes [$I \geq 2\sigma(I)$] $R_1 = 0.0342$, $wR_2 = 0.0672$. The final R indexes all data were $R_1 = 0.0460$, $wR_2 = 0.0722$. The goodness of fit on F^2 was 1.224.

***Bis-trans*-[2,2,6,6-tetramethylpiperidinyl- κ -*N*]Palladium(II) diacetate (**1-tmp**) ¹⁵:**

The complex prepared according to the general procedure for the synthesis of *trans*-Pd(OAc)₂(HNR₂)₂ complexes. Yield: 132 mg, 59%; MP 157-158 °C (decomp.); ¹H NMR (400 MHz, CDCl₃) δ 8.06 (bs, 2H), 1.90 (s, 12H), 1.84 (s, 6 H), 1.46 (s, 12H), 1.48-1.42 (m, 12H); ¹³C NMR (101 MHz, CDCl₃) δ 180.5, 58.2, 38.3, 33.9, 26.4, 24.4, 18.0; LIFDI MS, m/z 450 [M⁺]; $\nu_{\text{max}}/\text{cm}^{-1}$ (ATR) 3059, 2963, 2927, 2863, 1585, 1449, 1370, 1320, 1260, 1171, 1104, 1015, 652, 926, 801, 687, 614, 544.

***N*-Benzyl-4-Bromo-6-methylpyridin-2-one (**2**):**

A large three necked round bottomed flask equipped with a thermometer, mechanical stirrer and condenser was purged with a flow of N₂ for 20 minutes before addition of 4-hydroxy-6-methyl-*N*-benzyl-pyridin-2(*1H*)-one (5 g, 2.52 mmol, 1 eq.) followed by freshly weighed out P₂O₅ (7.84 g, 5.52 mmol, 2.38 eq.), then purged for a further 5 minutes. Dry toluene was added (200 mL) and the mixture was heated to 80 °C with mechanical stirring for 1 hour, forming a yellow suspension. Bu₄NBr (8.67g, 2.62 mmol, 1.16 eq.) was added and the reaction subsequently heated to reflux (110 °C) with vigorous mechanical stirring for 2 hours. The reaction mixture was allowed to cool to room temperature and the upper toluene layer was collected. The lower (resinous) layer was extracted with toluene (100 ml), then the combined organic layers were washed with saturated NaHCO₃ (aq.) solution (70 mL), saturated brine (50 mL), dried over anhydrous MgSO₄ and then concentrated *in vacuo* to afford the crude product. Saturated NaHCO₃ (aq.) (100 ml) was slowly added to the lower resinous layer (vigorous evolution of CO₂) and stirred until all solid material was dissolved (*ca.* 1 hr.). The resulting solution was then extracted with toluene (50 mL \times 2), washed with saturated brine solution (50 mL), dried over MgSO₄, filtered then the solvent removed *in vacuo* to provide additional crude product. Flash chromatography (SiO₂, 40% EtOAc/Petrol) afforded the title compound as a white crystalline solid (2.4535 g, 38%). MP 98.0 – 100.5 °C.; ¹H NMR (400 MHz, CDCl₃) δ 7.35 – 7.28 (m, 2H), 7.28 – 7.23 (m, 1H), 7.14 (d, $J = 7.5 \text{ Hz}$, 2H), 6.80 (d, $J = 2.0 \text{ Hz}$, 1H), 6.22 (d, $J = 2.0 \text{ Hz}$, 1H), 5.29 (s, 2H), 2.25 (s, 3H); ¹³C (101 MHz, CDCl₃) δ 160.5, 147.0, 135.9, 135.6, 129.0, 127.7, 126.5, 120.1, 111.2, 47.3,

20.5; Elemental analysis: (calc) C, 56.14; H, 4.35; N, 5.04; Other; 34.48 (obs) C, 56.22; H, 4.41; N, 5.01; Other: 34.48; m/z (ESI⁺) 278.0175 [(M+H)⁺, Br⁷⁹], 299.9996 [(M+Na)⁺, Br⁷⁹]; $\nu_{\max}/\text{cm}^{-1}$ (ATR) 3055, 1647, 1572, 1541, 1409, 1345, 1180, 888, 845, 804, 739, 725, 696, 594, 524, 429; R_f 0.4 (40% EtOAc/Petrol).

General experimental procedure for the cyanation of aryl halides:

Representative procedure using **1-pip**: To a flame dried 30 mL Schlenk tube charged with a stirrer bar was added aryl bromide (1.4 mmol), freshly ground $\text{K}_4[\text{Fe}(\text{CN})_6]$ (130 mg, 3.08 mmol, 0.22 eq.), freshly ground Na_2CO_3 (148 mg, 1.4 mmol, 1 eq.). The vessel was then backfilled with N_2 with stirring (3 \times). To a separate 10 mL flame dried Schlenk tube charged with a stirrer bar was added **1-pip** (10 mg, 2.53×10^{-5} mol) and the vessel backfilled with N_2 with stirring (3 \times). Dry DMAc (2 mL) was added *via* a septum to the reaction vessel containing the aryl bromide, then this reaction mixture was added to an oil bath preheated to 140 °C. Concomitantly, dry DMAc (1 mL) was added to the Schlenk tube containing **1-pip** and was stirred until complete dissolution of the precatalyst was observed to give a precatalyst solution with a concentration of 25.3 mmol dm^{-3} . Immediately after complete dissolution of **1-pip**, the required amount of precatalyst solution was added using an appropriate microsyringe through a septum to the preheated reaction mixture. The resulting reaction mixture was stirred vigorously under a static N_2 atmosphere at 140 °C for 16 h. After reaction completion, the mixture was then allowed to cool to room temperature and purified directly by silica gel column chromatography with an appropriate solvent system.

N-benzyl-4-cyano-6-methylpyridin-2-one (**3**):

The compound was prepared per the general procedure for the cyanation of aryl halides. Flash chromatography (SiO_2 , 50% EtOAc/Petrol) afforded the product as a white crystalline solid (0.307 g, 98%). MP 116.9 – 120 °C; ^1H NMR (400 MHz, CDCl_3) δ 7.34 – 7.27 (m, 3H), 7.12 (ddt, $J = 7.1, 1.3, 0.7$ Hz, 2H), 6.85 (dq, $J = 1.8, 0.8$ Hz, 1H), 6.13 (dq, $J = 1.8, 0.8$ Hz, 1H), 5.31 (s, 2H), 2.31 (dd, $J = 0.8, 0.8$ Hz, 3H); ^{13}C NMR (101 MHz, CDCl_3) δ 162.1, 149.4, 135.1, 129.1, 127.9, 126.6, 123.4, 123.3, 116.1, 106.1, 47.8, 20.9; Elemental analysis: (calc) C, 74.98; H, 5.39; N, 12.49; Other; 7.13 (obs) C, 75.01; H, 5.45; N, 12.36 Other: 7.18; m/z (ESI⁺) 225.1023 [(M+H)⁺], 247.0841 [(M+Na)⁺]; $\nu_{\max}/\text{cm}^{-1}$ (ATR) 3089, 3066, 3031, 2967, 2237, 1666, 1575, 1531, 1412, 1345, 1172, 1099, 1031, 966, 924, 865, 819, 723, 692, 657, 639, 600, 574, 478, 444; R_f 0.3 (40% EtOAc/Petrol). Crystal data: Crystal data ijsf1330 (**3**): $\text{C}_{13.97}\text{H}_{12}\text{Br}_{0.03}\text{N}_{1.97}\text{O}$, $M = 0.183$, $a = 11.0909(2)$, $b = 13.3680(4)$, $c = 7.95097(18)$, $\alpha = 90.00^\circ$, $\beta = 92.498(2)^\circ$, $\gamma = 90.00^\circ$, $V = 1177.72(5) \text{ \AA}^3$, $T = 110.05(10) \text{ K}$, space group $\text{P2}_1/\text{c}$, $Z = 4$, 8699 reflections collected, 3781 [$R(\text{int}) = 0.0465$] independent reflections. The final R indexes [$I \geq 2\sigma(I)$] were $R_1 = 0.0548$, $wR_2 = 0.1181$. The final R indexes all data were $R_1 = 0.0771$, $wR_2 = 0.1318$. The goodness of fit on F^2 was 1.083.

1,4-Dicyanobenzene (**4**)¹⁶:

The compound prepared per the general procedure for the cyanation of aryl halides. Flash chromatography (SiO_2 , 20% EtOAc/Petrol) afforded the product as a white crystalline solid (0.155 g, 90%). ^1H NMR (CDCl_3 , 400 MHz): δ 7.80 (s, 4H); ^{13}C NMR (101 MHz, CDCl_3): 132.9, 117.2, 116.9.

4-Fluorobenzonitrile (**5**)¹⁷:

The compound was prepared per the general procedure for the cyanation of aryl halides. Flash chromatography (SiO_2 , 20% EtOAc/Petrol) afforded the product as a volatile, white crystalline solid (0.153 g, 93%). ^1H NMR (CDCl_3 , 400 MHz): δ 7.70 – 7.64 (m, 2H), 7.20-

7.13 (m, 1H); ^{13}C NMR (101 MHz, CDCl_3): δ 165.0 (d, $J = 256$ Hz), 134.6 (d, $J = 9$ Hz), 118.0, 116.8 (d, $J = 24$ Hz) 108.5 (d, $J = 4$ Hz); ^{19}F NMR (CDCl_3 , 376 MHz) δ 102.3 (m, 1F).

2-Methylbenzonitrile (6)¹⁷:

The compound was prepared per the general procedure for the cyanation of aryl halides. Flash chromatography (SiO_2 , 10-20% EtOAc/Petrol) afforded the product as a white crystalline solid (0.133 g, 81%). ^1H NMR (CDCl_3 , 400 MHz): δ 7.60 (dd, $J = 7.7$, 1.4 Hz, 1H), 7.48 (ddd, $J = 7.7$, 7.7, 1.4 Hz, 1H), 7.32 (d, $J = 7.8$ Hz, 1H), 7.28 (d, $J = 7.8$ Hz, 1H), 2.55 (s, 3H); ^{13}C NMR (101 MHz, CDCl_3): 142.0, 132.8, 132.7, 130.4, 126.4, 118.3, 112.9, 20.6.

4-Phenylbenzonitrile (7)¹⁷:

The compound was prepared per the general procedure for the cyanation of aryl halides. Flash chromatography (SiO_2 , 100% Petrol) afforded the product as a white crystalline solid (0.207 g, 84%). ^1H NMR (CDCl_3 , 400 MHz): δ 7.73 (d, $J = 8.4$ Hz, 2H), 7.69 (d, $J = 8.4$ Hz, 2H), 7.6 (d, $J = 7.1$, 2H), 7.49 (ddd, $J = 7.1$, 7.1 Hz, 2H), 7.43 (dd, $J = 7.1$, 7.1 Hz, 1H); ^{13}C NMR (101 MHz, CDCl_3): δ 145.8, 139.3, 132.7, 129.2, 128.8, 127.9, 127.4, 119.1, 111.0.

4-(Methylthio)benzonitrile (8)¹⁷:

The compound was prepared per the general procedure for the cyanation of aryl halides. Flash chromatography (SiO_2 , 10-30% EtOAc/Petrol) afforded the product as a white crystalline solid (0.125 g, 60%). ^1H NMR (CDCl_3 , 400 MHz): δ 7.52 (d, $J = 8.7$ Hz, 2H), 7.25 (d, $J = 8.7$ Hz, 2H), 2.50 (s, 3H); ^{13}C NMR (101 MHz, CDCl_3): 146.2, 132.2, 125.5, 119.1, 107.7, 14.8.

9-Cyanoanthracene (9)¹⁷:

The compound was prepared per the general procedure for the cyanation of aryl halides. Flash chromatography (SiO_2 , 10-1% Et₂O/Petrol) afforded the product as a bright yellow crystalline solid (0.174 g, 61%). ^1H NMR (CDCl_3 , 400 MHz): δ 8.66 (s, 1H), 8.41 (ddd, $J = 8.7$, 1.8, 1.0 Hz, 2H), 8.07 (dd, $J = 8.5$, 1.0 Hz, 2H), 7.71 (ddd, $J = 8.7$, 6.7, 1.2 Hz, 2H), 7.58 (ddd, $J = 8.5$, 6.7, 1.2 Hz, 2H); ^{13}C NMR (101 MHz, CDCl_3): 133.4, 132.9, 130.7, 130.8, 129.1, 126.5, 125.4, 117.4, 105.6.

4-Formylbenzonitrile (10)¹⁸:

The compound was prepared per the general procedure for the cyanation of aryl halides. Flash chromatography (SiO_2 , 20% EtOAc/Petrol) afforded the product as a white crystalline solid (0.125 g, 68%). ^1H NMR (CDCl_3 , 400 MHz): δ 10.10 (s, 1H), 8.00 (d, $J = 8.4$ Hz, 2H), 7.85 (d, $J = 8.4$ Hz, 2H); ^{13}C NMR (101 MHz, CDCl_3): 190.8, 138.8, 133.0, 130.0, 117.8, 117.7.

2-Thiophenecarbonitrile (11)¹⁹:

The compound was prepared according to the general procedure for the cyanation of aryl halides. Flash chromatography (SiO_2 , 1-5% Et₂O/Petrol) afforded the product as a colourless oil (0.125 g, 84%). ^1H NMR (CDCl_3 , 400 MHz): δ 7.64 (dd, $J = 3.6$, 1.1 Hz, 1H), 7.61 (dd, $J = 1.1$, 5.1 Hz, 1H), 7.14 (dd, 5.1, 3.6 Hz, 1H); ^{13}C NMR (101 MHz, CDCl_3): 137.6, 132.7, 127.8, 114.4, 110.1.

4-Methoxybenzotrile (12)²⁰:

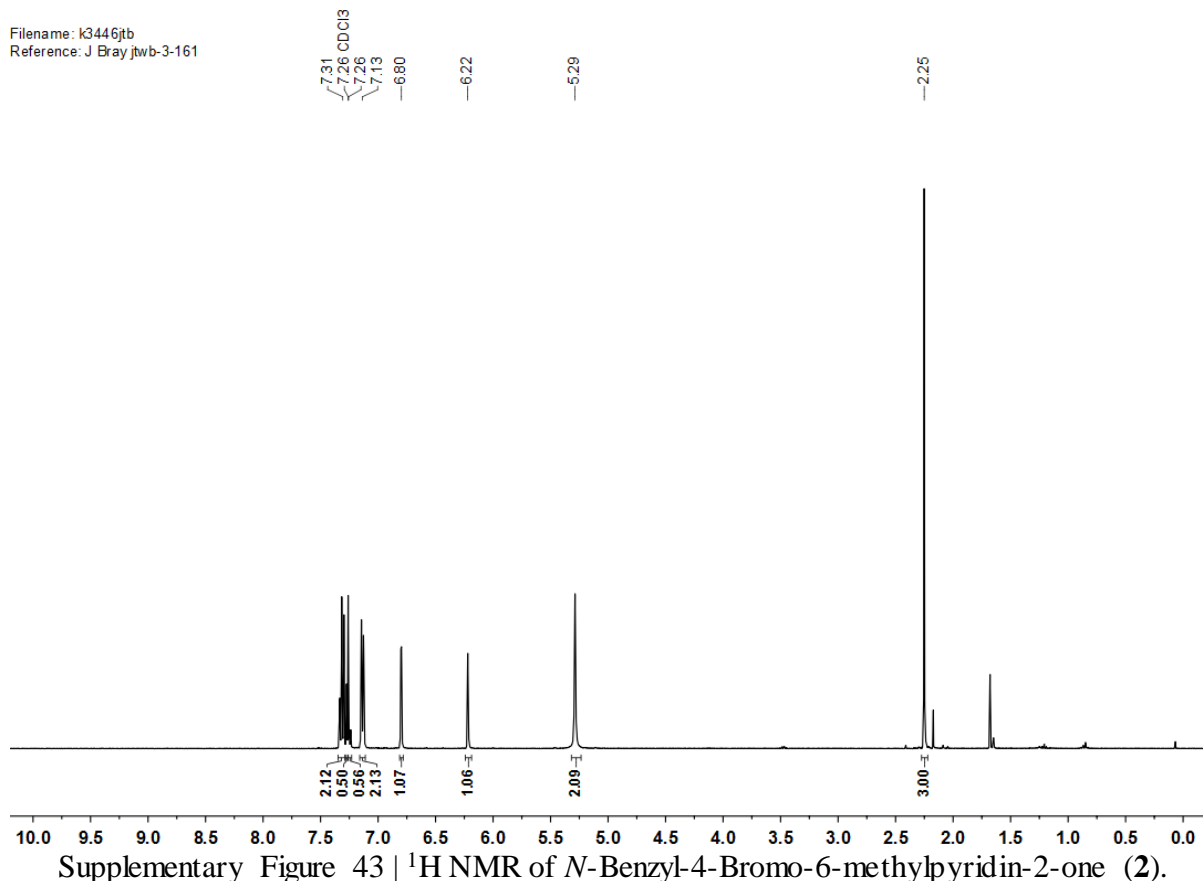
The compound was prepared per the general procedure for the cyanation of aryl halides. Flash chromatography (SiO₂, 20% Et₂O/Petrol) afforded the product as a white crystalline solid (0.057 g, 31%). ¹H NMR (CDCl₃, 400 MHz): δ; 7.59 (d, 8.9 Hz, 2H), 6.95 (d, 8.9 Hz, 2H), 3.86 (s, 3H); ¹³C NMR (101 MHz, CDCl₃): δ 162.9, 134.1, 119.3, 114.8, 104.1, 55.6.

Benzotrile (13)¹⁸:

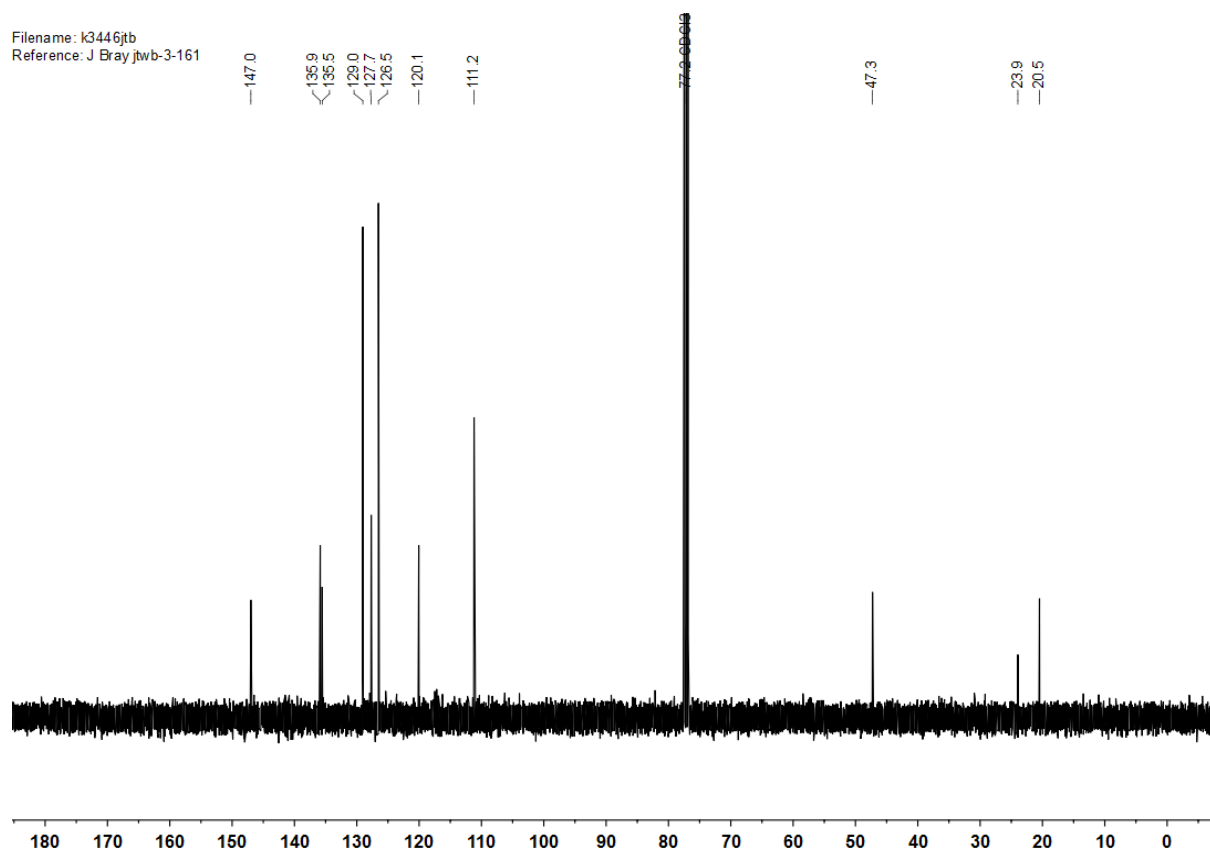
The compound was prepared per the general procedure for the cyanation of aryl halides. Flash chromatography (SiO₂, 5% Et₂O/Petrol) afforded the product as a colourless oil (0.141 g, 98%). ¹H NMR (CDCl₃, 400 MHz): δ 7.68-7.65 (m, 2H), 7.61 (dd, *J* = 7.6, 7.1 Hz, 1H), 7.48 (dd, *J* = 7.1, 7.1 Hz, 2H); ¹³C NMR (101 MHz, CDCl₃): δ 132.9, 132.3, 129.2, 119.0, 112.5.

4. Representative NMR spectra of organic compounds

4.1. *N*-Benzyl-4-bromo-6-methylpyridin-2-one (2)

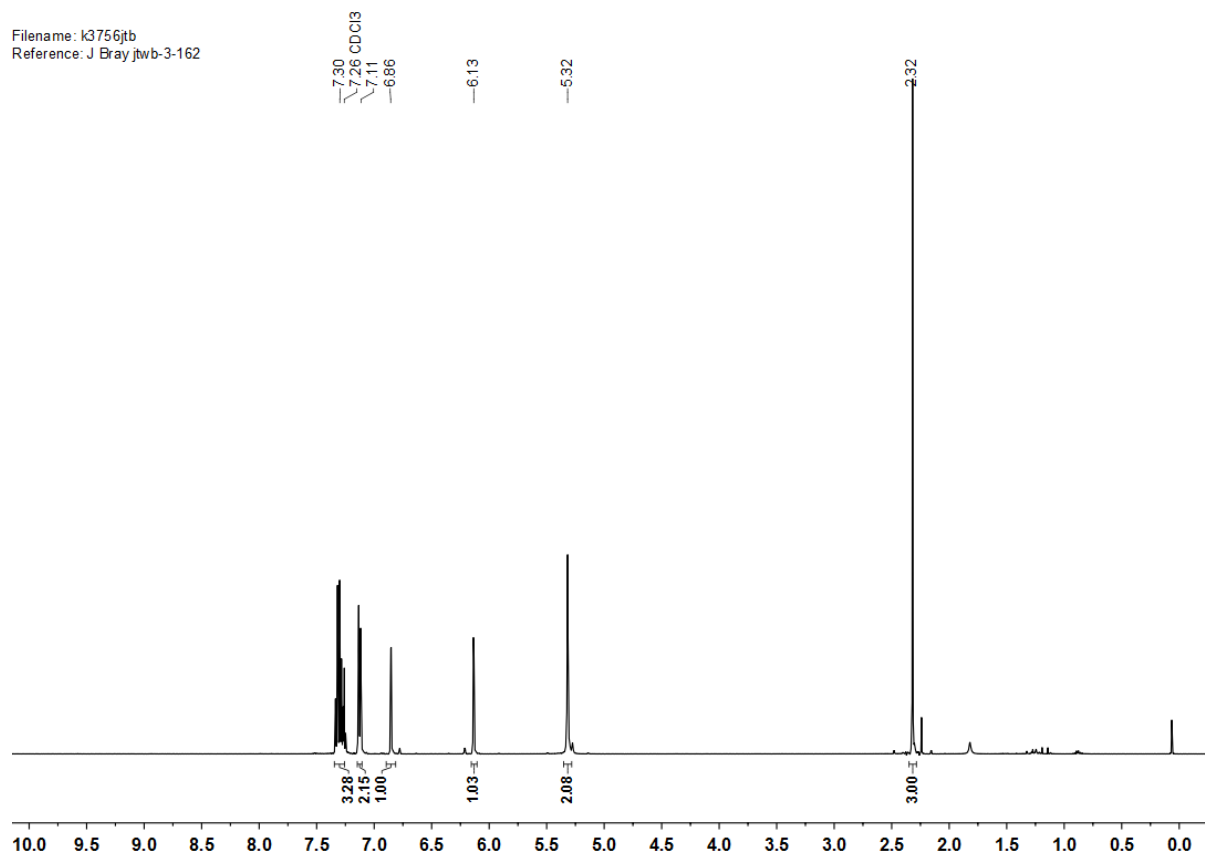


Filename: k3446jtb
Reference: J Bray.jtwb-3-161



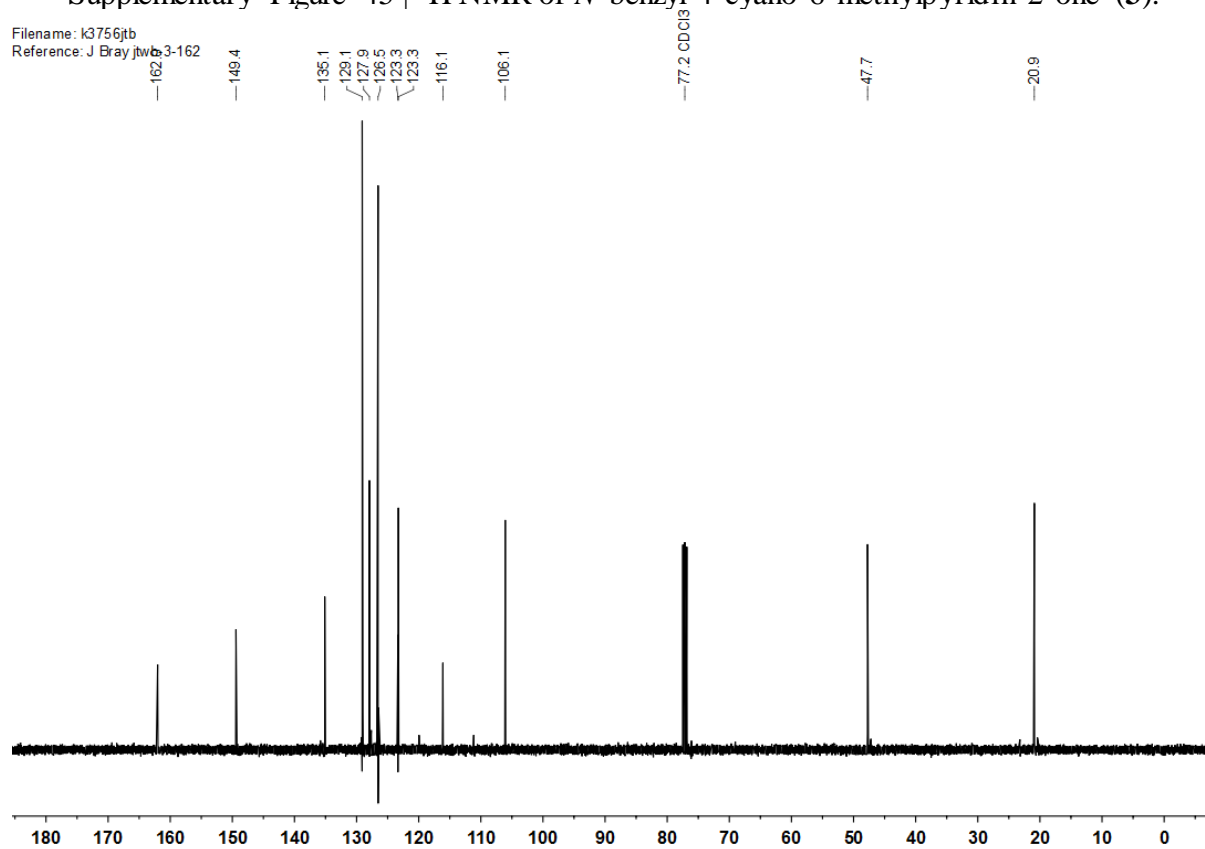
1.1. *N*-Benzyl-4-cyano-6-methylpyridin-2-one (3)

Filename: k3756jtb
Reference: J Bray jtwb-3-162



Supplementary Figure 45 | ¹H NMR of *N*-benzyl-4-cyano-6-methylpyridin-2-one (3).

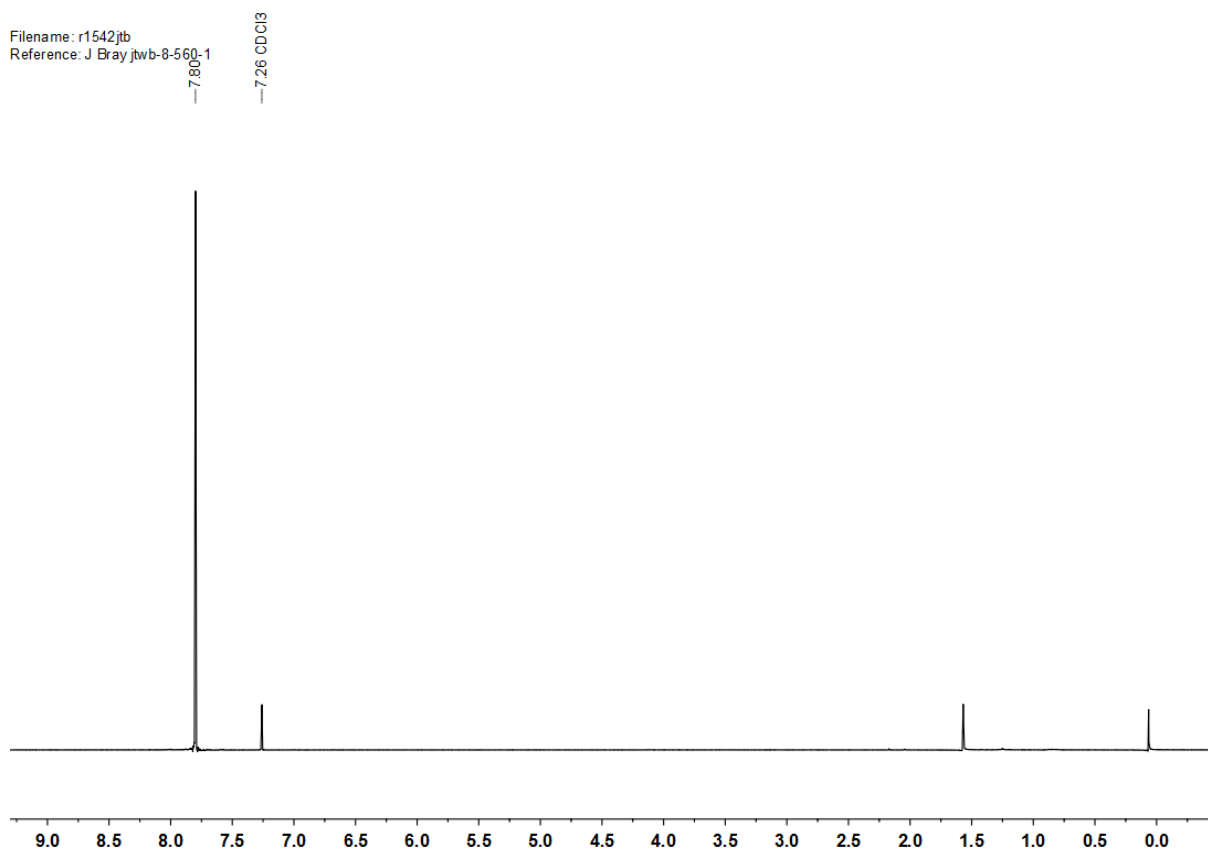
Filename: k3756jtb
Reference: J Bray jtwb-3-162



Supplementary Figure 46 | ¹³C NMR of *N*-benzyl-4-cyano-6-methylpyridin-2-one (3).

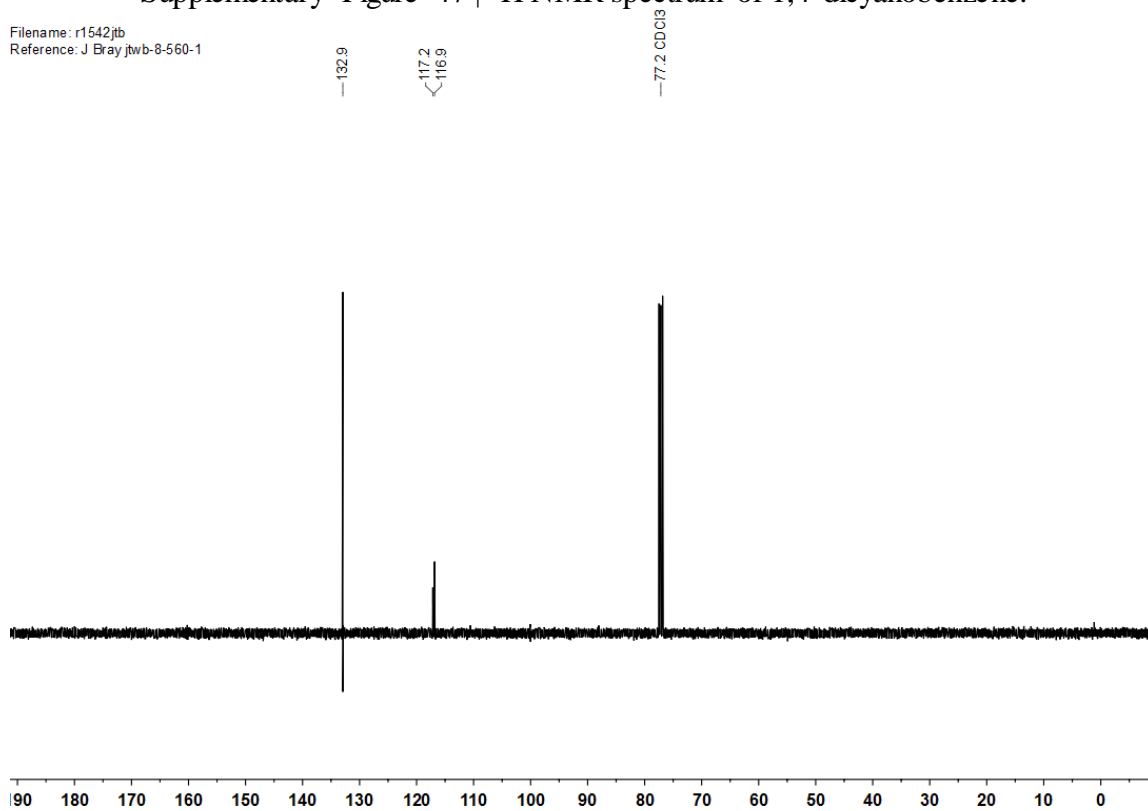
4.2. 1,4-Dicyanobenzene (4)

Filename: r1542jtb
Reference: J Bray jtwb-8-560-1



Supplementary Figure 47 | ¹H NMR spectrum of 1,4-dicyanobenzene.

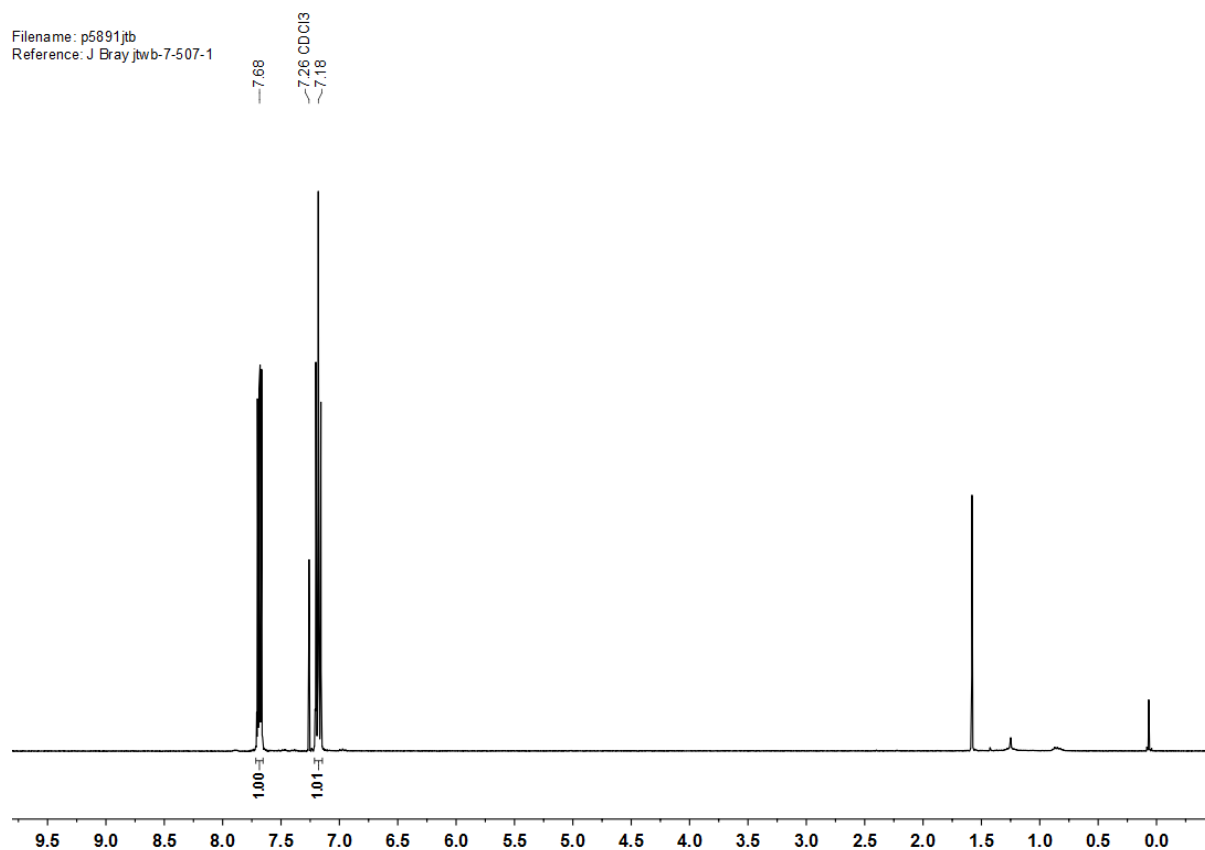
Filename: r1542jtb
Reference: J Bray jtwb-8-560-1



Supplementary Figure 48 | ¹³C NMR spectrum of 1,4-dicyanobenzene.

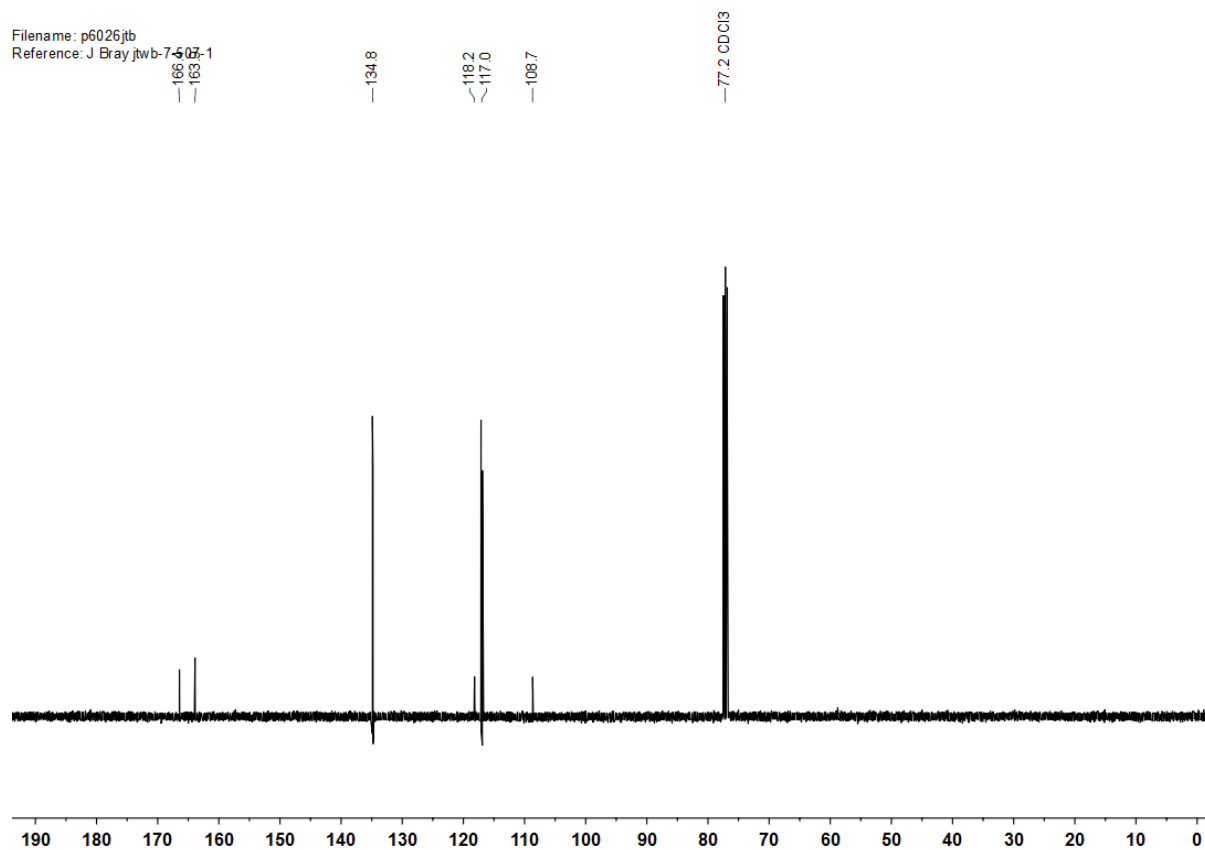
4.3. 4-Fluorobenzonitrile (5)

Filename: p5891jtb
Reference: J Bray jtwb-7-507-1



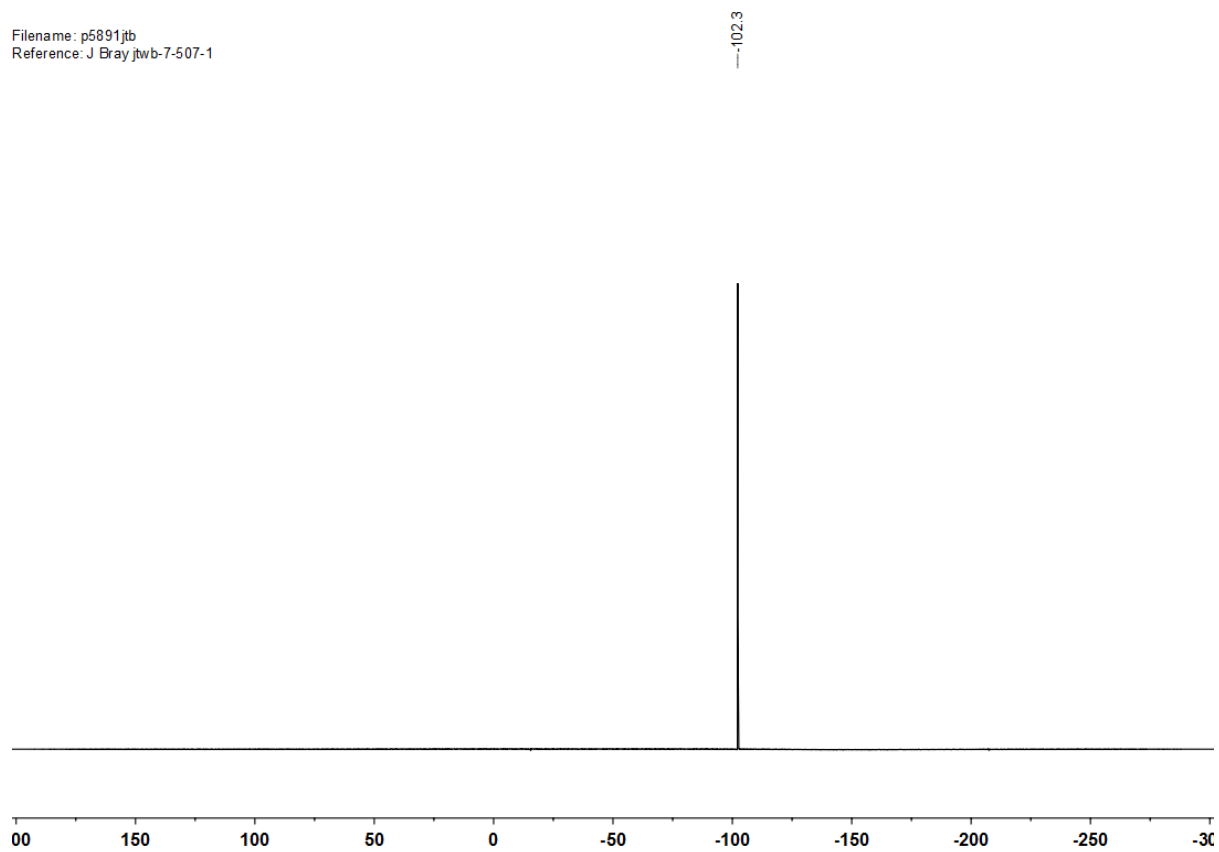
Supplementary Figure 49 | ¹H NMR spectrum of 4-fluorobenzonitrile.

Filename: p6026jtb
Reference: J Bray jtwb-7-507-1



Supplementary Figure 50 | ¹³C NMR spectrum of 4-fluorobenzonitrile.

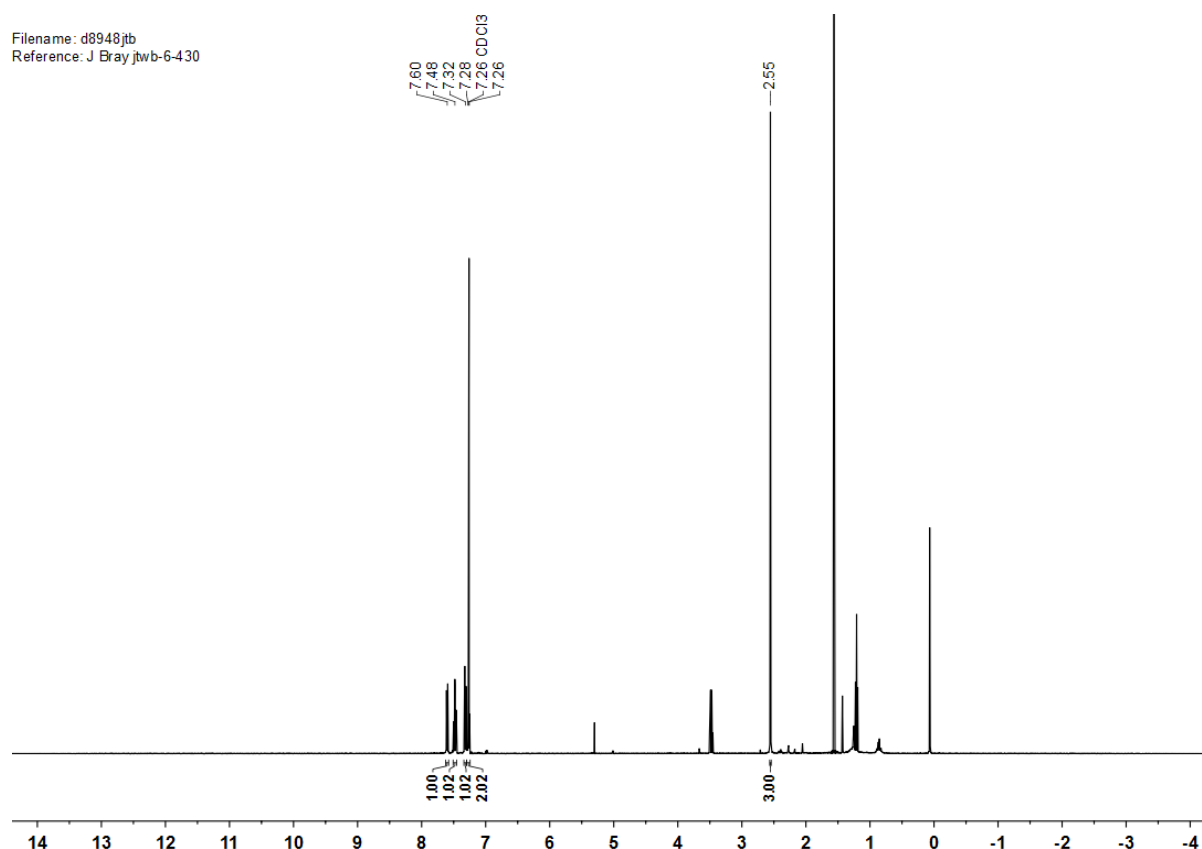
Filename: p5891jtb
Reference: J Bray.jtwb-7-507-1



Supplementary Figure 51 | ^{19}F NMR spectrum of 4-fluorobenzonitrile.

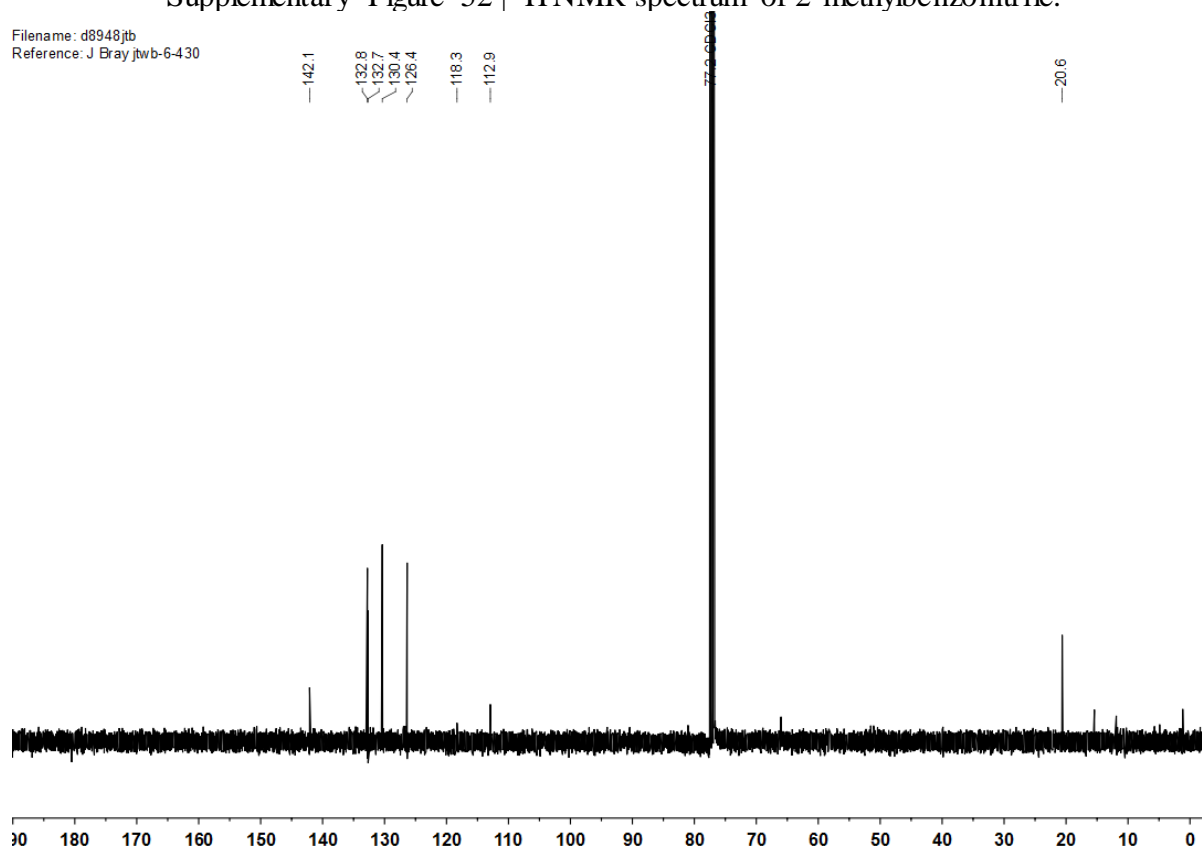
4.4. 2-Methylbenzointrile (6)

Filename: d8948jtb
Reference: J Bray jtwb-6-430



Supplementary Figure 52 | ¹H NMR spectrum of 2-methylbenzointrile.

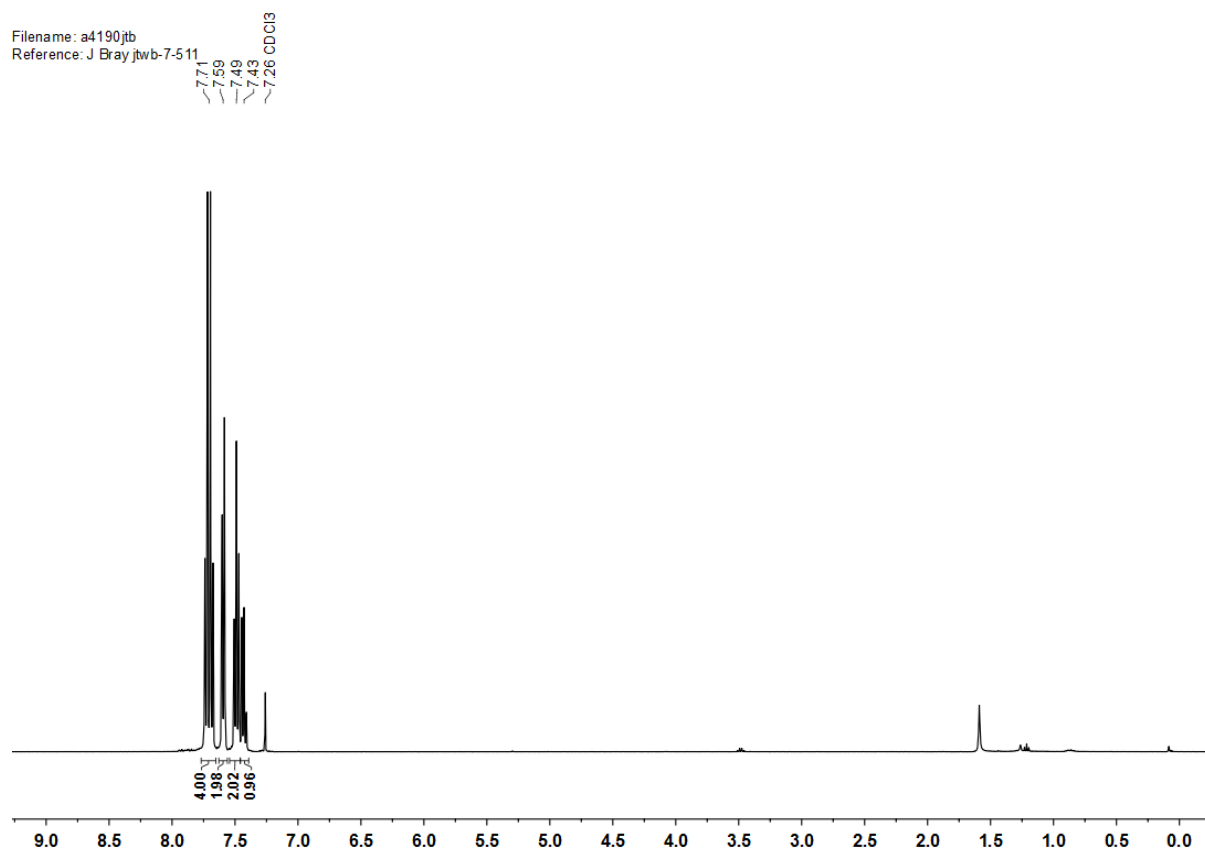
Filename: d8948jtb
Reference: J Bray jtwb-6-430



Supplementary Figure 53 | ¹³C NMR spectrum of 2-methylbenzointrile.

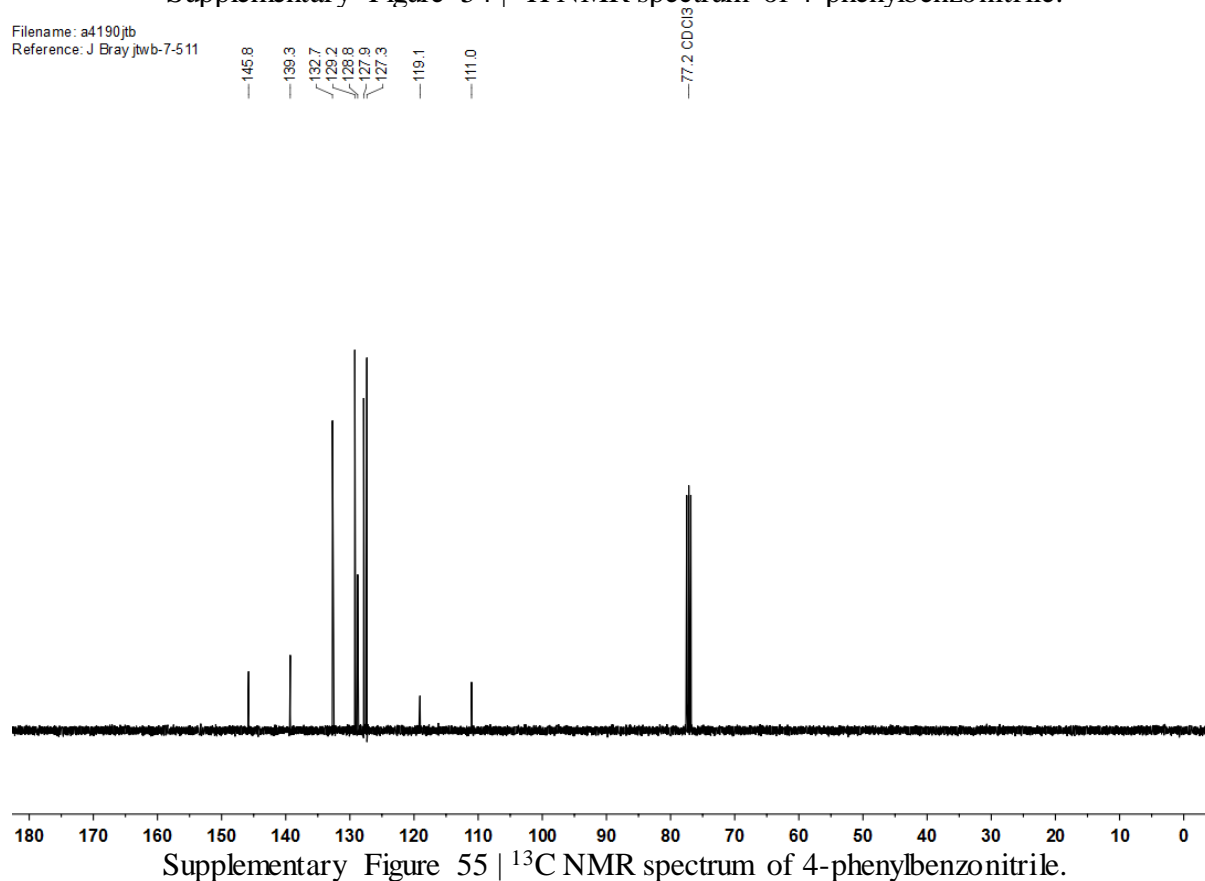
4.5. 4-Phenylbenzointrile (7)

Filename: a4190jtb
Reference: J Bray jtwb-7-511



Supplementary Figure 54 | ¹H NMR spectrum of 4-phenylbenzointrile.

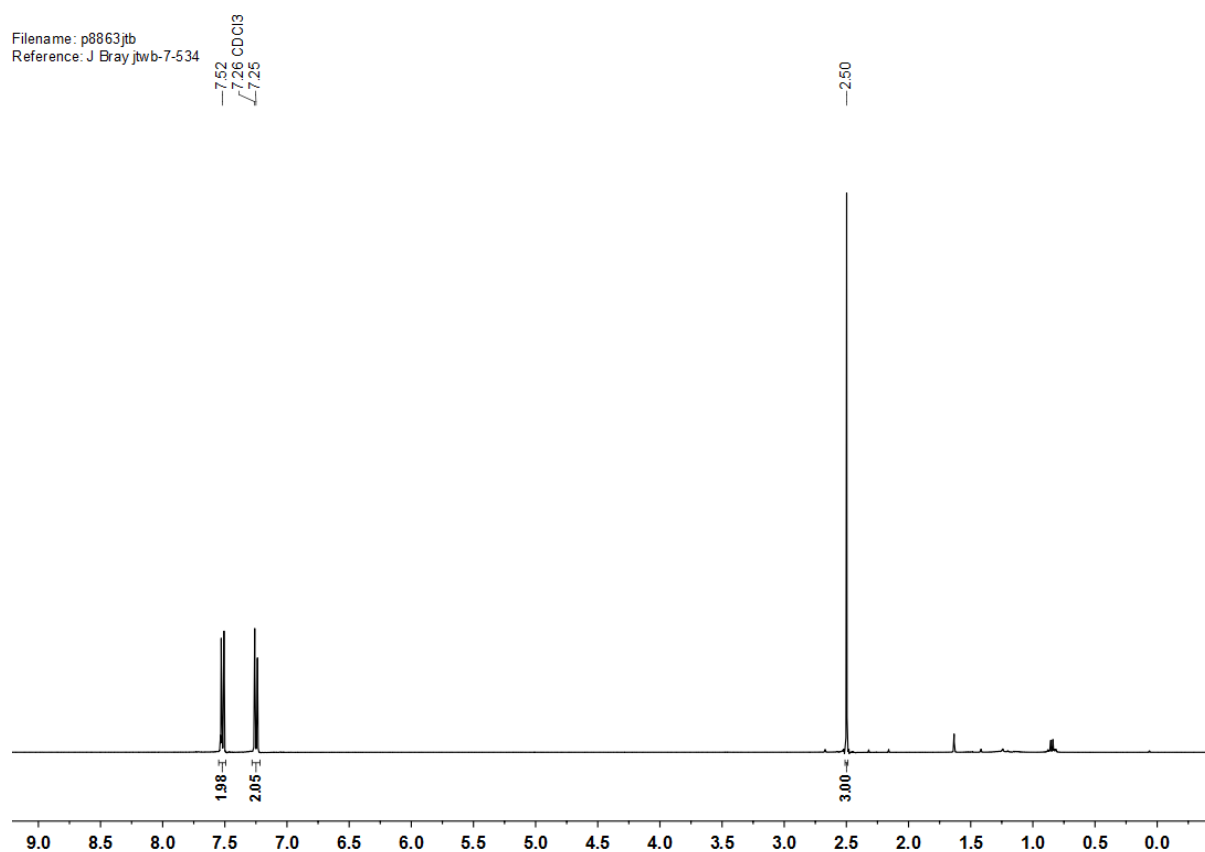
Filename: a4190jtb
Reference: J Bray jtwb-7-511



Supplementary Figure 55 | ¹³C NMR spectrum of 4-phenylbenzointrile.

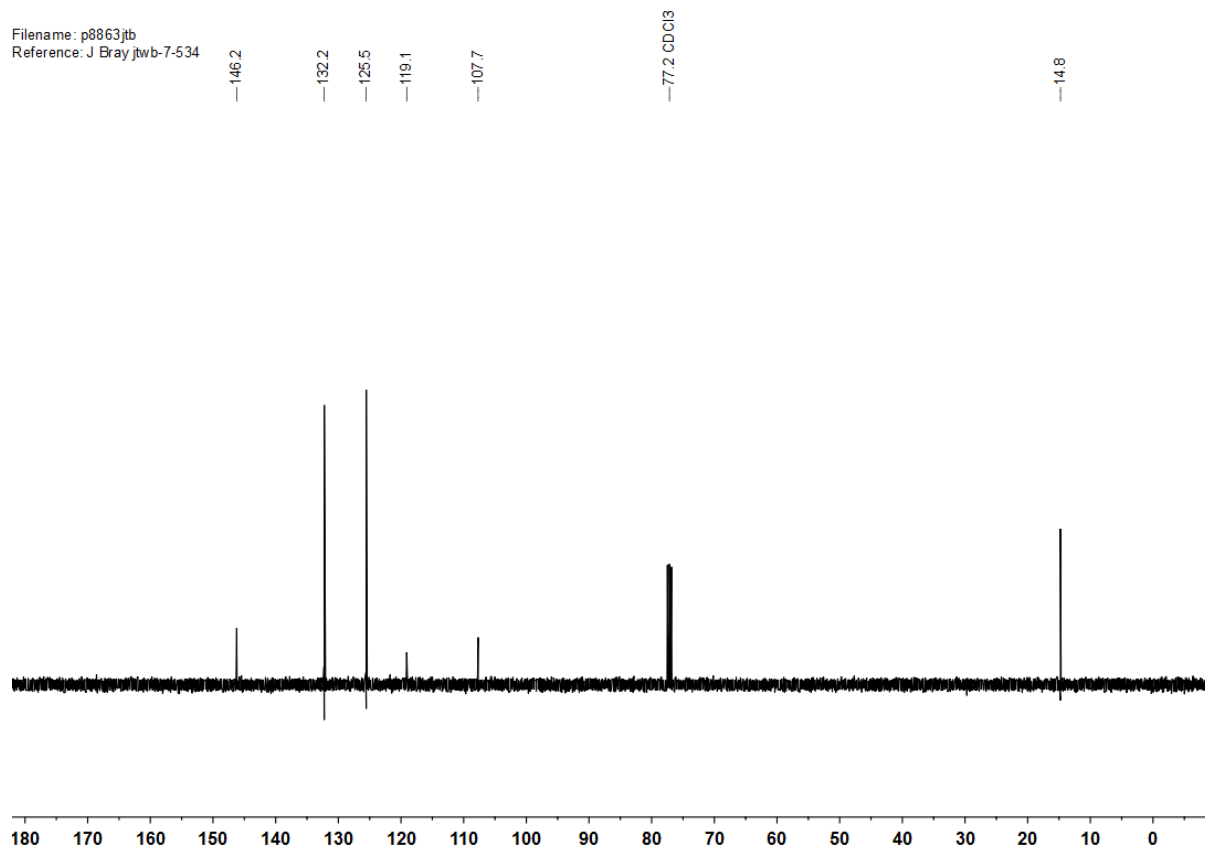
4.6. 4-(Methylthio)benzotrile (8)

Filename: p8863jtb
Reference: J Bray.jtwb-7-534



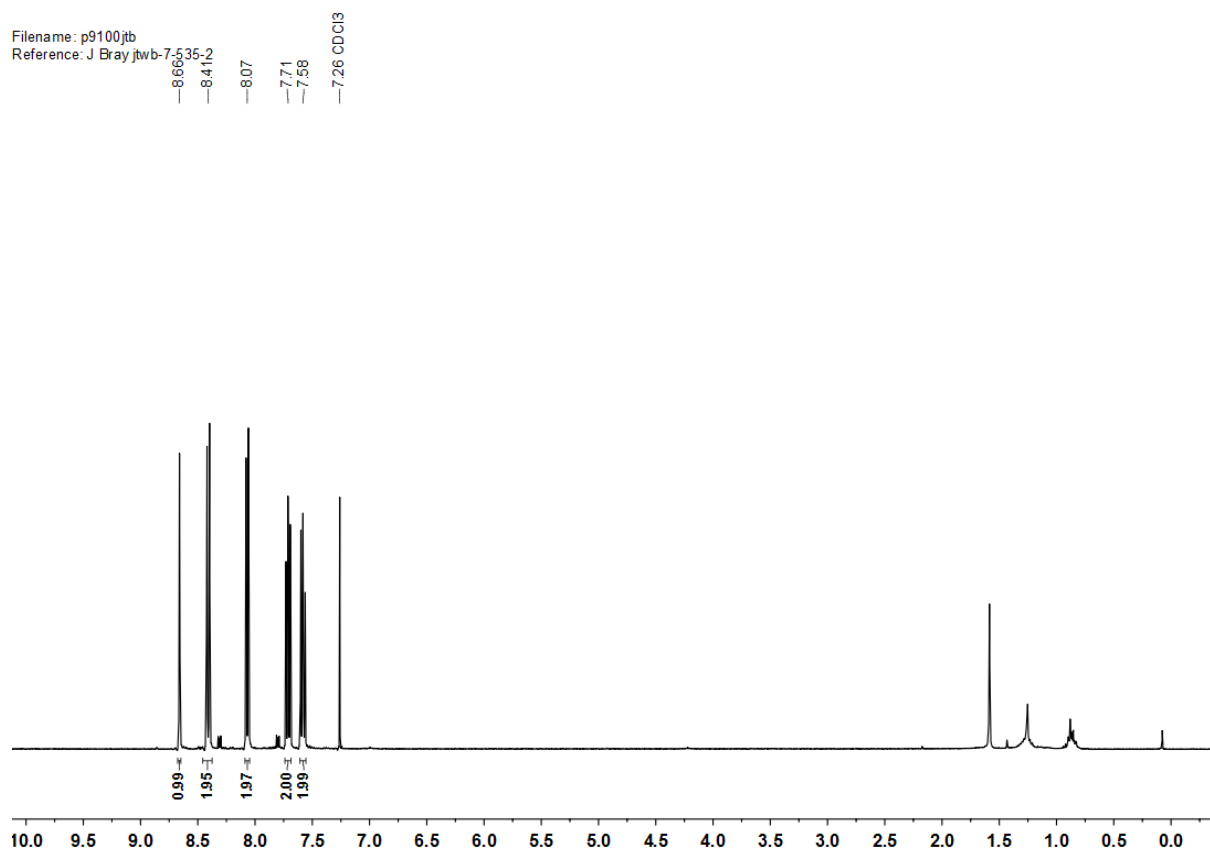
Supplementary Figure 56 | ¹H NMR spectrum of 4-(Methylthio)benzotrile.

Filename: p8863jtb
Reference: J Bray.jtwb-7-534

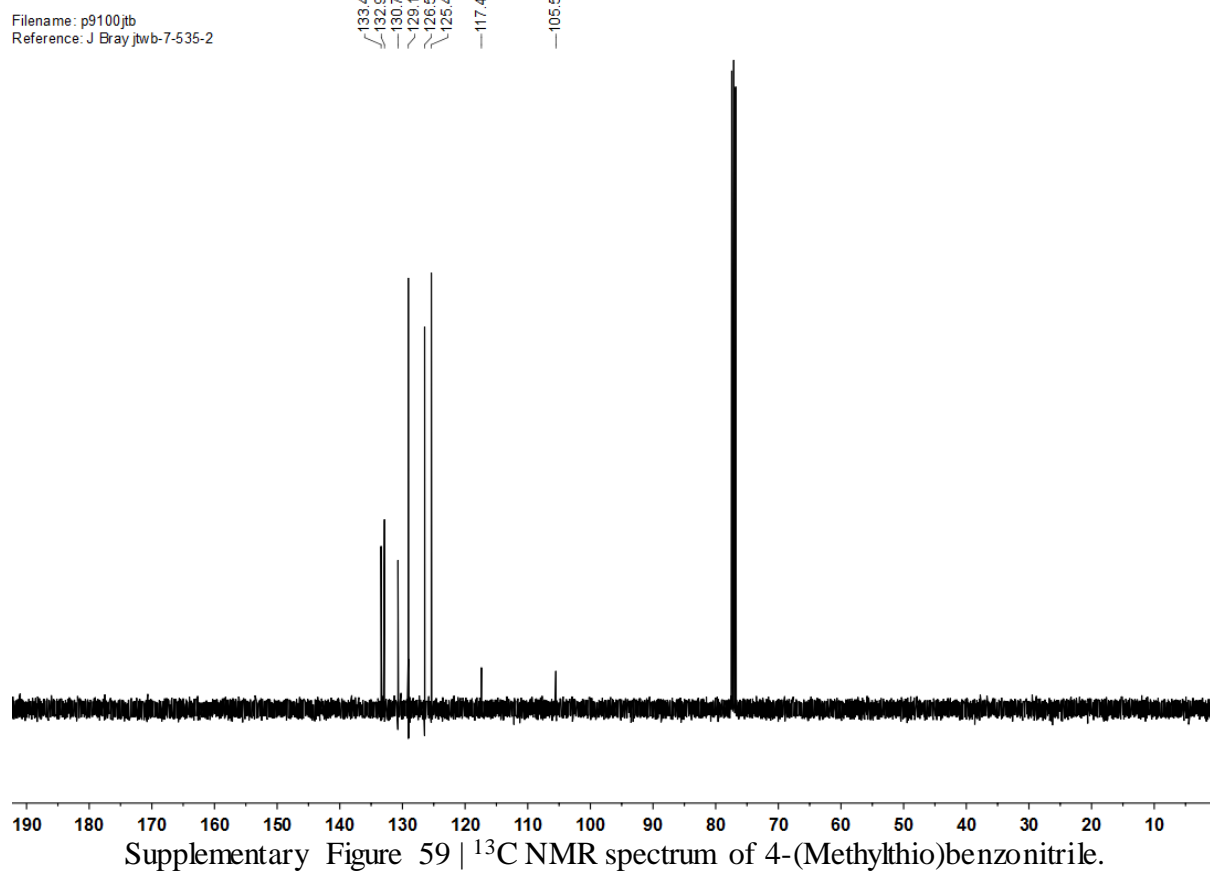


Supplementary Figure 57 | ¹³C NMR spectrum of 4-(Methylthio)benzotrile.

4.7. 9-Cyanoanthracene (9)

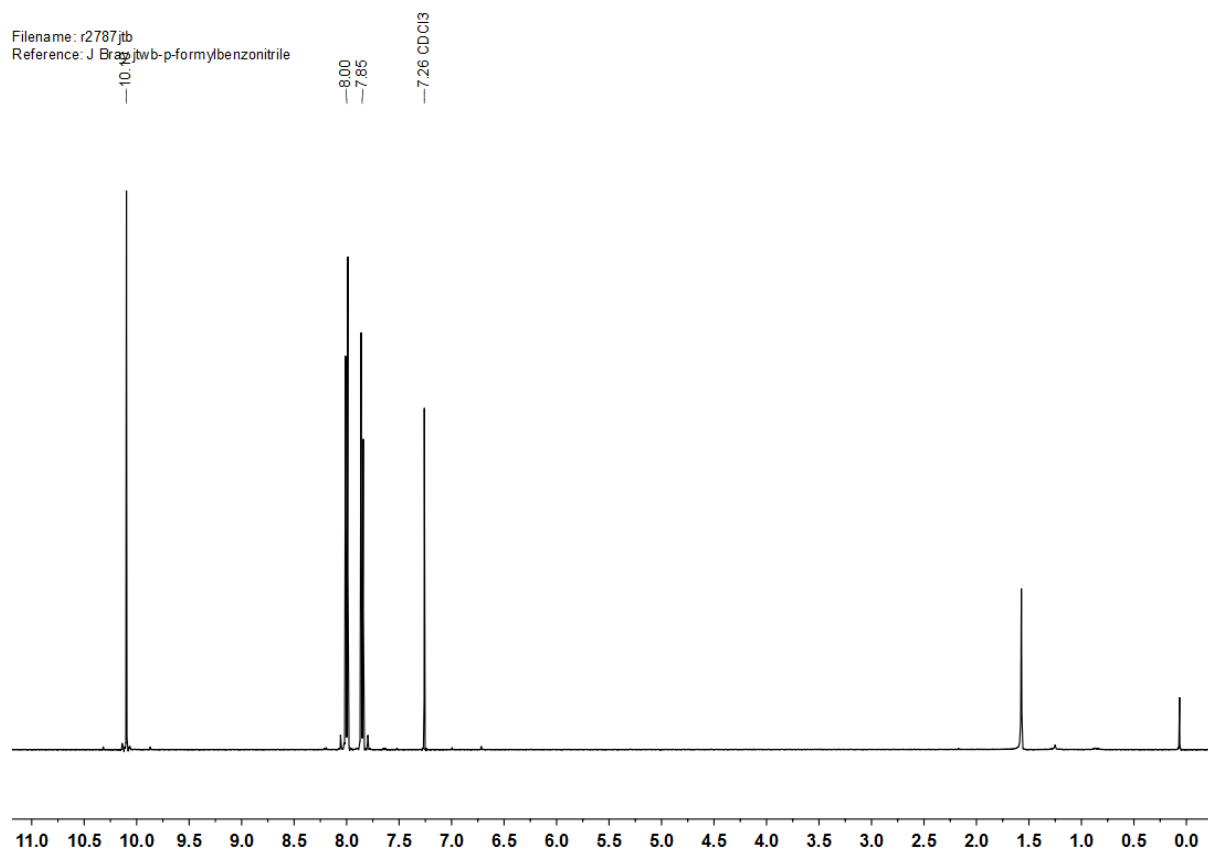


Supplementary Figure 58 | ¹H NMR spectrum of 4-(Methylthio)benzonitrile.

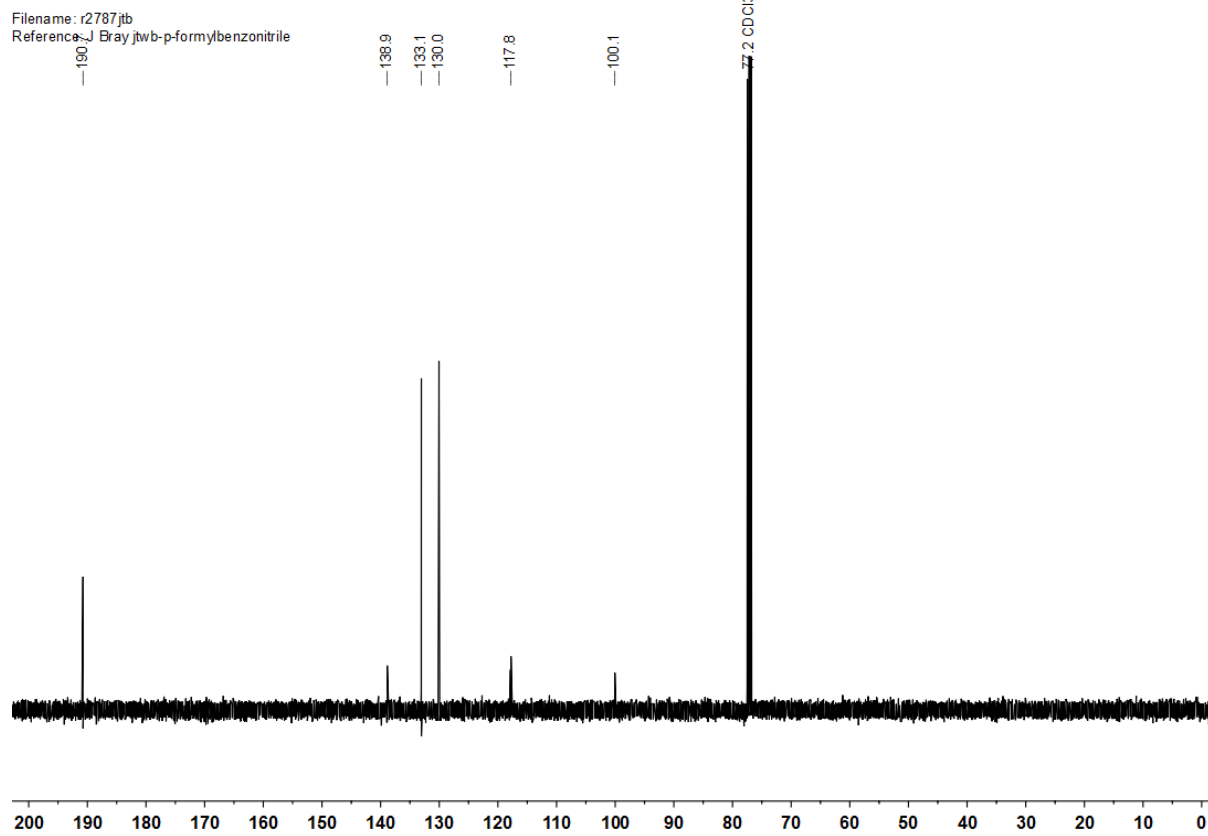


Supplementary Figure 59 | ¹³C NMR spectrum of 4-(Methylthio)benzonitrile.

4.8. 4-Formylbenzonitrile (10)



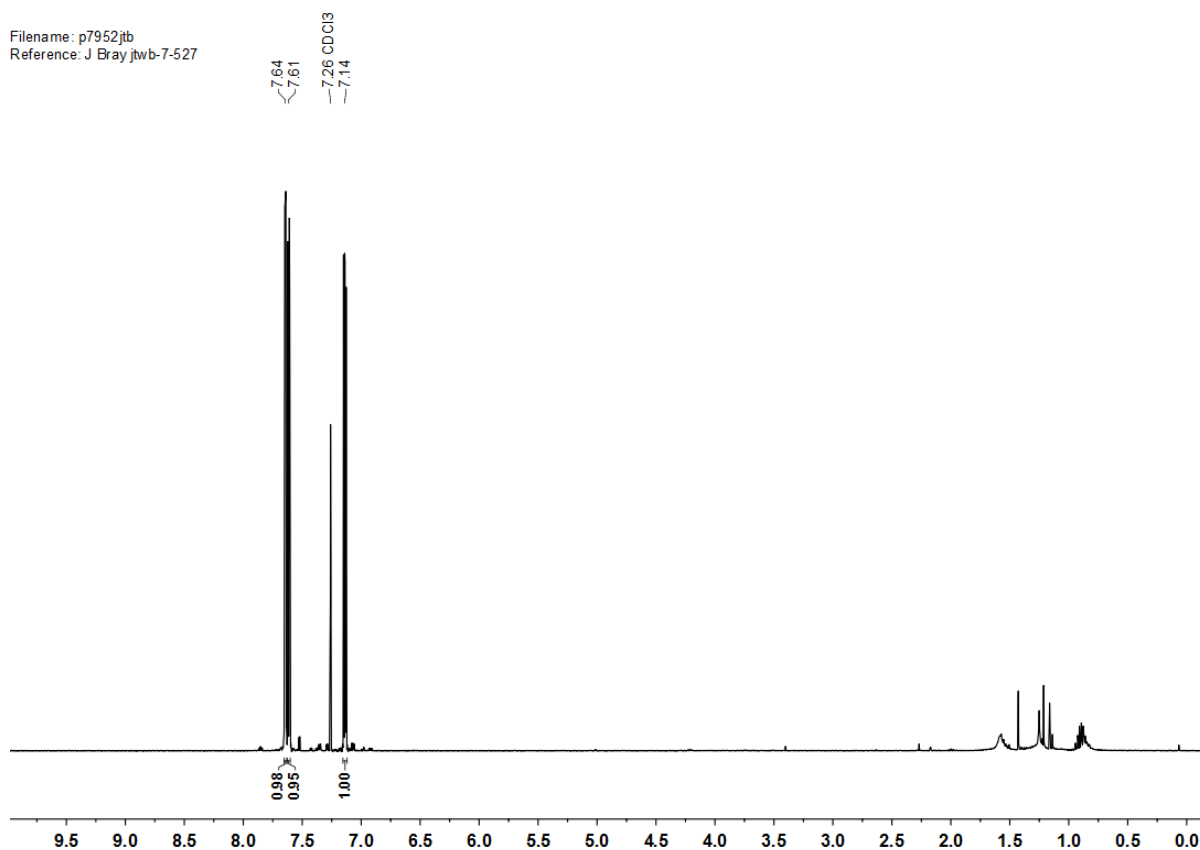
Supplementary Figure 60 | ^1H NMR spectrum of 4-Formylbenzonitrile.



Supplementary Figure 61 | ^{13}C NMR spectrum of 4-Formylbenzonitrile.

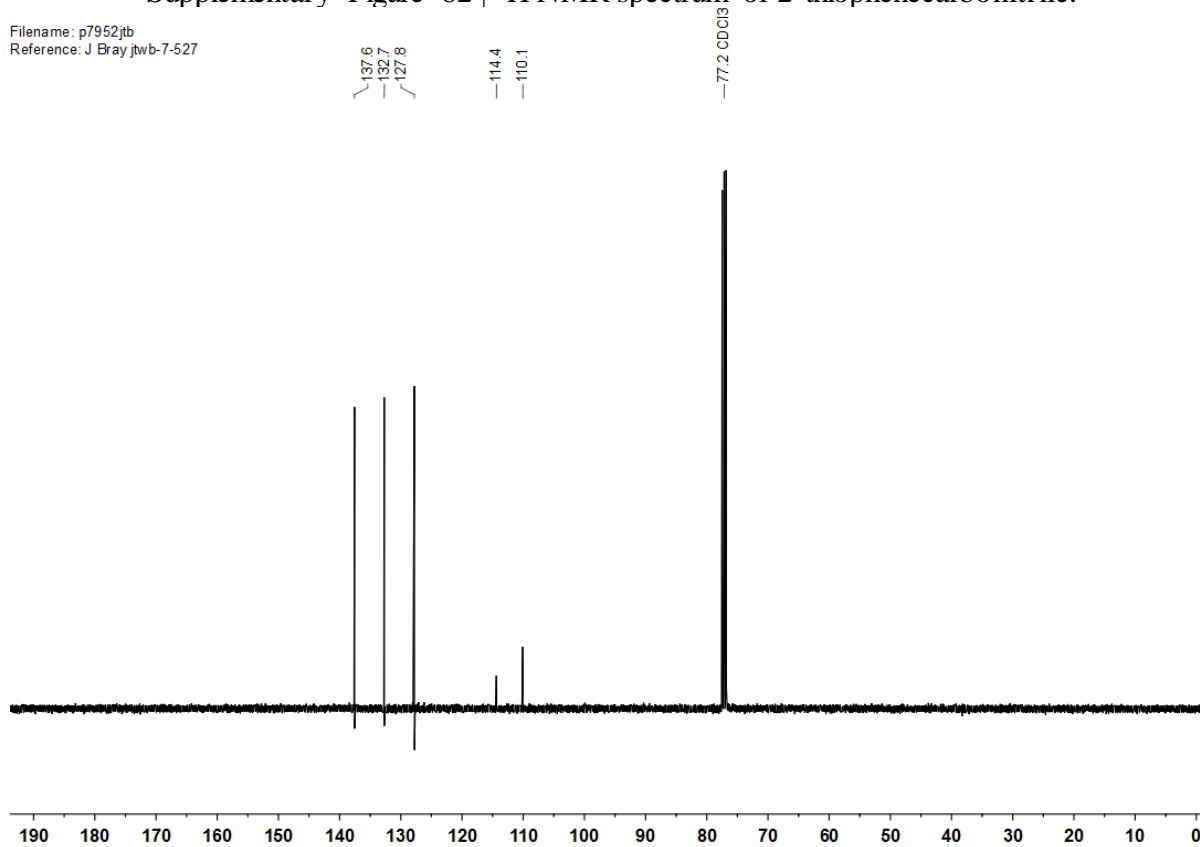
4.9. 2-Thiophenecarbonitrile (11)

Filename: p7952jtb
Reference: J Bray jtwb-7-527



Supplementary Figure 62 | ¹H NMR spectrum of 2-thiophenecarbonitrile.

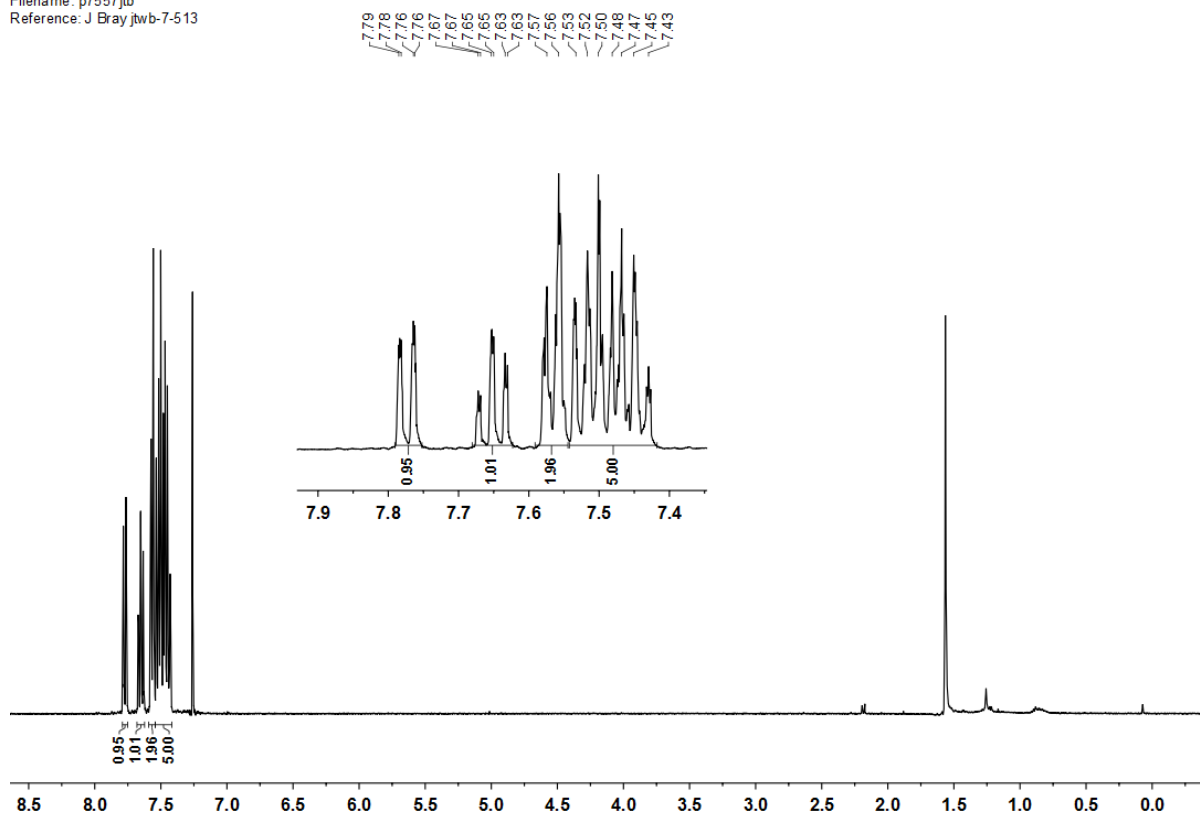
Filename: p7952jtb
Reference: J Bray jtwb-7-527



Supplementary Figure 63 | ¹³C NMR spectrum of 2-thiophenecarbonitrile.

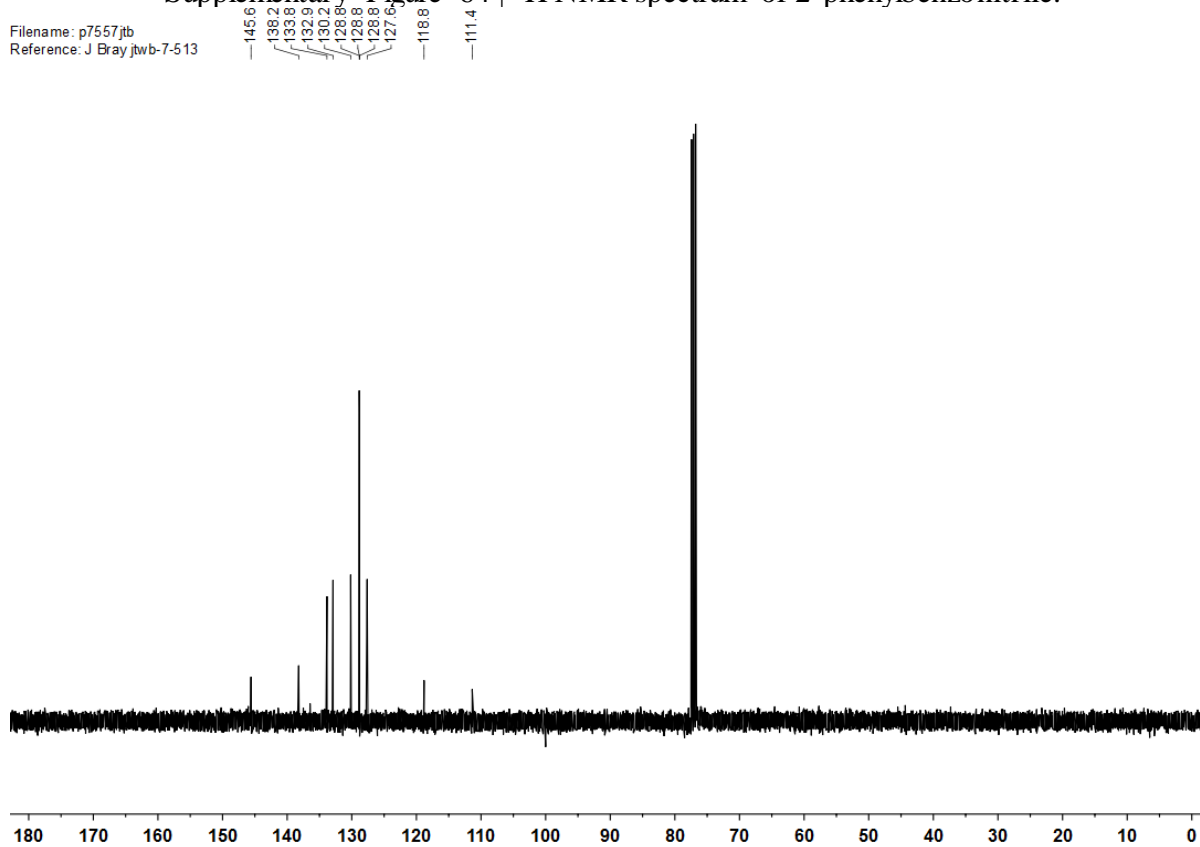
4.10. 2-Phenylbenzonitrile (12)

Filename: p7557.jtb
Reference: J Bray jtwb-7-513



Supplementary Figure 64 | ^1H NMR spectrum of 2-phenylbenzonitrile.

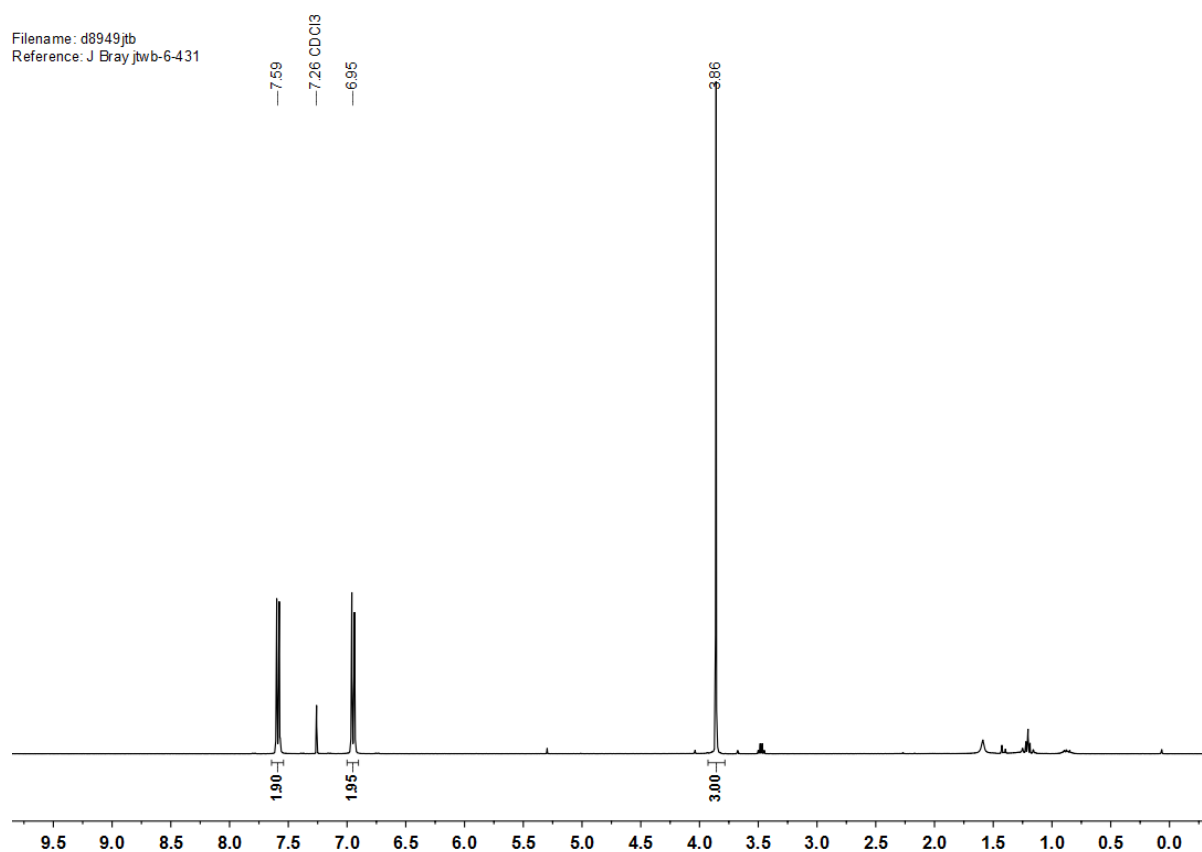
Filename: p7557.jtb
Reference: J Bray jtwb-7-513



Supplementary Figure 65 | ^{13}C NMR spectrum of 2-phenylbenzonitrile.

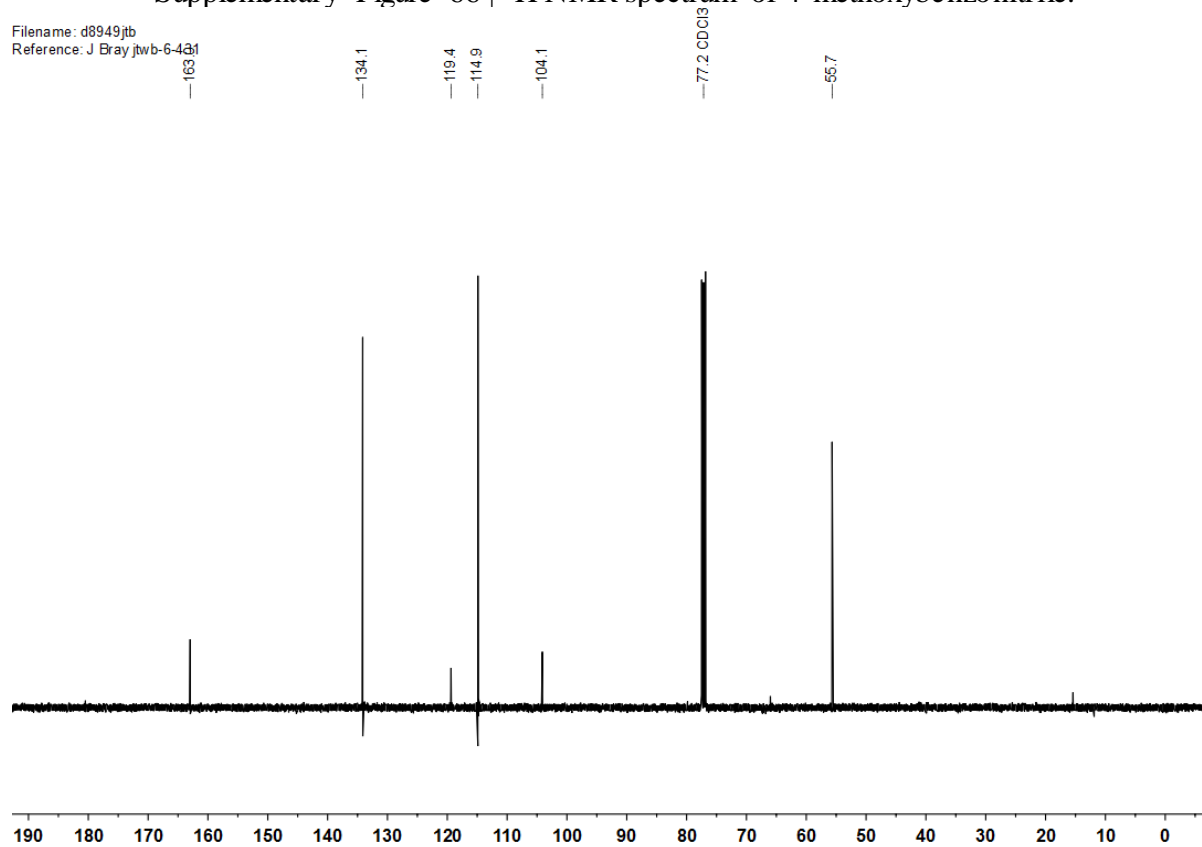
4.11. 4-Methoxybenzonitrile (13)

Filename: d8949jtb
Reference: J Bray jtwb-6-431



Supplementary Figure 66 | ¹H NMR spectrum of 4-methoxybenzonitrile.

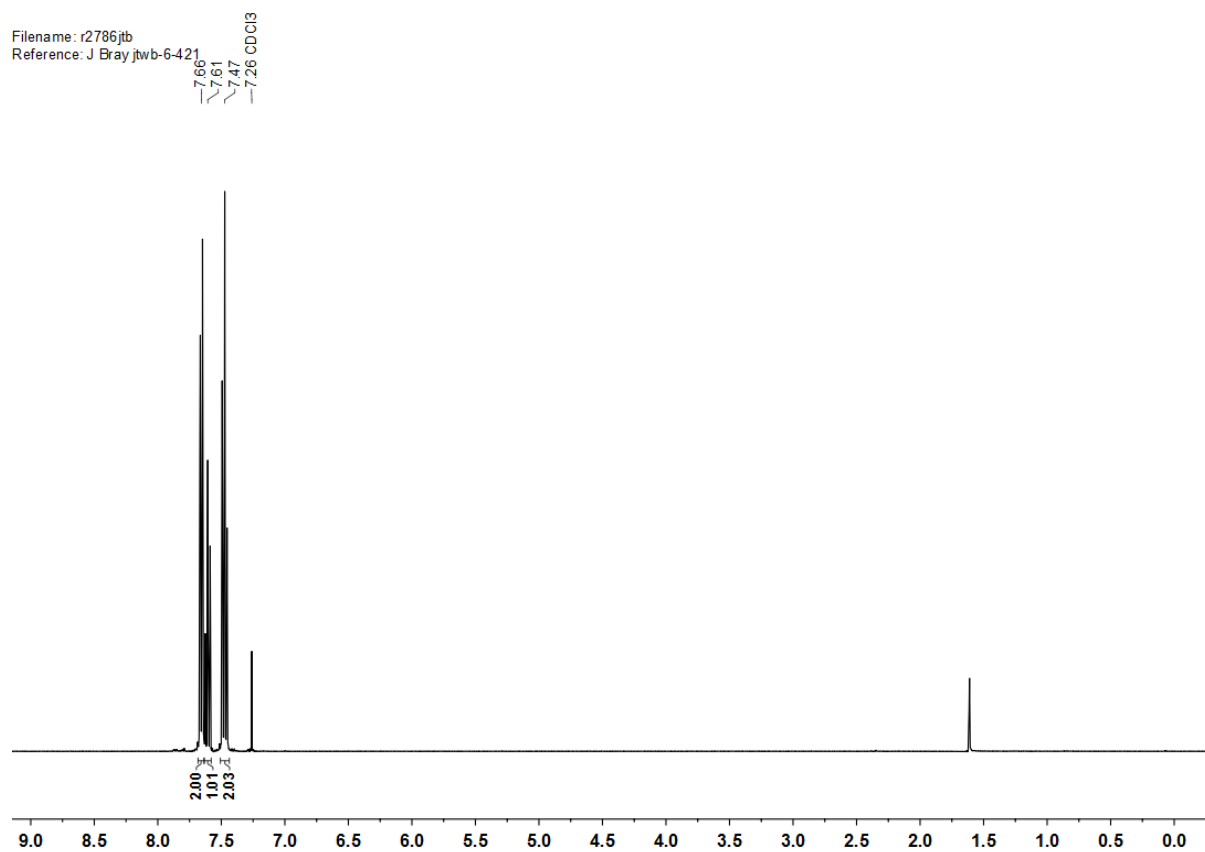
Filename: d8949jtb
Reference: J Bray jtwb-6-431



Supplementary Figure 67 | ¹³C NMR spectrum of 4-methoxybenzonitrile.

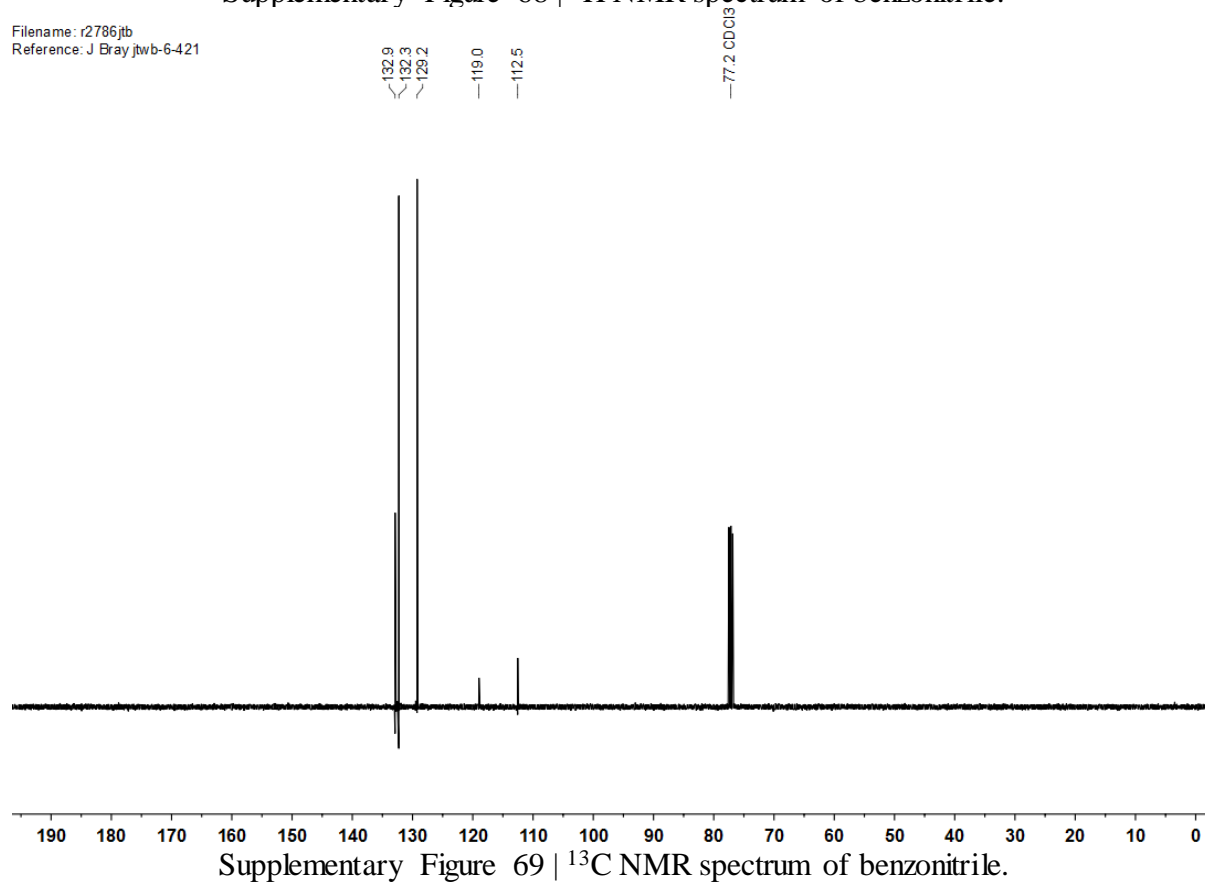
4.12. Benzonitrile (14)

Filename: r2786jtb
Reference: J Bray jtwb-6-421



Supplementary Figure 68 | ¹H NMR spectrum of benzonitrile.

Filename: r2786jtb
Reference: J Bray jtwb-6-421

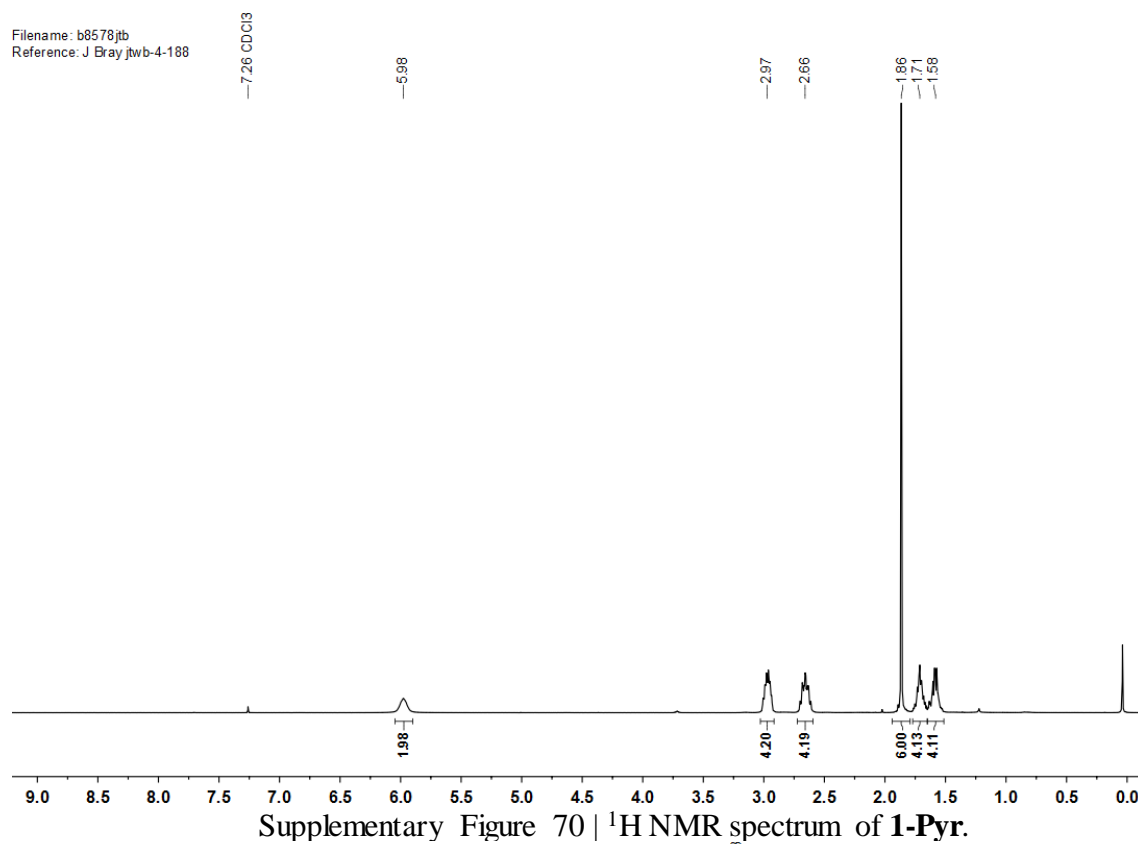


Supplementary Figure 69 | ¹³C NMR spectrum of benzonitrile.

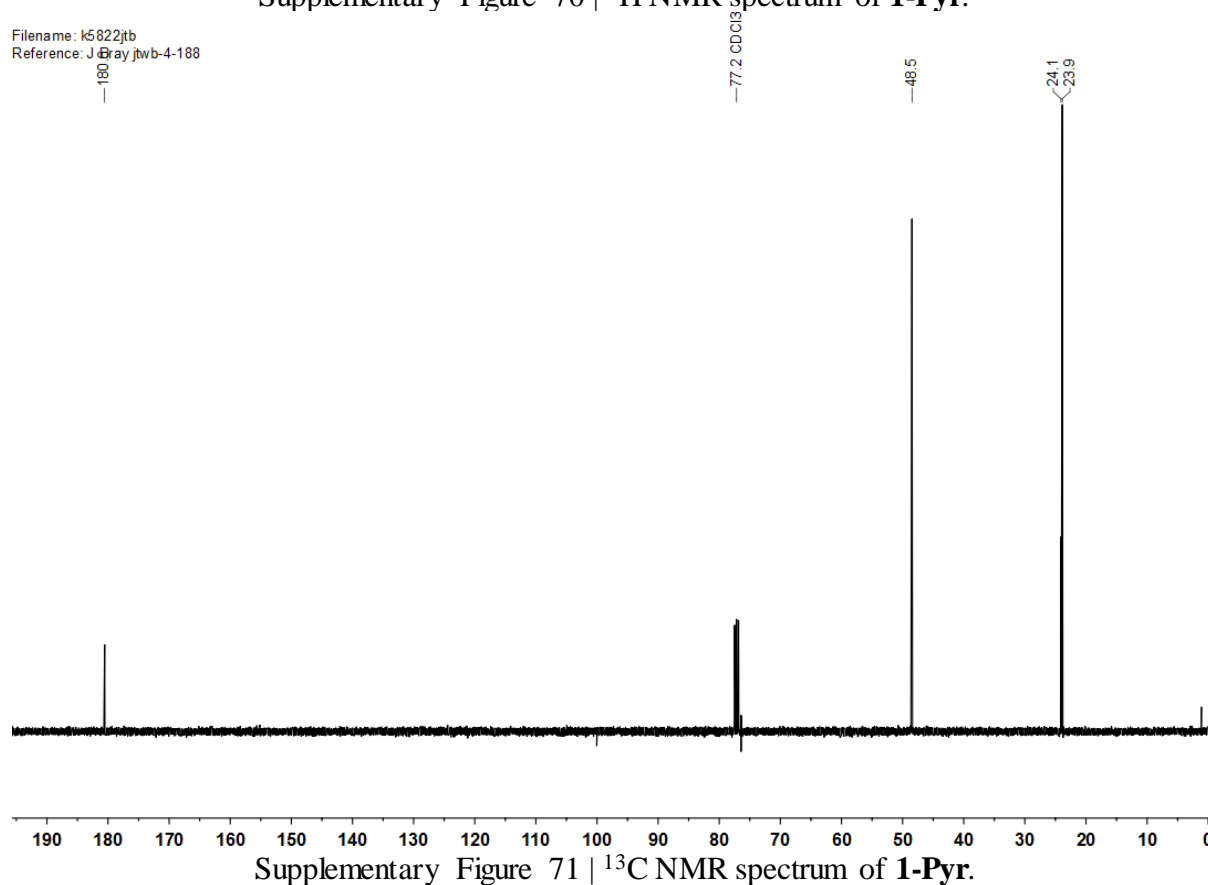
5. NMR spectra of Pd amine complexes

5.1. 1-Pyr

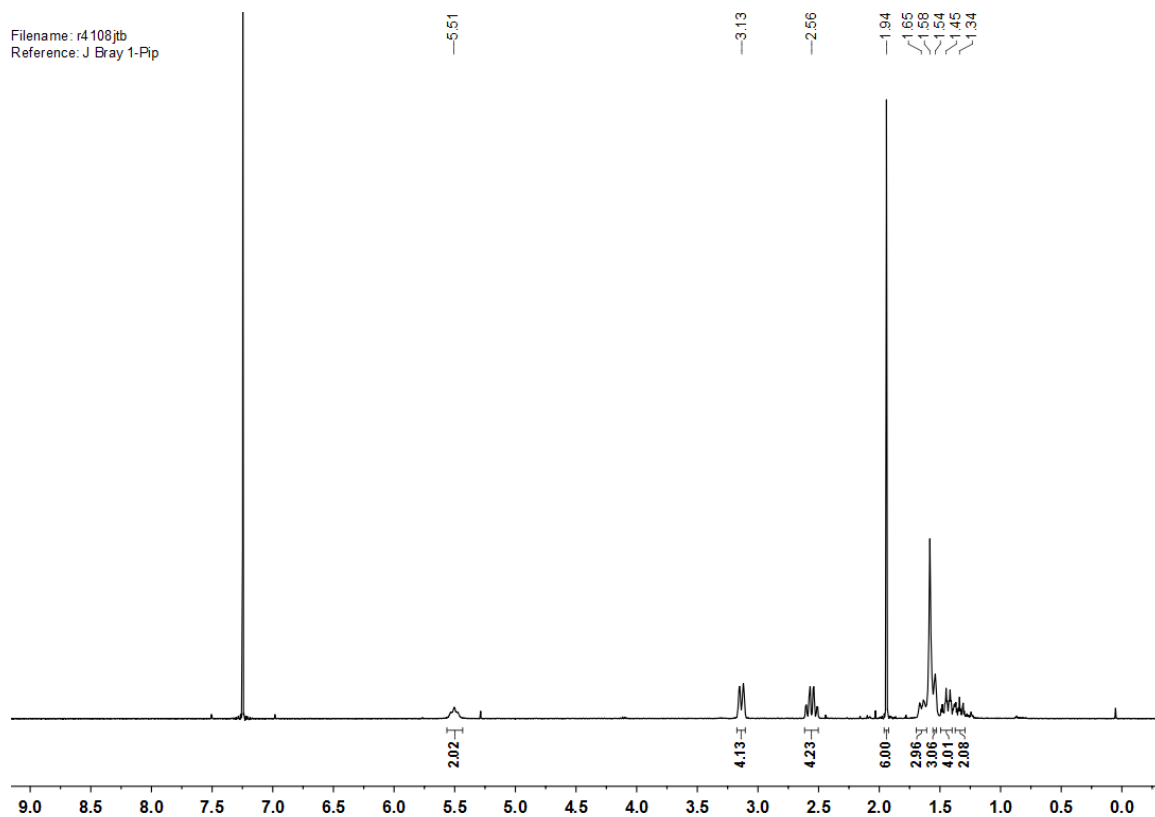
Filename: b8578jtb
Reference: J Bray jtwb-4-188



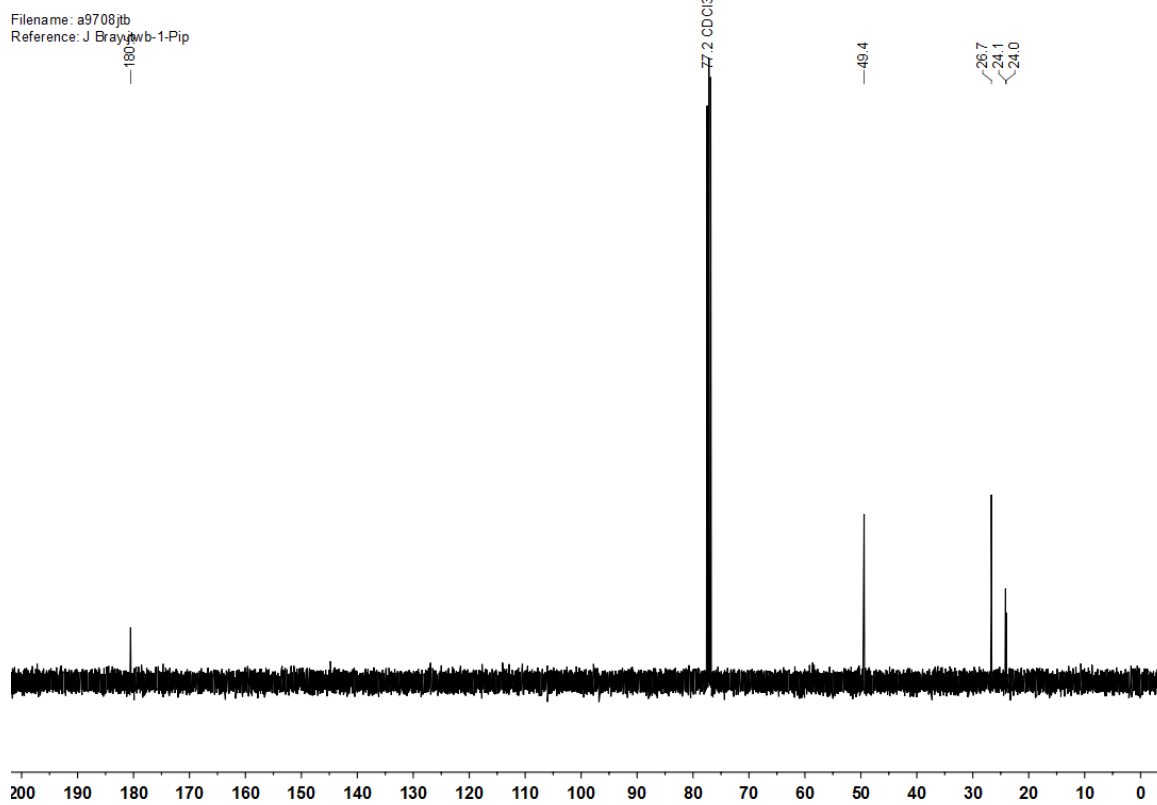
Filename: k5822jtb
Reference: J Bray jtwb-4-188



5.2. 1-Pip



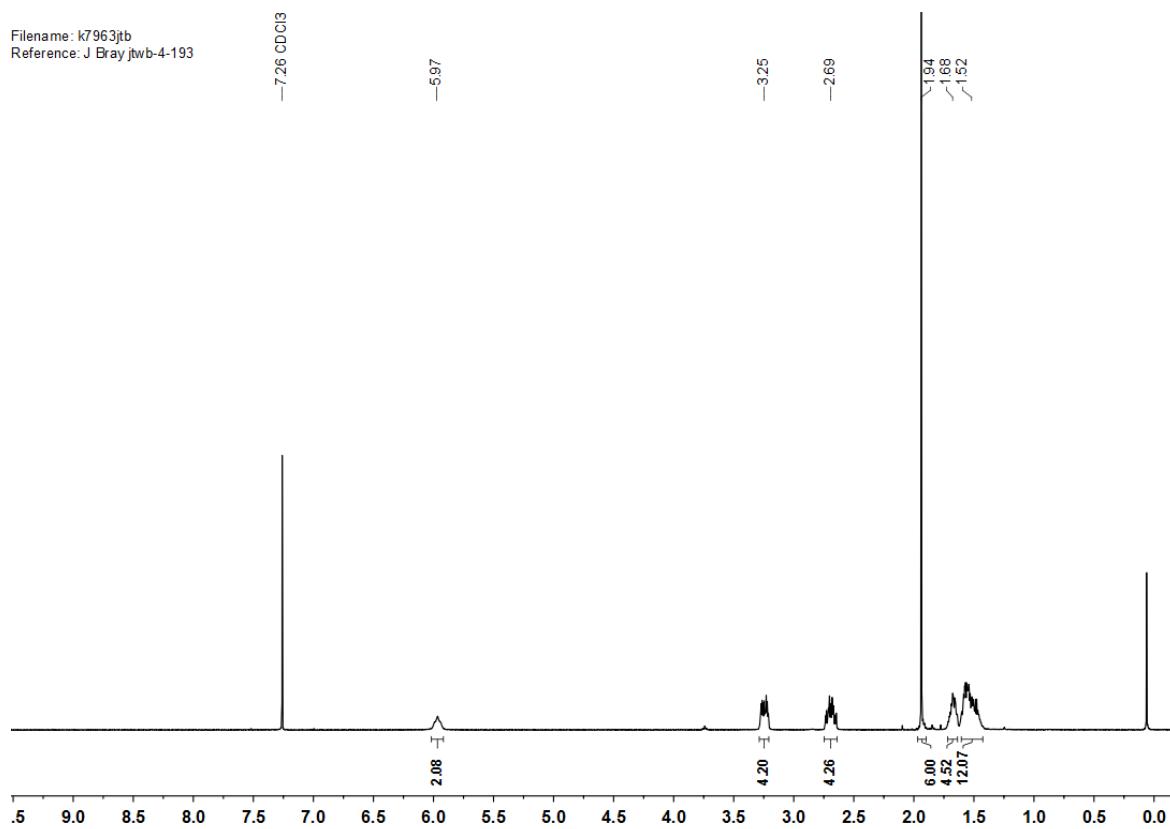
Supplementary Figure 72 | ¹H NMR of 1-Pip.



Supplementary Figure 73 | ¹³C NMR of 1-Pip.

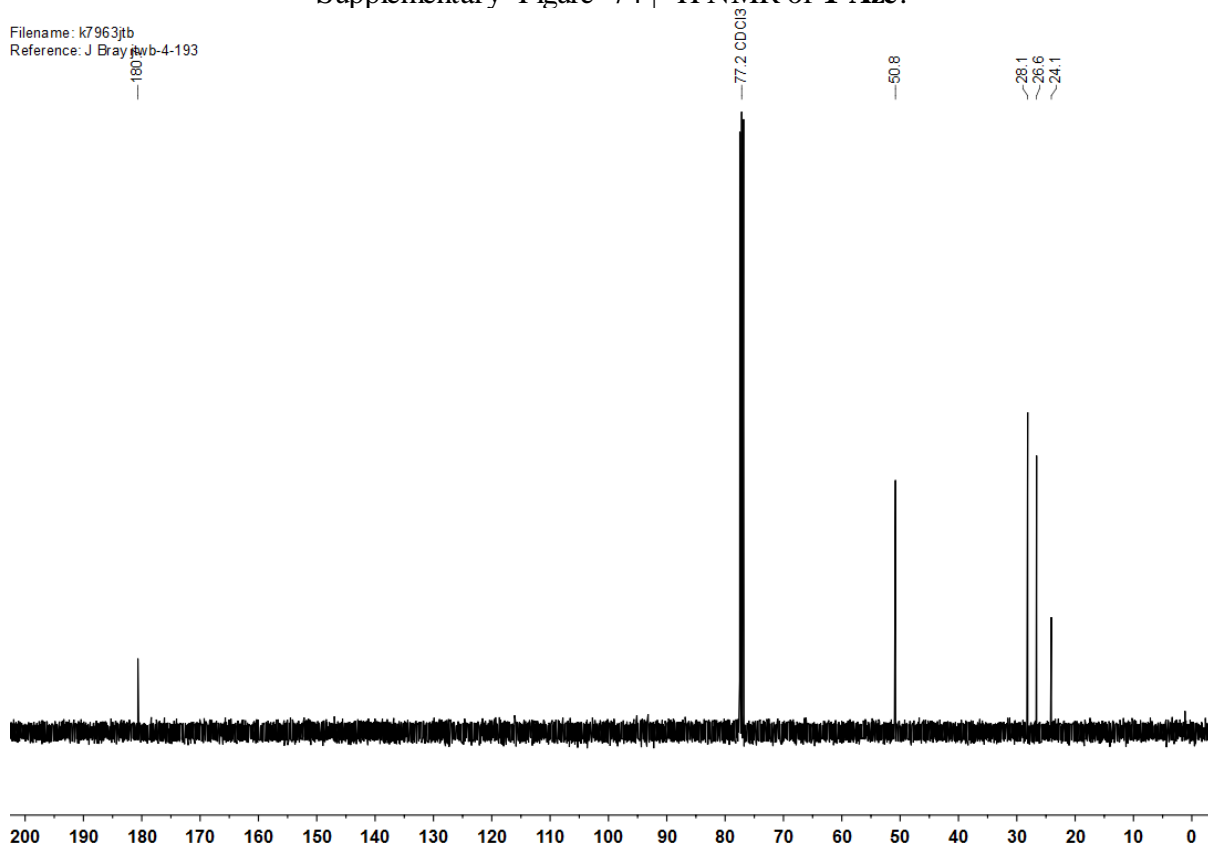
5.3. 1-Aze

Filename: k7963jtb
Reference: J Bray jtwb-4-193



Supplementary Figure 74 | ¹H NMR of **1-Aze**.

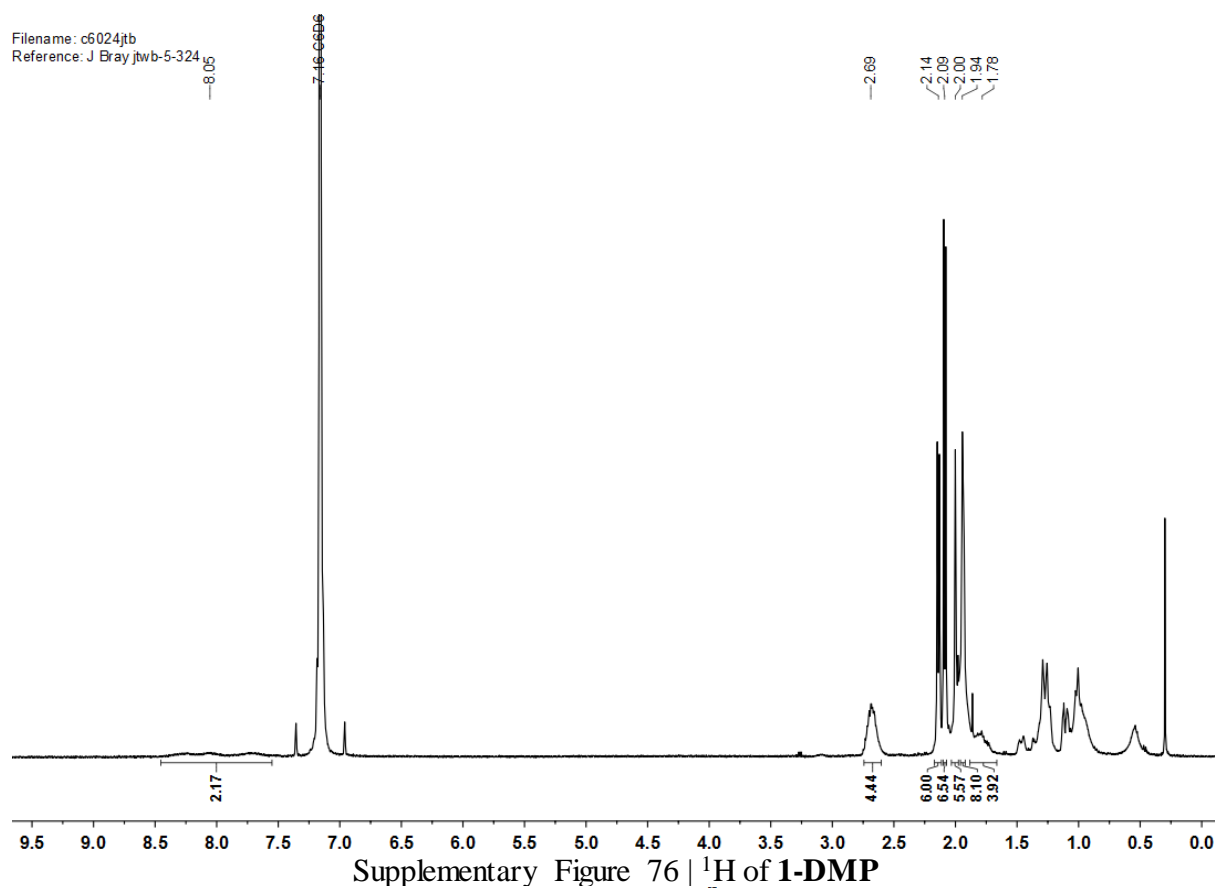
Filename: k7963jtb
Reference: J Bray jtwb-4-193



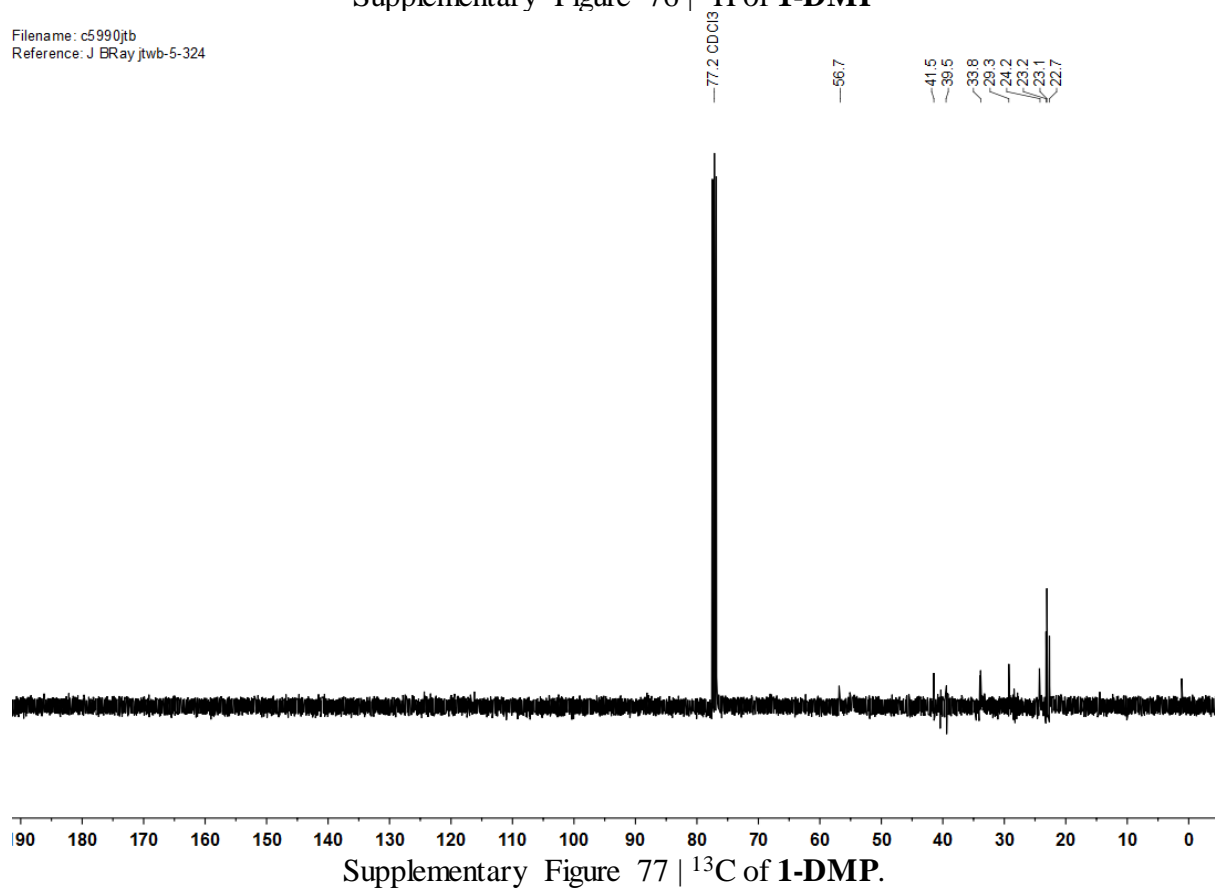
Supplementary Figure 75 | ¹³C NMR of **1-Aze**.

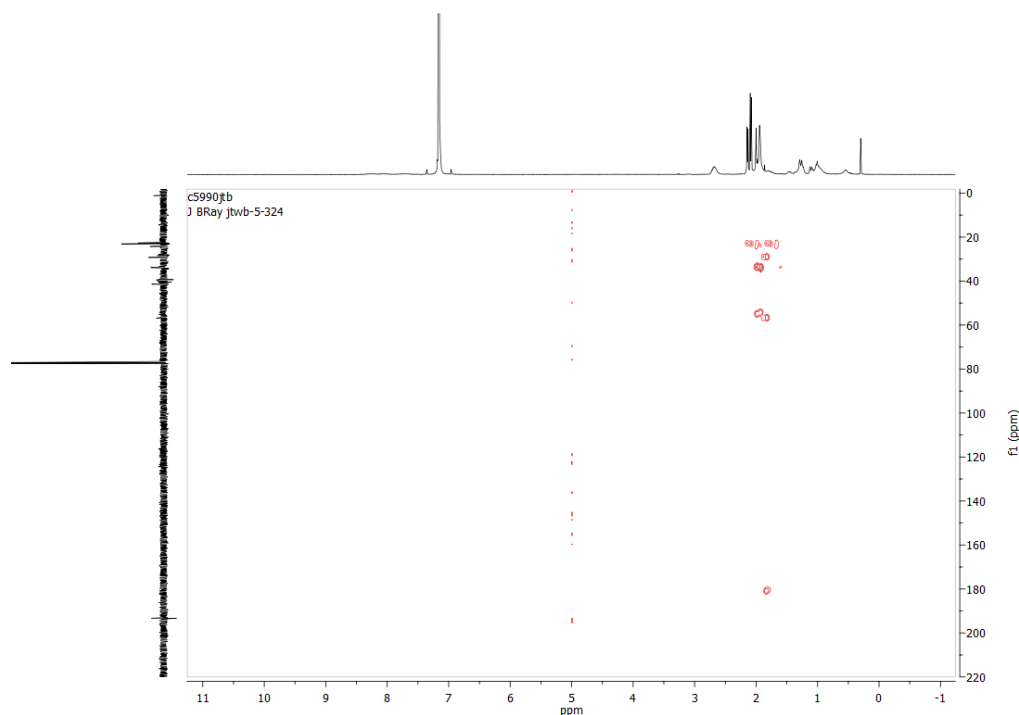
5.4. 1-DMP

Filename: c6024jtb
Reference: J Bray jtwb-5-324



Filename: c5990jtb
Reference: J BRay jtwb-5-324





Supplementary Figure 78 | ^1H - ^{13}C HMBC spectrum of **1-DMP**.

6. X-Ray crystallography

6.1. General details

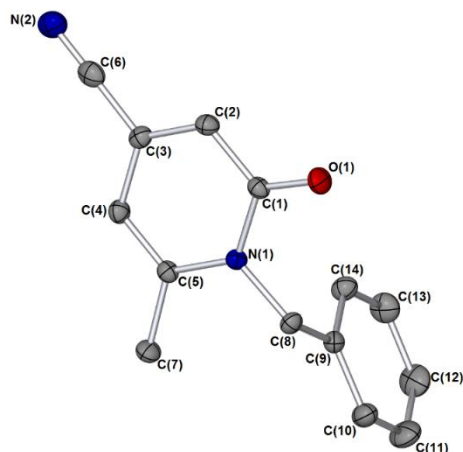
Diffraction data were collected at 110 K on an Agilent SuperNova diffractometer with Mo $K\alpha$ radiation ($\lambda = 0.71073 \text{ \AA}$). Data collection, unit cell determination and frame integration were carried out with CrysAlisPro. Absorption corrections were applied using face indexing and the ABSPACK absorption correction software within CrysAlisPro. Structures were solved and refined using Olex2²¹ implementing SHELX algorithms and the Superflip²²⁻²⁴ structure solution program. Structures were solved by charge flipping, Patterson or direct methods and refined with the ShelXL²⁵ package using full-matrix least squares minimisation. All non-hydrogen atoms were refined anisotropically. Hydrogen atoms were placed using a “riding model” and included in the refinement at calculated positions.

6.2. X-ray data for **3** and complexes **1-pyr**, **1-aze** and **1-dmp**

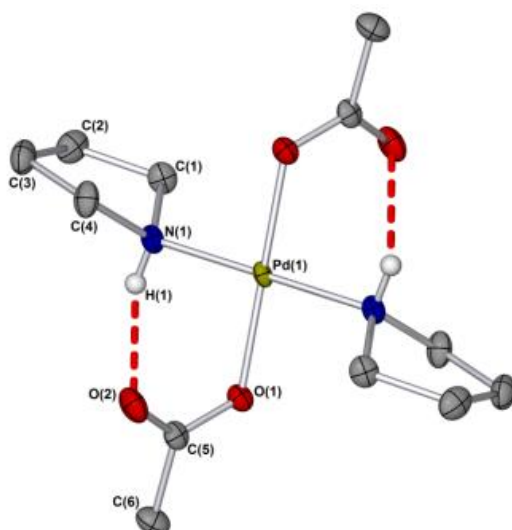
Table 3: X-ray data for **3** and complexes **1-pyr**, **1-aze** and **1-dmp**

Identification code	ijsf1330 (3)	ijsf1402 (1-aze)
CCDC number	CCDC 1863214	CCDC 1863216
Empirical formula	C _{13.97} H ₁₂ Br _{0.03} N _{1.97} O	C ₁₆ H ₃₂ N ₂ O ₄ Pd
Formula weight	225.87	422.83
Temperature/K	110.05(10)	110.10(14)
Crystal system	monoclinic	triclinic
Space group	P2 ₁ /c	P-1
a/Å	11.0909(2)	6.0767(4)
b/Å	13.3680(4)	7.1046(4)
c/Å	7.95097(18)	10.4577(5)
α/°	90.00	89.399(4)
β/°	92.498(2)	84.578(5)
γ/°	90.00	86.939(5)
Volume/Å ³	1177.72(5)	448.82(4)
Z	4	1
ρ _{calc} /mg/mm ³	1.274	1.564
m/mm ⁻¹	0.183	1.055
F(000)	475.0	220.0
Crystal size/mm ³	0.1799 × 0.1320 × 0.0503	0.2829 × 0.1162 × 0.0986
Radiation	Mo Kα (λ = 0.7107)	MoKα (λ = 0.7107)
2θ range for data collection	5.96 to 64.1°	5.736 to 64.162°
Index ranges	-16 ≤ h ≤ 15, -16 ≤ k ≤ 19, -11 ≤ l ≤ 10	-9 ≤ h ≤ 8, -10 ≤ k ≤ 10, - 15 ≤ l ≤ 15
Reflections collected	8699	8212
Independent reflections	3781 [R(int) = 0.0465]	2927 [R _{int} = 0.0323, R _{sigma} = 0.0372]
Data/restraints/parameters	3781/6/164	2927/0/111
Goodness-of-fit on F ²	1.083	1.081
Final R indexes [I ≥ 2σ (I)]	R ₁ = 0.0548, wR ₂ = 0.1181	R ₁ = 0.0251, wR ₂ = 0.0640
Final R indexes [all data]	R ₁ = 0.0771, wR ₂ = 0.1318	R ₁ = 0.0255, wR ₂ = 0.0645
Largest diff. peak/hole / e Å ⁻³	0.30/-0.28	1.61/-0.84

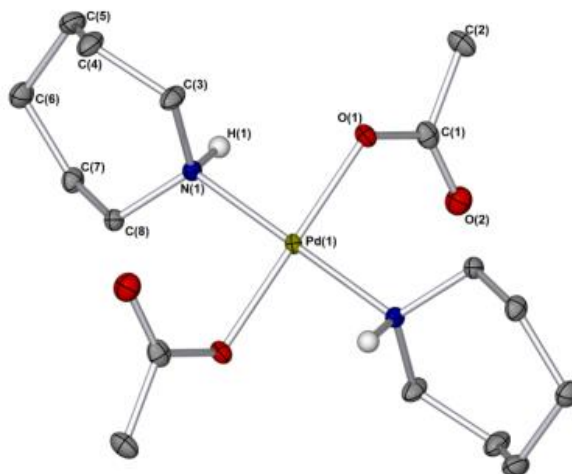
Identification code	ijsf1470 (1-dmp)	ijsf1464 (1-pyr)
CCDC number	CCDC 1863217	CCDC 1863215
Empirical formula	C ₁₈ H ₃₆ N ₂ O ₄ Pd	C ₁₂ H ₂₈ N ₂ O ₈ Pd ₁
Formula weight	450.89	402.76
Temperature/K	110.05(10)	110.05(10)
Crystal system	monoclinic	monoclinic
Space group	P2 ₁ /C	C ₁₂ /C1
a/Å	7.49848(14)	17.1405(6)
b/Å	9.61025(19)	6.10222(17)
c/Å	14.3500(3)	16.0694(5)
α/°	90.00	90.00
β/°	92.4862(18)	90.140(3)
γ/°	90.00	90.00
Volume/Å ³	1033.12(3)	1680.78(9)
Z	2	4
ρ _{calc} /mg/mm ³	1.449	1.449
m/mm ⁻¹	0.921	1.592
F(000)	472.0	832.0
Crystal size/mm ³	0.3156 × 0.2728 × 0.1575	0.1343 × 0.0963 × 0.0364
Radiation	MoKα (λ = 0.71073)	CuKα (λ = 1.54184)
2θ range for data collection	3.90 to 32.06	5.15 to 69.30
Index ranges	-11 ≤ h ≤ 11, -10 ≤ k ≤ 14, -20 ≤ l ≤ 9	-20 ≤ h ≤ 20, -7 ≤ k ≤ 7, -19 ≤ l ≤ 14
Reflections collected	6182	4628
Independent reflections	3286 [R _{int} = 0.0237, R _{sigma} = 0.0414]	1496 [R _{int} = 0.0295, R _{sigma} = 0.0286]
Data/restraints/parameters	3286/0/122	1496/0/110
Goodness-of-fit on F ²	1.224	1.086
Final R indexes [I >= 2σ (I)]	R ₁ = 0.0342, wR ₂ = 0.0672	R ₁ = 0.0290, wR ₂ = 0.0728
Final R indexes [all data]	R ₁ = 0.0460, wR ₂ = 0.0722	R ₁ = 0.0335, wR ₂ = 0.0759
Largest diff. peak/hole / e Å ⁻³	1.055/-0.574	1.645/-0.760



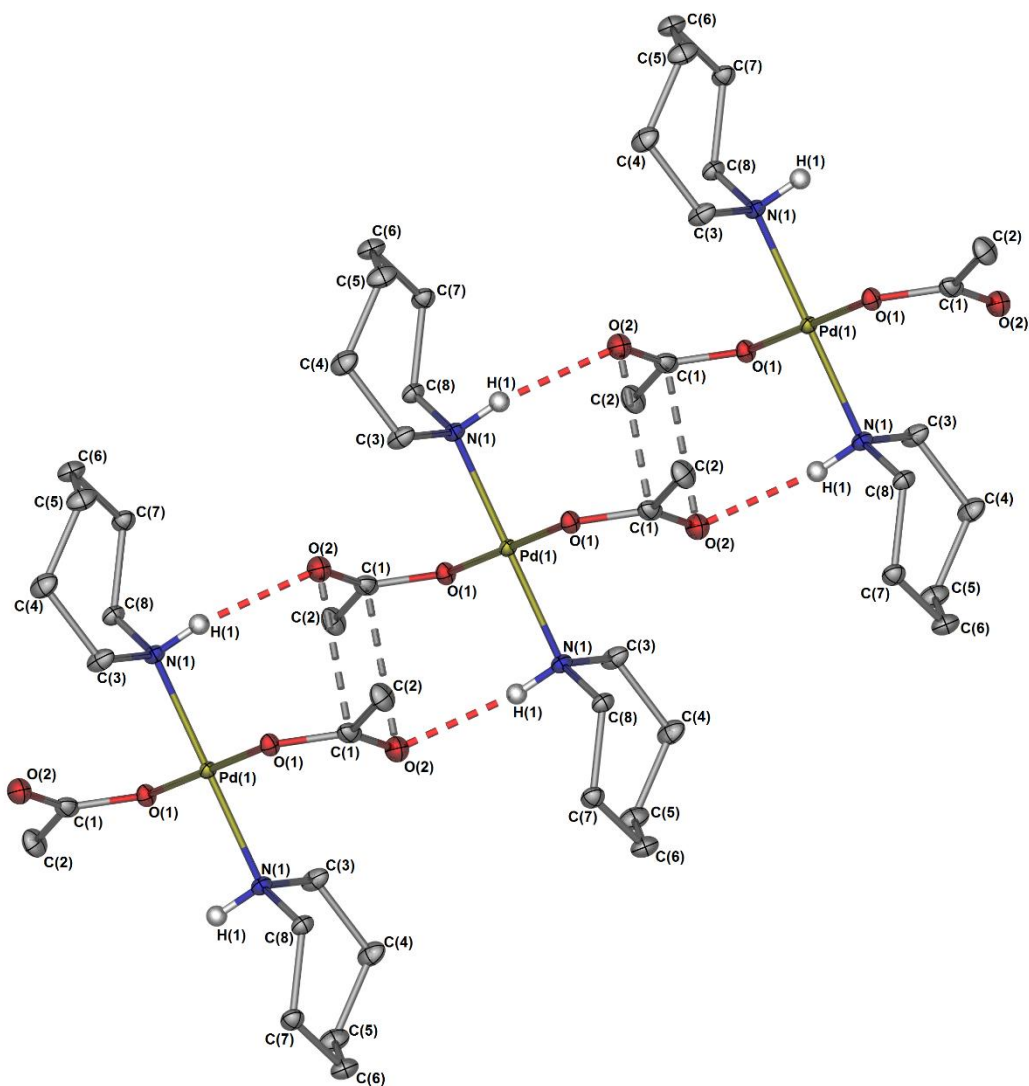
Supplementary Figure 79 | Structure of *N*-benzyl-4-cyano-6-methylpyrid-2-one (**3**) determined by X-ray diffraction; arbitrary numbering used. Hydrogen atoms removed for clarity. Thermal ellipsoids shown with a probability of 50%; numbers in parentheses are standard deviations from the measured value, denoting the error in the measurements. Selected bond lengths (Å): C(3)-C(6):1.431(3), C(6)-N(2): 1.150(3), C(1)-O(1): 1.2379(16), C(1)-N(1):1.4052(16), C(5)-N(1): 1.3811(16), C(8)-N(1):1.4717(17).



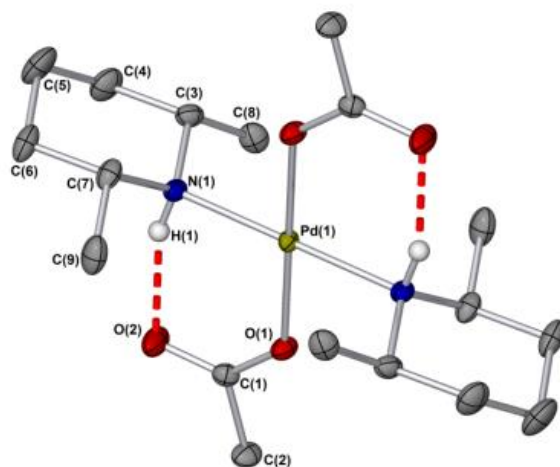
Supplementary Figure 80 | Structure of **1-Pyr**, determined by X-ray diffraction; arbitrary numbering used. Selected hydrogen atoms removed for clarity. Thermal ellipsoids shown with a probability of 50%. Selected bond lengths (Å): : N(1)-Pd(1): 2.043(3), O(1)-Pd(1): 2.015(2), C(1)-N(1): 1.484(4), C(5)-O(1): 1.282(4), C(5)-O(2): 1.243(4).



Supplementary Figure 81 | Structure of **1-Aze**, determined by X-ray diffraction; arbitrary numbering used. Selected hydrogen atoms removed for clarity. Thermal ellipsoids shown with a probability of 50%. Selected bond lengths (Å): N(1)-Pd(1): 2.0638(14), O(1)-Pd(1): 2.0050(12), C(1)-O(1): 1.286(2), C(1)-O(2): 1.236(2).



Supplementary Figure 82 | Extended lattice structure of 1-Aze, determined by X-ray diffraction; arbitrary numbering used. Selected hydrogen atoms removed for clarity. Thermal ellipsoids shown with a probability of 50%. Selected Hydrogen bond lengths and angles and Short-contact bond lengths calculated using Mercury: N(1)-H(1)···O(2): 2.972 Å, 158.93°, C(1)···O(2): 3.000 Å, C(1)-O(2)···C(1) 93.63°.



Supplementary Figure 83 | Structure of **1-DMP**, determined by X-ray diffraction; arbitrary numbering used. Selected hydrogen atoms removed for clarity. Thermal ellipsoids shown with a probability of 50%. Selected bond lengths (Å): N(1)-Pd(1): 2.0696(18), O(1)-Pd(1): 2.0191(16), C(1)-O(1): 1.266(3), C(1)-O(2): 1.229(3), C(3)-N(1): 1.481(3)

7. References

- 1 Still, W. C., Kahn, M. & Mitra, A. Rapid chromatographic technique for preparative separations with moderate resolution. *J. Org. Chem.* **43**, 2923-2925 (1978).
- 2 Watzky, M. A. & Finke, R. G. Transition Metal Nanocluster Formation Kinetic and Mechanistic Studies. A New Mechanism When Hydrogen Is the Reductant: Slow, Continuous Nucleation and Fast Autocatalytic Surface Growth. *J. Am. Chem. Soc.* **119**, 10382-10400 (1997).
- 3 Kemmer, G. & Keller, S. Nonlinear least-squares data fitting in Excel spreadsheets. *Nat. Protocols* **5**, 267-281 (2010).
- 4 Senecal, T. D., Shu, W. & Buchwald, S. L. A General, Practical Palladium-Catalyzed Cyanation of (Hetero)Aryl Chlorides and Bromides. *Angew. Chem. Int. Ed.* **52**, 10035-10039 (2013).
- 5 Frisch, M. J. T., G. W.; Schlegel, H. B.; Scuseria, G. E.; Robb, M. A.; Cheeseman, J. R.; Scalmani, G.; Barone, V.; Petersson, G. A.; Nakatsuji, H.; Li, X.; Caricato, M.; Marenich, A. V.; Bloino, J.; Janesko, B. G.; Gomperts, R.; Mennucci, B.; Hratchian, H. P.; Ortiz, J. V.; Izmaylov, A. F.; Sonnenberg, J. L.; Williams-Young, D.; Ding, F.; Lipparini, F.; Egidi, F.; Goings, J.; Peng, B.; Petrone, A.; Henderson, T.; Ranasinghe, D.; Zakrzewski, V. G.; Gao, J.; Rega, N.; Zheng, G.; Liang, W.; Hada, M.; Ehara, M.; Toyota, K.; Fukuda, R.; Hasegawa, J.; Ishida, M.; Nakajima, T.; Honda, Y.; Kitao, O.; Nakai, H.; Vreven, T.; Throssell, K.; Montgomery, J. A., Jr.; Peralta, J. E.; Ogliaro, F.; Bearpark, M. J.; Heyd, J. J.; Brothers, E. N.; Kudin, K. N.; Staroverov, V. N.; Keith, T. A.; Kobayashi, R.; Normand, J.; Raghavachari, K.; Rendell, A. P.; Burant, J. C.; Iyengar, S. S.; Tomasi, J.; Cossi, M.; Millam, J. M.; Klene, M.; Adamo, C.; Cammi, R.; Ochterski, J. W.; Martin, R. L.; Morokuma, K.; Farkas, O.; Foresman, J. B.; Fox, D. J. . *Gaussian 16, Revision A.03, Gaussian, Inc., Wallingford CT, 2016.*
6 See http://www.gaussian.com/g_tech/g_ur/u_cubegen.htm.
- 7 Karadakov, P. B. & Horner, K. E. Magnetic Shielding in and around Benzene and Cyclobutadiene: A Source of Information about Aromaticity, Antiaromaticity, and Chemical Bonding. *J. Phys. Chem. A* **117**, 518-523 (2013).
- 8 Horner, K. E. & Karadakov, P. B. Chemical Bonding and Aromaticity in Furan, Pyrrole, and Thiophene: A Magnetic Shielding Study. *J. Org. Chem.* **78**, 8037-8043 (2013).
- 9 Horner, K. E. & Karadakov, P. B. Shielding in and around Oxazole, Imidazole, and Thiazole: How Does the Second Heteroatom Affect Aromaticity and Bonding? *J. Org. Chem.* **80**, 7150-7157 (2015).
- 10 Schleyer, P. v. R., Maerker, C., Dransfeld, A., Jiao, H. & Hommes, N. J. R. v. E. Nucleus-Independent Chemical Shifts: A Simple and Efficient Aromaticity Probe. *J. Am. Chem. Soc.* **118**, 6317-6318 (1996).
- 11 Schleyer, P. v. R., Jiao, H., Hommes, N. J. R. v. E., Malkin, V. G. & Malkina, O. L. An Evaluation of the Aromaticity of Inorganic Rings: Refined Evidence from Magnetic Properties. *J. Am. Chem. Soc.* **119**, 12669-12670 (1997).
- 12 Schleyer, P. v. R. *et al.* Dissected Nucleus-Independent Chemical Shift Analysis of π -Aromaticity and Antiaromaticity. *Org. Lett.* **3**, 2465-2468 (2001).
- 13 Katritzky, A. R., Karelson, M., Sild, S., Krygowski, T. M. & Jug, K. Aromaticity as a Quantitative Concept. 7. Aromaticity Reaffirmed as a Multidimensional Characteristic. *J. Org. Chem.* **63**, 5228-5231 (1998).
- 14 Storr, T. E. *et al.* Pd(0)/Cu(I)-Mediated Direct Arylation of 2'-Deoxyadenosines: Mechanistic Role of Cu(I) and Reactivity Comparisons with Related Purine Nucleosides. *J. Org. Chem.* **74**, 5810-5821 (2009).

- 15 McNally, A., Haffemayer, B., Collins, B. S. L. & Gaunt, M. J. Palladium-catalysed C-H activation of aliphatic amines to give strained nitrogen heterocycles. *Nature* **510**, 129-133 (2014).
- 16 Shu, Z., Ye, Y., Deng, Y., Zhang, Y. & Wang, J. Palladium(II)-Catalyzed Direct Conversion of Methyl Arenes into Aromatic Nitriles. *Angew. Chem. Int. Ed.* **52**, 10573-10576 (2013).
- 17 Laube, M. *et al.* Diaryl-Substituted (Dihydro)pyrrolo[3,2,1-hi]indoles, a Class of Potent COX-2 Inhibitors with Tricyclic Core Structure. *J. Org. Chem.* **80**, 5611-5624 (2015).
- 18 Gerber, R., Oberholzer, M. & Frech, C. M. Cyanation of Aryl Bromides with $K_4[Fe(CN)_6]$ Catalyzed by Dichloro[bis{1-(dicyclohexylphosphanyl)piperidine}]palladium, a Molecular Source of Nanoparticles, and the Reactions Involved in the Catalyst-Deactivation Processes. *Chem. Eur. J.* **18**, 2978-2986 (2012).
- 19 Reeves, J. T. *et al.* Transnitration from Dimethylmalononitrile to Aryl Grignard and Lithium Reagents: A Practical Method for Aryl Nitrile Synthesis. *J. Am. Chem. Soc.* **137**, 9481-9488 (2015).
- 20 Kim, J., Choi, J., Shin, K. & Chang, S. Copper-Mediated Sequential Cyanation of Aryl C-B and Arene C-H Bonds Using Ammonium Iodide and DMF. *J. Am. Chem. Soc.* **134**, 2528-2531 (2012).
- 21 Dolomanov, O. V., Bourhis, L. J., Gildea, R. J., Howard, J. A. K. & Puschmann, H. OLEX2: a complete structure solution, refinement and analysis program. *J. Appl. Crystallogr.* **42**, 339-341 (2009).
- 22 Palatinus, L., Prathapa, S. J. & van Smaalen, S. EDMA: a computer program for topological analysis of discrete electron densities. *J. Appl. Crystallogr.* **45**, 575-580 (2012).
- 23 Palatinus, L. & Chapuis, G. SUPERFLIP - a computer program for the solution of crystal structures by charge flipping in arbitrary dimensions. *J. Appl. Crystallogr.* **40**, 786-790 (2007).
- 24 Palatinus, L. & van der Lee, A. Symmetry determination following structure solution in P1. *J. Appl. Crystallogr.* **41**, 975-984 (2008).
- 25 Sheldrick, G. A short history of SHELX. *Acta Crystallogr. Sect. A: Found. Crystallogr.* **64**, 112-122 (2008).